PULSED LASER INDUCED DOPING OF TWO-DIMENSIONAL CRYSTALS

Ioanna E. Demeridou

Supervisors: Dr. Emmanuel Stratakis
Prof. Ioannis Kominis
Prof. George Kioseoglou

Department of Physics
University of Crete

This dissertation is submitted for the degree of Doctor of Philosophy

March 2021

Contents

Acknowledgments

First, I would like to express my gratitude to my supervisors, Prof. George Kioseoglou and Dr. Emmanuel Stratakis for their incredible support, advice and guidance throughout my entire Ph.D. program. Their generous encourage and discussions combined with their vast experience made this Ph.D. work constructive and productive.

I want to express my appreciation and thanks to my supervisor Prof. Ioannis Kominis for doing me the honor of evaluating my Ph.D. thesis and offer me the opportunity to present this work.

I gratefully thank Prof. Alexandros Georgakilas, Prof. Peter Rakitzis, Prof. Nikos T. Pelekanos, and Prof. Emmanuel Kymakis for accepting to be my dissertation committee members. Their time spent on the evaluation of this dissertation is sincerely appreciated.

I would like to thank our collaborators Prof. Panos Patsalas and Nikolaos Pliatsikas from AUTH, Prof. Nikos T. Pelekanos and Dr. Savvas Germanis from Micro/Nano electronics group from UOC and finally Dr. Yuanyue Liu and Prof. W. A. Goddard III from Caltech. I thank my colleagues from the 2D Materials subgroup, Dr. Ioannis Paradisanos, Mr. Antonis Papadopoulos, Dr. Leonidas Mouchliadis, Mr. George Kourmoulakis, Ms. Eirini Katsipoulaki and all the members of the Ultrafast Laser Micro and Nano Processing lab of IESL-FORTH for the perfect collaboration.

Also, I would like to thank Ms. Maria Fouskaki and Mr. Yannis Labrakis for the great willingness to help with all the technical issues that I had.

Special thanks to Kyriaki Savva, Eleftheria Babaliari, Evi Kavatzikidou, Andreas Lemonis, Antonis Papadopoulos, and Konstantinos Triantopoulos. These people deserve my gratitude and regard for the support, interesting discussions, and the unforgettable fun times that we have shared.

I am deeply and forever indebted to my family and childhood friends for their love, support and encouragement throughout my entire life and studies.

I am grateful to the European Horizon 2020 - FET OPEN Program “MouldTex”, the Nanoscience Foundries and Fine Analysis (NFFA) and EU-ESF Fund through HRDELL 2014-2020 program from Greece for the generous financial support.

Abstract

Two-dimensional transition metal dichalcogenides (2D-TMDs) attract worldwide interest in the last few decades since the successful isolation and characterization of graphene. TMDs are semiconductors and provide unique optoelectronic properties attributed to their ultrathin nature. As their numbers of layers decreases, turned from an indirect to direct bandgap semiconductor with possible applications in visible range optoelectronic devices. Here, we investigate the optical properties of monolayer WS_2, a member of the TMD family, and the effects of the UV pulsed laser-induced doping.

We proposed a novel doping method that modulates the electron density in a 1L-WS_2. Chlorine-doped tungsten disulfide monolayer (1L-WS_2) with tunable charge carrier concentration has been realized by pulsed laser irradiation of the atomically thin lattice in a chlorine environment. A systematic shift of the neutral exciton peak, in the photoluminescence spectra, towards lower energies indicates the reduction of the crystal's electron density. The capability to progressively tune the carrier density upon variation of the exposure time is demonstrated. The Fermi level shift is correlated to the respective electron density modulation due to the chlorine species. At the same time, is found that the effect can be reversed upon continuous-wave laser scanning of the monolayer in the air. Such bidirectional control of the Fermi level, coupled with the capability offered by lasers to process at pre-selected locations, can be advantageously used for spatially resolved doping modulation in 1L-WS_2 with micrometric resolution.

This process has boosted interests in controlling valley polarized light emission of doped monolayer WS_2. TMDs have interesting spin/valley properties due to the large spin-orbit coupling and the non-equivalent valleys in their band structure. We demonstrate spin-valley polarization tunability by more than 40% in 1L-WS_2 via photochlorination. Polarization photoluminescence spectroscopy was performed in the temperature range from 4K to 300K.

The reduction of circular polarization, after the photochlorination treatment, was attributed to the reduction of defect sites in the crystal lattice and consequently to the increase of the non-radiative exciton lifetime. Ultrafast time-resolved transient absorption spectroscopy measurements and theoretical simulations support our findings.

Furthermore, taking advantage of room-temperature valley polarization on graphene, we performed measurements of monolayer WS_2 with various substrates. By illuminating WS_2/Graphite with on-resonance circularly polarized light at room temperature, we measure significantly large circular polarization (P_C up to 25%). Using the photochlorination process, we can modulate the polarization of the neutral exciton emission continuously from 27% to 38% for 1L-WS_2/Graphite. We show that valley polarization strongly depends on the relationship between the doping and the supporting layer of TMDs. These preliminary results shed light on the significant role of the substrate on valley polarization in monolayer TMDs.

These findings make TMDs promising materials for future applications and computing architectures.

List of Figures

Thesis Outline

This thesis is organized and structured into five different parts.

Chapter I is an introduction to layered transition metal dichalcogenides (TMDs). Single layers (1L) of TMDs arise as an exciting class of atomically thin, two-dimensional (2D) materials with worldwide interest in the research community. Fundamental and essential characteristics of these materials are described, including their structural, electronic, optical, and vibrational properties. These are followed by a discussion on the inversion symmetry breaking in a monolayer and the optical selection rules in 2D crystals. All these unique properties lead to great application potential of 2D-TMDs. The main characteristics of graphene and graphite are also presented in this chapter.

Chapter II cover the basic doping methods in TMDs and the impacts of tuning the carrier density in TMDs. These doping strategies are reflected by Raman and Photoluminescence spectroscopy as well as valley polarization measurements. It is a general background and a literature review that provides an overview of different doping approaches in TMDs. Here, for the first time, we take advantage of the powerful UV lasers for TMDs doping. This approach will be presented in detail in the following chapters. One of the main objectives of this thesis is to develop a method to control the carrier density and, as a consequence, the optoelectronic properties of monolayer TMDs.

Chapter III describes the experimental techniques used during this thesis. Micro-Photoluminescence spectroscopy, micro-differential reflectivity, and spin valley polarization measurements are essential in characterizing and evaluating the overall quality of our 2D materials. With these techniques, we can detect the possible changes after photochlorination treatment. All experimental details are included in this section. Finally, this chapter presented the photochlorination doping technique, a unique approach to induce carriers in the crystal structure of a 1L-TMD.

Chapter IV presents the main results of this thesis. It comprises three distinct parts.

- Chapter 4.1 shows that controllable irradiation of WS_2 monolayers with UV nanosecond pulses in a rich chlorine environment can affect the crystal's carrier density resulting in Fermi level shift. As a result, this technique offers the possibility of selective tuning of the crystal's electronic properties. We observe significant shifts of the exciton complexes that suggest a reduction of the electron density. Moreover, the overall PL intensity is enhanced by molecules that deplete electrons from the crystal. Our work demonstrates the ability of photochemical doping to effectively tune the emission energy of the exciton species. Micro-Photoluminescence measurements at 78K showed a significant shift of neutral exciton energy to smaller values and, at the same time, a switching effect on the relative intensity of neutral and charged exciton. This electron-withdrawing process enabled the determination of the trion binding energy of the intrinsic crystal, found to be as low as 20meV, following theoretical predictions. These results are further supported by Raman spectroscopy. By monitoring the two main Raman vibrational modes is revealed that chlorine depletes the excess electrons of monolayer WS_2. Our observed Raman features indicate the chlorine doped WS_2 sample is less n-doped than that of as-prepared WS_2 due to the charge transfer during chlorine adsorption. Specifically, is found that the A_1' mode blue-shifts by $3cm^{-1}$ after radiation with 40 pulses in the chlorine environment. Additionally, the effect reversed upon continuous-wave laser scanning of the monolayer in the air. Density functional theory calculations reveal that chlorine physisorption is responsible for the carrier density modulation induced by the pulsed laser photochemical reaction process. This method can be extended for the controllable doping of other TMD monolayers.
- Chapter 4.2 presents the effect of the photochlorination on valley polarization properties. The reduced dimensional hexagonal lattice of TMDs combined with their unique optical selection rules open up fascinating opportunities for carrier manipulation in different

valleys. Recent publications have indicated the detection and control of valley polarization in 1L-TMDs with temperature, excitation energy, electron-hole exchange and electron-phonon coupling. The emerging field of valleytronics has raised great interest in investigating valley polarized light emission of doped monolayer TMDs. This is the first study of chemically-controlled valley polarization in 1L-WS_2/hBN for optoelectronic/valleytronic devices. Doping- and temperature- dependent valley polarization phenomena and the related non-radiative exciton lifetimes are examined in off-resonant conditions for 1L-WS_2 on hBN and SiO_2 substrates. High tunability of the valley polarization in the 1L-WS_2/hBN system has been demonstrated. A reduction of more than 40% in the circular polarization of the neutral exciton at 4K was achieved. The decrease of the polarization was attributed to the reduction of the active defect sites as a result of the chlorine doping. That affects the non-radiative recombination time τ_{NR} and the degree of the emitted circular polarization. Our results are supported by transient absorption spectroscopy measurements. These findings could be useful for understanding fundamental spin relaxation phenomena in 2D materials.

- Chapter 4.3 investigates the room-temperature valley polarization measurements of monolayer WS_2 on different substrates. It is found that while the neutral exciton emission of 1L-WS_2 on top of graphene/graphite has zero polarization at room temperature and off-resonance conditions, we observe a room temperature optical polarization over 25% with on-resonance conditions. Using the photochlorination process, we can modulate the polarization of the neutral exciton emission continuously from 27% to 38% for 1L-WS_2/Graphite. We show that valley polarization strongly depends on the relationship between the doping and the supporting layer of TMDs. These results suggest a pathway towards engineering valley polarization and exciton lifetimes in TMDCs by controlling the type of substrate and the carrier's density that serve as non-radiative exciton recombination sites.

Chapter V summarizes the results and contributions of this thesis. A concluding overview of this work is presented.

Chapter I

Structure and excitons in 2D Materials

1.1 Crystal structure and electronic properties of TMD monolayers

In 2004, with the successful isolation of graphene by Geim and Novoselov,[1] research into the field of two-dimensional (2D) materials exploded. The isolation of graphene and its impressive properties led to a great interest in the isolation of monolayers of other materials with various interesting electrical, optical, and physical properties. These thin layers have a diverse range of properties – for example, hexagonal boron nitride (hBN) as an insulator, molybdenum disulfide (MoS_2), and tungsten disulfide (WS_2) as semiconductors, and tantalum disulfide (TaS_2), niobium diselenide ($NbSe_2$) as superconductors.[2] The divergent categories of 2D materials make them suitable for use in a wide range of future applications. These materials can be considered layered materials where individual layers are strongly bonded in-plane and weakly bonded out-of-plane in between layers. These weak, interlayer, van der Waals interactions allow the formation of a monolayer from bulk crystals. These bonds also allow these layers to slide on top of one another similarly to other layered materials like graphite.[3,4] Research into 2D materials captivates worldwide interest due to the various properties that make them suitable for industrial technology. Those materials provide great potential for interesting optoelectronic applications such as field-effect transistors,[5,6] light-emitting diodes (LED), sensors, photodetectors, photovoltaic devices, and integrated circuits.[7–10] Recent advances in 2D crystals have opened up new opportunities for novel valleytronic devices.[11,12]

Transition Metal Dichalcogenides (TMDs) are generally inorganic materials with a chemical formula of MX_2 where M is a transition metal (W, Mo) and X is a chalcogen (S, Se, Te). TMDs consist of layers stacked on top of one another. Most of the physical properties of TMDs are anisotropic due to their layered structure, i.e., the in-plane and out-of-plane properties are significantly different. The basic building block for these materials composed of three hexagonally packed atomic layers where a layer of metal atoms is sandwiched between two layers of chalcogen atoms.[13] Due to the strong chalcogen metal covalent bonds within a single

layer and weak van der Waals forces between layers, it is relatively easy to exfoliate them and obtain a monolayer. Different possible stacking arrangements of the monolayers give rise to distinct polytypes. Each polytype has a prefix, e.g., 1T, 2H, 3R, where the number refers to the number of monolayers within a unit cell and the letter to the symmetry of the unit cell: trigonal, hexagonal, and rhombohedral, respectively. In the 2H polytype (also called trigonal prismatic configuration), the upper layer rotated by 180 degrees concerning the lower layer. Thus, the metal atoms are placed above the chalcogen atoms and vice versa. Every metal atom is always surrounded by six chalcogen atoms, which allows the metal coordination to be either trigonal prismatic or octahedral. Fig. 1.1 (a) and (b) show the schematic representation of the trigonal prismatic coordination. In this thesis, we investigate the monolayer tungsten disulfide in the 2H form (2H-WS_2).

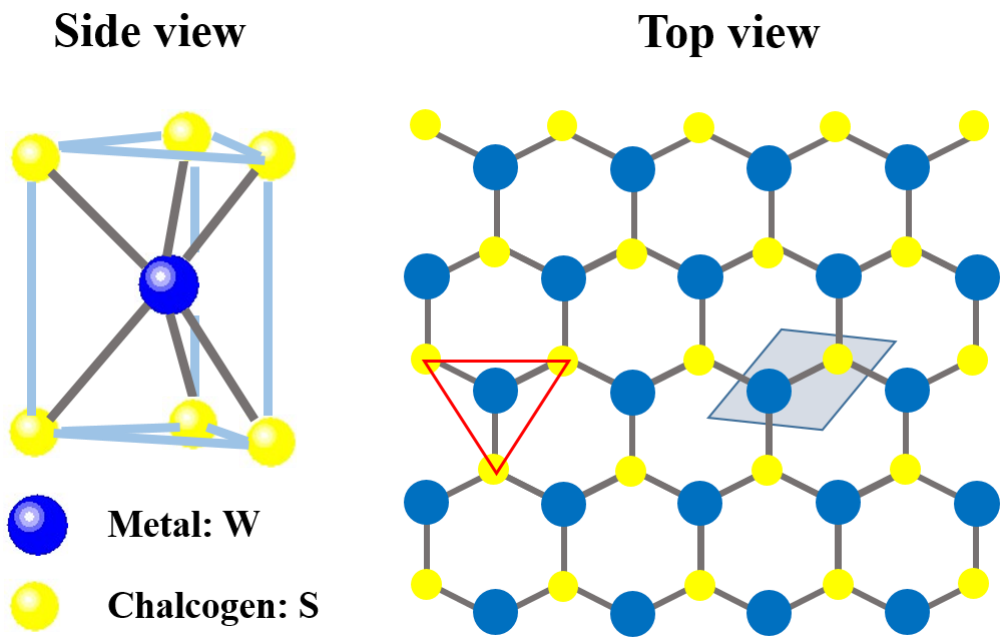

Figure 1.1 Side and top view of the crystal structure of TMD monolayers. The blue and yellow spheres represent M and X atoms, respectively. The light blue diamond region is the 2D unit cell. Side view: Trigonal prismatic coordination geometry, corresponding to the red triangle in top view. Reproduced from Ref. [14]

The Brillouin zone has the form presented in Fig. 1.2. The hexagonal lattice in real space results in a hexagonal lattice in momentum space, similar to graphene. It consists of inequivalent K and K- (sometimes referred to as K') points in the corners of the momentum space lattice. These

points are involved in the direct transitions in bulk and monolayer crystals. The symmetry points are critical for the electronic structure of MX_2 compounds: the center of the Brillouin zone, the Γ point, where the electronic states are involved in the indirect transitions in bulk crystals. The high symmetry points at the Brillouin zone boundary for two-dimensional monolayers are labeled as Q and K.

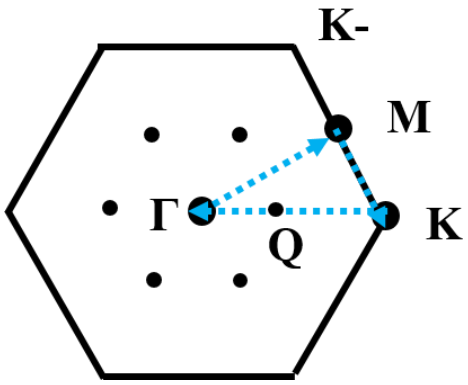

Figure 1.2 Brillouin zone of the hexagonal lattice in TMDs, with the K and K- points labelled. [15]

One of the most impressive characteristics of TMDs is the shift of the band structure exhibit with the changing number of layers. The calculated electronic band structures of bulk and monolayer WS_2 crystal are presented in Fig. 1.3 [16]. The calculations reveal an indirect bandgap in the bulk crystal located between the valence band maximum (VBM), situated at the center of the Brillouin zone (Γ point), and a conduction band minimum (CBM) between the Γ and K point (noted as Q). The red arrow in Fig. 1.3 (a) illustrates the indirect optical transition between these points. The electronic states involved in the indirect transition (CBM at Q and VBM at Γ) originate from a linear combination of tungsten d_{xy} and $d_{x^2-y^2}$ orbitals and chalcogen p_z-orbitals. The wave functions have a spatial extension in z-direction, i.e., along the c-axis of the crystal. These electronic states exhibit a strong interlayer coupling, and their dispersion strongly depends on the number of layers. The indirect bandgap in bulk crystals leads to an extremely weak (negligible) quantum yield for the photoluminescence (PL).[17] While reducing the number of layers, the electronic band structure evolves to the one presented in Fig. 1.3 (b) for monolayer

WS_2 crystal. The conduction band, as well as the valence band, is dominated by the d-electron orbitals of the transition metal atoms. At the VBM and CBM, they hybridize with the p-electron orbitals of the chalcogenide atoms. The states at the Γ and Q point have a strong metal d-orbital character combined with p_z-orbitals of chalcogen and depend strongly on vertical interlayer coupling (absent in monolayer). Because the hybridization happens mostly at these points and the chalcogenide atoms are at the surface of the TMD layer, leads to strong interactions between the layers. For this reason, we can observe a significant change in the band structure at the Γ point, as the number of layers increases. On the other hand, the d-orbitals of the transition metals contributing to the conduction/valence band states at the K point remain mostly unaffected because they are positioned in the middle of the layer X-M-X.[18,19] The orbitals at the K point are independent of the number of layers.

Decreasing the number of layers, the energy at Γ point changes dramatically, while at the K point remains practically unchanged, for the reasons mentioned above. In the monolayer limit, both the VBM and CBM move from the Γ and Q, respectively, to the K point of the Brillouin zone. As a result, a monolayer 2H-MX_2 becomes a direct bandgap material with an optical transition at the corner of the Brillouin zone. Finally, in a WS_2 monolayer, the VBM at K point as well as the entire conduction band increases to form a new greater direct bandgap at K point. The WS_2 bandgap changes from 1.3eV indirect bandgap in bulk to 2.1eV direct bandgap in monolayer.[17,20]

This dramatic change of electronic structure in monolayer WS_2 can explain the observed jump in monolayer photoluminescence efficiency. This direct bandgap manifests itself in extraordinary room temperature PL, which is attributed to the effect of quantum confinement on the material's electronic structure[17] and allows fast identification of single layers.

In 2010, Mak et al.[17] and Splendiani et al.[18] showed that MoS_2, which has previously shown to exist in a few-layer state,[21] showed extraordinary photoluminescence (PL) in its single-layer

form. The same conclusion applies to the rest of the TMDs. They could be more practical than graphene with a zero bandgap. The presence of a significant direct bandgap in WS_2 indicates that it could be suitable for use as active materials for the semiconductor industry.

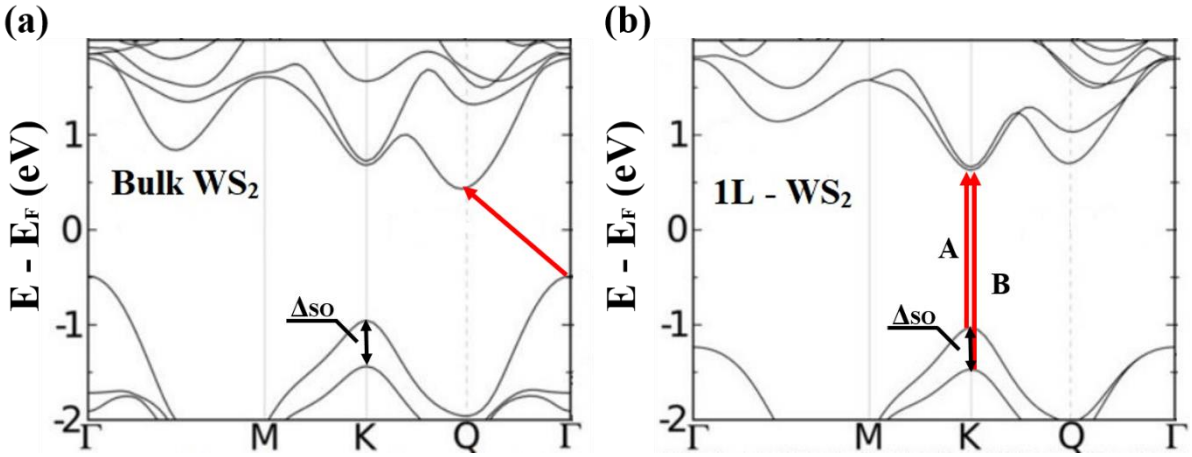

Figure 1.3 Calculated DFT electronic band structures of (a) bulk and (b) monolayer WS_2 crystal. The solid red arrows indicate the lowest energy transitions, (a) the indirect bandgap and (b) the direct bandgap and also the transition associated with the low-energy A and B excitons. Δ_{SO} denotes the energy of the split VBM due to spin-orbit coupling. [16]

Additionally, a clear band splitting of VBM at the K point of the Brillouin zone in monolayers MX_2 is observed due to the strong spin-orbit coupling as in bulk crystals. The spin-orbit splitting increases with the atomic number of a transition metal or chalcogen atom. The splitting in tungsten dichalcogenides compounds is larger (~400meV), compared to molybdenum dichalcogenides (~150meV). This happens due to the heavier mass of the tungsten atoms. Moreover, the spin-orbit coupling leads to a splitting of the CBM, the band edge at the K point, and at the secondary minimum Q, as illustrated in Fig. 1.3 (b).[16,20]

1.2 Fabrication of TMD monolayers

The synthesis of 2D TMDs performed using top-down or bottom-up approaches. The top-down strategy commonly includes exfoliation from the bulk layered crystals, while the bottom-up approach grows the crystals through vapor deposition. The TMDs samples prepared by mechanical and liquid exfoliation methods (top-down) have good quality, but their size is small.

The Chemical Vapor Deposition (CVD) approach (bottom-up) is suitable for wafer-scale fabrication and real device applications.

Mechanical exfoliation is the dominant technique used in this thesis to perform 2D crystals. The first realize of graphene was in 2004, using the "scotch-tape" method.[1] This method involves peeling off layers of carbon atoms from graphite using adhesive tape. Mechanical exfoliation is now generally applied to produce 2D crystals beyond graphene.[6,22,23] Monolayers of WS_2 and MoS_2 first isolated via mechanical exfoliation from bulk crystals using Scotch tape.[5,17,18] The produced monolayer regions have high structural and electronic quality but a small lateral size.

The mechanical exfoliation technique is a low-cost method for fabricating monolayers or a few-layers of many different 2D materials for initial studies. The monolayers were fabricated to test electronic and optical properties and even the stability in ambient conditions. This method produces high-quality crystals free from dopants introduced from chemical processes. Therefore, mechanical exfoliation is ideal for studies on the intrinsic physical properties of 2D materials and the fabrication of proof-of-concept devices. Many efforts have been made to scale up the produced monolayer by mechanical exfoliation and test these materials' suitability for applications in the electronics industry.[24] However, the disadvantages of this method are its improbable industrial scaling and limited crystal sizes.

Liquid-exfoliation [3,25–27] may lead to a higher yield, but it still faces limitations in its solution-based processes, smaller crystal sizes, and varying qualities. For these reasons, the bottom-up approach using chemical vapor deposition (CVD) may be the only scalable route in obtaining high-quality, large-area, and continuous 2D crystals necessary for wafer-scale device fabrications.[28,29]

1.3 Excitons in monolayer TMDs

The optical response of monolayer dichalcogenides dominated by excitonic effects. A photon is absorbed in a semiconductor if its energy is enough to excite an electron from the valence to the conduction band. Photoluminescence is just a reverse process in which an electron in the conduction band recombines with a hole in the valence band under the emission of a photon. Electron and hole attract each other through Coulomb force, which results in the formation of electron-hole pairs, called excitons (X). The excitons are electrically neutral quasiparticles of bound electron-hole pairs formed by their mutual Coulomb attraction. A stable exciton will be formed if the binding energy of two particles is large enough to protect it against environmental perturbations.

The 2D nature of monolayer TMDs does not allow for much Coulomb screening of charges, unlike in a bulk semiconductor.[30,31] As depicted at the top of Fig. 1.4(a), when optical excitation creates an electron-hole pair in a typical bulk semiconductor, the surrounding material provides Coulomb screening, so the binding energy between the negatively charged electron and the positively charged hole is low.[32] The electron-hole pair is known as an exciton, but since the binding energy is so small, the exciton absorption energy is very close to the bandgap, shown at the top of Figure 1.4(b). We can consider the electron and hole as separate entities. However, the reduced Coulomb screening in TMDs allows for high binding energies, shown at the bottom of Fig. 1.4(a), creating a large energy gap between the exciton absorption and the bandgap edge, shown at the bottom of Fig. 1.4(b). The TMD binding energies are calculated to be up to and even over 1eV,[31,33–36] although experiments have shown it to be a bit smaller.[32,37] This binding energy is so large that we must also consider the charged exciton.[32,34,36,38]

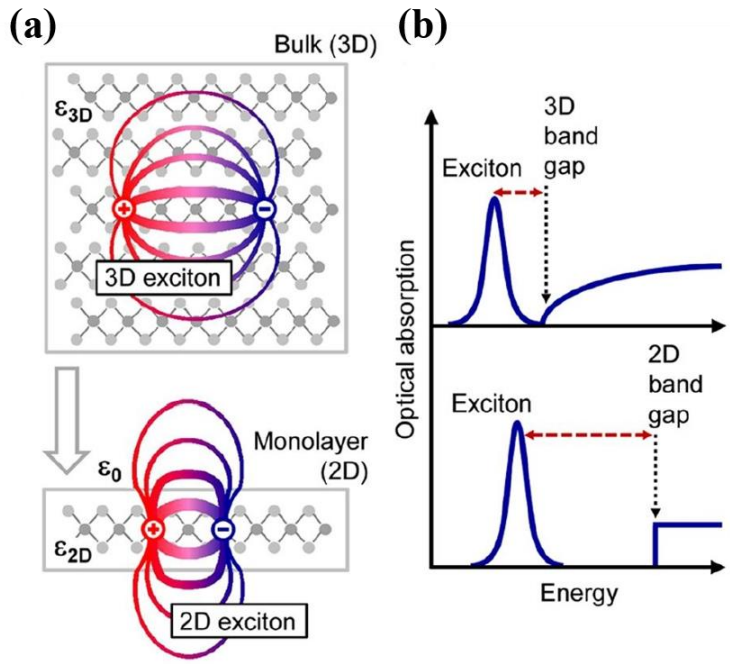

Figure 1.4 Coulomb Screening and Binding Energies in Bulk vs. 2D. (a) The differences in the real space environment, specifically the dielectric constants, are shown for the 3D and 2D exciton. (b) The effect of the changes in the environment is shown for both 3D and 2D. In 3D, the exciton absorption energy is very close to the bandgap. However, in 2D, the exciton absorption energy and 2D bandgap are separated by a substantial energy gap.[32]

The theory of excitons in crystals has developed from two different points of view. Depending on the exciton radius and the strength of the Coulomb interaction between electron and hole. Excitons in solids can be divided into two types. In materials with a small dielectric constant, the electron and hole are tightly bound to each other within the same or nearest neighbor unit cells. These excitons are called Frenkel excitons with typical binding energy on the order of 0.1-1eV. In semiconductors, the dielectric constant is generally large. Electric field screening by the valence electrons reduces the Coulomb interaction between electrons and holes, resulting in the exciton radius larger than the lattice spacing. Such excitons are called Wannier-Mott excitons. Because of the lower masses and the screened Coulomb interaction, the binding energy of Wannier-Mott excitons is typically in the order of 0.01eV.[39] As a consequence, in monolayers dichalcogenides, excitons have both Wannier-Mott and Frenkel character. The exciton wave function is larger than the lattice constant like in the Wannier-Mott type of excitons and strongly bound like Frenkel excitons. The binding energy is comparable to that for typical Frenkel excitons. The calculated 2D Bohr radius is about 1nm[33] so that the wave function for the electron-hole relative motion extends over several tens of unit cells.[40]

Moreover, the exciton series deviates significantly from the 2D hydrogen model. In the hydrogen model, the orbitals with the same principal quantum number degenerate.

The excitons in monolayer TMDs as Wannier-Mott type, whose wave function extends over multiple unit cells, are delocalized states that can freely move throughout the crystal so-called "free" excitons.[40,33] The motion of free exciton in semiconductors treated like a motion of a two-body problem, which separates into the center of mass motion and the relative motion.

The relative movement of electron and hole with Coulomb potential, $-\frac{e^2}{\varepsilon\,|r_e - r_h|}$, is mathematically equivalent to a hydrogen-like problem, where $r_e - r_h$ is the electron-hole distance and ε is the dielectric constant of the material. In the case of isotropic 2D, the electron-hole pair binding energy is enhanced due to spatial confinement and defined as:[41,32]

$$E_n^{2D} = -\frac{\mu e^4}{2\varepsilon^2\hbar^2}\frac{1}{\left(n - {}^1/_2\right)^2} = -R_X\frac{1}{\left(n - {}^1/_2\right)^2} \tag{1.1}$$

where integers n=1,2,3,.. is the principle quantum number; $R_X = \frac{\mu e^4}{2\varepsilon^2\hbar^2}$ is the exciton Rydberg energy and $\mu = \frac{m_e m_h}{m_e + m_h}$ is the reduced electron-hole mass. From the results, the total exciton energy relative to quasiparticle bandgap E_g, for the 2D case, is given as:

$$E_X(n, K_C) = E_g - R_X\frac{1}{\left(n - {}^1/_2\right)^2} + \frac{\hbar^2 K_C^2}{2M} \tag{1.2}$$

where $M = m_e + m_h$ is the center of mass of electron-hole pair moves like a free particle with kinetic energy, $\overrightarrow{K_C} = \overrightarrow{k_e} + \overrightarrow{k_h}$.

Because of momentum conservation law and negligible photon wave number in comparison to the first Brillouin zone, only excitons with $K_C=0$ predominantly participate in direct optical transitions. Thus the spectrum of the exciton is a series of discrete levels:

$$E_X(n) = E_g - R_X\frac{1}{\left(n - {}^1/_2\right)^2} \tag{1.3}$$

The excitonic effects are more clearly manifested in monolayer or a few-layer TMDs, arising from the significant enhancement of Coulomb interactions in the 2D limit due to spatial confinement and weak dielectric screening.[42,43] Due to lack of inversion symmetry in monolayer, the spin-orbit coupling induces a large splitting of valence bands ranging between 150meV (MoS_2) up to 460meV (WSe_2). The effect of spin-orbit splitting in the conduction band is negligible.[11] Therefore, there are two possible vertical transitions from spin-orbit split valence band minimum to a doubly degenerate conduction band, which rise to two distinct low energy features in absorption spectra, commonly referred to as A and B exciton peaks (Fig. 1.5(b)).[44] The energy separation between A and B excitons correlates with the spin-orbit splitting valence bands Δ_{SO}.[36] In the photoluminescence (PL) spectra, the emission of A exciton is much more pronounced than B exciton, originating from dominantly forming A excitons due to the fast intra-valence-band relaxation processes. The excitonic peak energies in PL spectra are slightly redshifted from the corresponding absorption energies due to the Stokes shift. The emitted photon has lower energy than the absorbed photon, this energy difference is the Stokes shift.

It is possible to form an exciton from the coupling between electron and hole in different valleys because of multi-valleys in the Brillouin zone of monolayer TMDs. The former exciton commonly recombines radiatively and is called a bright exciton. The latter exciton is forbidden from direct recombination to emit a photon by the law of momentum conservation and is called dark exciton (Fig. 1.5(a)).[45] Beyond the neutral excitons, the greatly enhanced Coulomb interaction in monolayer TMDs implies the possibility of the existence of other many-body bound quasiparticles composed of a large number of charge carriers. The bound electron-hole pair can capture an extra electron or hole to form a negatively (X^-) or positively (X^+) charged exciton, which is also referred to as trion (Fig. 1.5(c)).[46] This happens when the material is electron or hole-doped, or with a large density of photo-excited carriers. [38,47,48] The trion has

experimentally been found to be stable even at room temperature with large binding energy.[47,49,50]

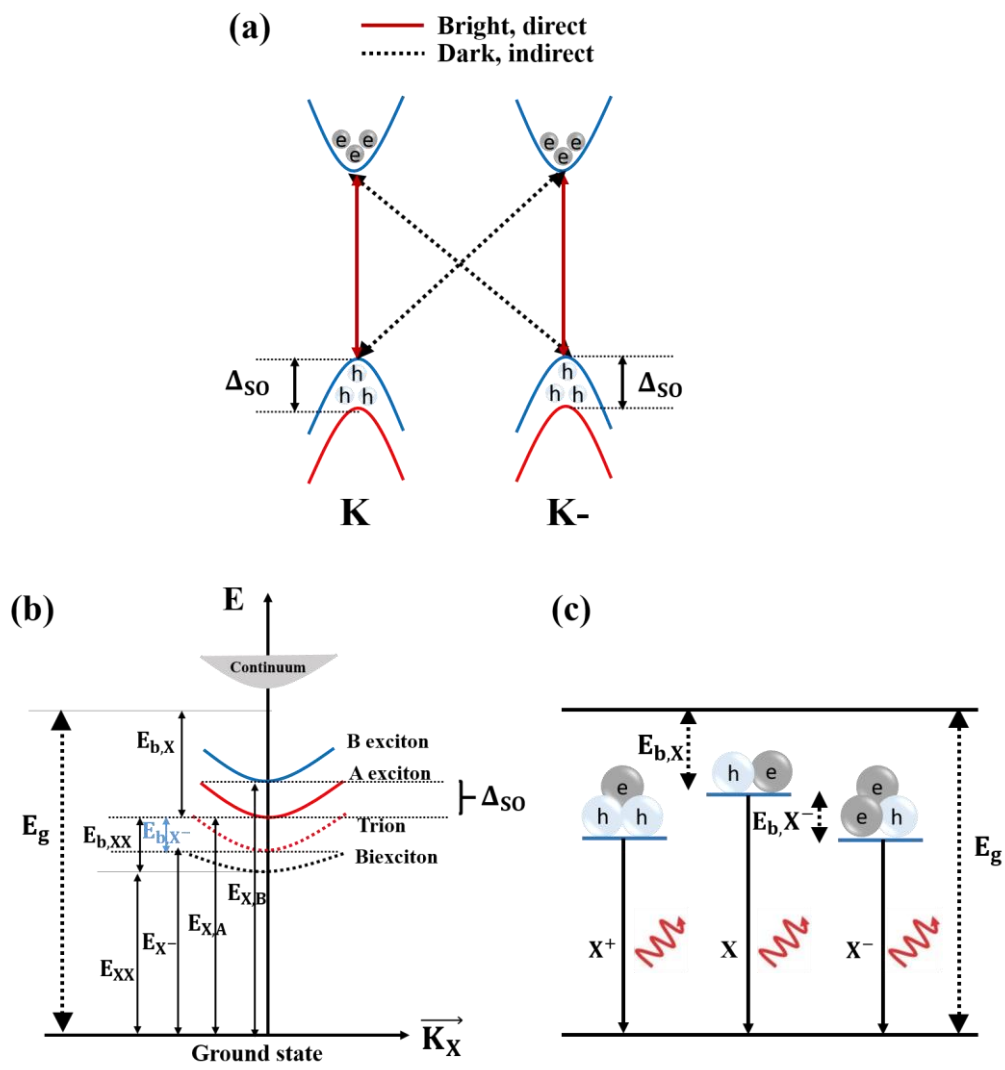

Figure 1.5 (a) Band structure of TMD materials. The four possible exciton formations in K and K- valleys. Two of them are intravalley excitons, bright one (red solid arrows), the other two are intervalley excitons, dark one (grey dotted arrows). (b) Energy levels of the exciton, trion, and biexciton as a function of exciton center of mass wave number $\vec{K}_X$. Different parabolas correspond to the dispersion relation curves of trion, A, B exciton, and biexciton. E_{XA}, E_{XB}, E_{XX}, E_{X^-} are emission energy of A, B exciton, biexciton, and trion, respectively. And $E_{b,X}$, $E_{b,XX}$, E_{b,X^-} are binding energy of A exciton, biexciton, and trion. (Fig.(a) and (b) reproduced from ref.[51]) (c) Schematic of electron and hole configuration in neutral (X) and charged excitons (X^+, X^-). Relevant energies denoted: bandgap energy (E_g), exciton ($E_{b,X}$) and trion binding energy (E_{b,X^-}) (Fig.(c) reproduced from ref.[50]).

The energy of neutral exciton (X) is less than the bandgap energy and is denoted as exciton binding energy, E_{bX}. The exciton binding energy defined as its lowered energy compared to the free electron-hole pair.[52] According to Equation 1.3, the exciton binding energy E_{bX} is determined from the gap between the exciton state and single-particle bandgap, $E_{bX}(n) = E_g$ -

E_X, (Fig. 1.5(b)). However, it is impossible to directly extract the exciton binding energy from conventional absorption or luminescence spectra, because of ambiguous estimation of onset of the direct band to band transition. The trion binding energy is the appropriate energy that the system needs to remove the extra electron or hole from the neutral exciton. In PL spectra, corresponds to the separation between neutral exciton emission energy and charged exciton (X^+ or X^-) emission and is defined as E_{bX}-=E_X-E_{X^-}. In TMDs, strong excitonic properties are observed. Due to their 2D nature and the strong Coulomb interaction, the binding energies are large and sharp. Are well-defined and typically measured with PL spectroscopy.[32,36,38] Moreover, several recent studies have also demonstrated the generation of other exciton complexes, such as biexcitons (two bound electron-hole pairs) or localized states (due to residual impurities, defects, and disorder effects), in monolayer dichalcogenides.[36,37,53–55]

1.4 Spin-Valley Polarization and selection rules

It has theoretically demonstrated that the inversion symmetry breaking in 2D materials leads to contrast circular dichroism in different k-space regions, which takes the extreme form of optical selection rules for interband transitions at high symmetry points.[56]

Since inversion symmetry has inherently broken in monolayer TMDs due to two different types of atoms (metal and chalcogen), these materials have great promise for valleytronics and valley dependent physics. As a result of inversion symmetry, the valleys of energy-momentum dispersion located at the corners of the hexagonal Brillouin zone (K, K-). Among the six corners of the Brillouin zone, there exist two sets of three equivalent points. We have two inequivalent valleys, which form a time-reversal pair with each other. Because the valleys are well separated from each other in momentum space, the intervalley scattering is relatively weak. This leads to a long-lived valley and spin polarization.[57] The main objective is to control the valley index similarly with the manipulation of the spin in semiconductors. The critical quantity is the orbital magnetic momentum m(k). This quantity is characterized by symmetry considerations: (i) time-

reversal symmetry, m(k)=-m(-k) (ii) space-inversion symmetry, m(k)=m(-k). The m(k) does not vanish under time-reversal operation, so it has opposite values once an inversion symmetry has broken in the system (monolayer TMD).

The lack of inversion symmetry together with spin-orbit coupling making possible spin and valley control in monolayer dichalcogenides. Since time-reversal symmetry's forces opposite spin-splitting at each valley, we can control the valley polarization.[11] Also known as spin-momentum locking, the result is that in a specific valley at the valence band maximum, the spin is "locked" to a particular direction. The K valley would correspond to optical selection rules of a certain helicity as well as carriers of a fixed spin, while the K- valley would correspond to opposite conditions. The ability to control carrier spin and carrier confinement within a specific valley with circularly polarized light in TMDs was first experimentally demonstrated in 2012 [58–61] and has been crucial to the research progress TMDs ever since. The time-reversal symmetry ($E_{\uparrow}(k) = E_{\downarrow}(-k)$) requires the spin splitting in opposite valleys to be opposite, different valleys will have opposite spin at the same energy.[11]

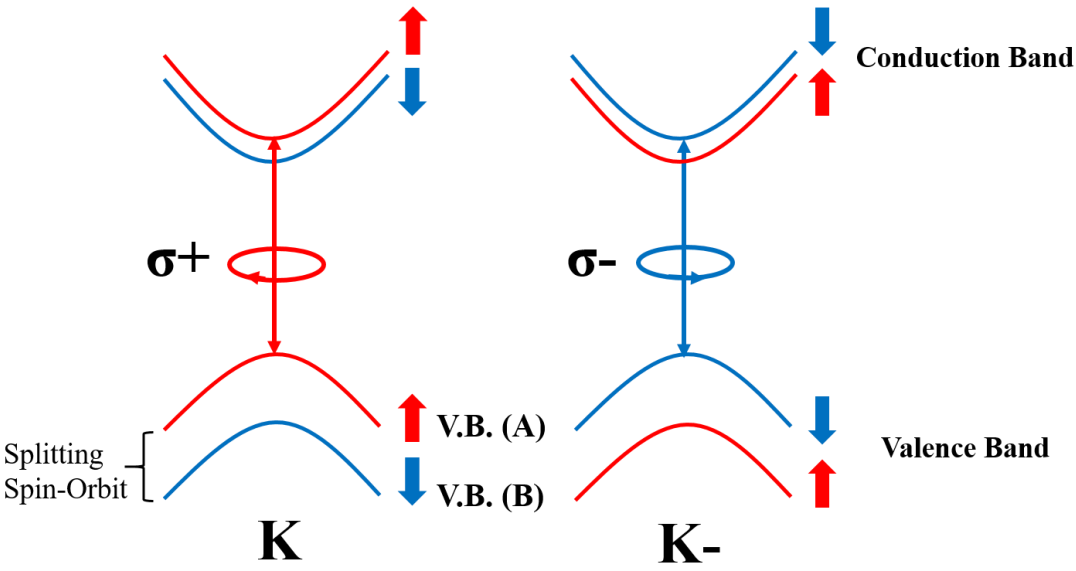

Figure 1.6 Spin-Valley Optical Selection Rules. Due to the spin-valley coupling, when a specific energy level is excited in a valley using circularly polarized light, a spin polarization will also be created. Here, the spin-splitting in the conduction band is assumed to be negligible.

Fig. 1.6 shows the optical selection rules from the top of the spin-split of the valence band to the bottom of the spin-split conduction band in a monolayer TMD. The large spin-splitting in the valence bands has induced by the spin-orbit coupling. At the K valley, the spin-up and spin-down holes occupy the valence band (A) and the valence band (B), respectively. While at the K- valley the spin occupation is the opposite. Light with σ+ circular polarization (red arrow) generates spin-up holes and spin-down electrons in the K valley. The excitation on the K- valley is the time-reversal of the above.

The optical properties of monolayers TMD are dominated by excitons. The valley polarization can be probed through charged and neutral exciton emission. When an electron and hole are at different valleys, their direct recombination is forbidden (dark exciton) since the momentum conservation cannot be satisfied. If the electron and hole are in the same valley, their recombination and photon emission are possible. The B excitons lifetime is much shorter due to relaxation to the lower energy configurations through fast non-radiative channels. In the following paragraph, we will focus only on neutral excitons (A excitons).

At the K valley, only spin-up holes populate valence band maximum A, an A exciton at the K valley formed by a spin-up hole with a spin-down electron. At the K- valley, an A exciton is formed by a spin-down hole with a spin-up electron. Based on these selection rules, a circularly polarized light can inject spin- and valley-polarized excitons, which in turn recombine and emit circularly polarized photoluminescence.

In the case of charged excitons (X±), the selection rules consist of four possible configurations, three for the negative (X^-) and one for the positively charged exciton(X^+). The holes in the K valley have spin-up states and holes in the K- valley have spin-down states, due to the large spin-valley coupling. At the K valley, only spin-up holes populate the valence band maximum. Negatively charged excitons have formed by an electron-hole pair with a spin-up (-down) electron from the conduction band minimum at the other K- valley. It is also possible to form a

negatively charged exciton through a bound electron-hole pair, which captures an electron from the other conduction band minimum at the same valley.

All the other configurations are the time-reversal equivalent of the ones described below.

One further result of the lack of inversion symmetry combined with strong spin-orbit coupling is the prediction of long spin and valley lifetimes in TMDs. The large momentum difference between the two valleys prevents scattering between the valleys. It is expected that the spin and valley lifetimes in TMDs will be long, which is ideal for spin- and valleytronic applications.[11]

1.5 Vibrational Properties

Similar to their optoelectronic properties, the vibrational properties of TMDs critically depend on the number of layers. The vibrational and phonon characteristics of TMDs have been investigated theoretically and experimentally. The 2H-MX_2 crystal structure of the TMDs belongs to D_{6h} point group. The 6 atoms per unit cell result in 18 lattice dynamical modes at the Γ-point of the hexagonal Brillouin zone. Phonons belonging to these modes can be represented as Eq. 1.4.[62]

$$\Gamma = A_{1g} + 2A_{2u} + B_{1u} + 2B_{2g} + E_{1g} + 2E_{1u} + E_{2u} + 2E_{2g} \qquad (1.4)$$

In the monolayer and an odd number of layers (odd N) the symmetry is reduced to the D_{3h} point group. Therefore, an odd number of WS_2 layers do not have a center of inversion. The Γ-point phonon modes transform according to the following representation:[63]

$$\Gamma = 2A_2'' + A_1' + 2E' + E'' \qquad (1.5)$$

Raman Spectroscopy emerges as the ideal tool to study these vibrational properties.[22] Indeed, it offers a fast and unambiguous method to determine the number of layers and to probe the electron-phonon interactions.[17,64] Fig. 1.7 shows the calculated phonon dispersions relation for single-layer WS_2.

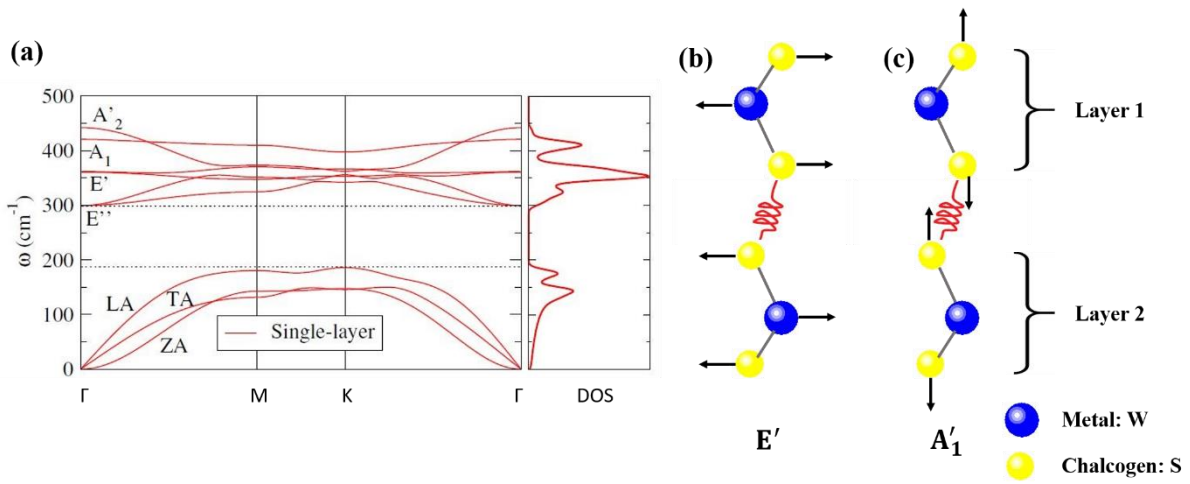

Figure 1.7 (a) Phonon dispersion curves and density of states of single-layer WS_2.[65] (b) Phonon modes in-plane E', and (c) the out-of plane phonon mode A_1' for two adjacent layers, the red spiral lines represent the weak inter-layer van der Waals interaction. (Fig. (b) and (c) reproduced from Ref. [65]).

One A_2'' and one E' are acoustic modes, another A_2'' is Infrared active, A_1' and E'' are Raman active, and another E' is both Raman and Infrared active. For monolayers, the E', which is an in-plane mode involving vibration of both metal and chalcogen atoms, as well as A_1', which is an out-of-plane mode involving only chalcogen atoms, are the two primary Raman modes. These two peaks tend to dominate the spectrum of any TMDs, whether monolayer or few-layers or bulk. Representative Raman spectrum for single-layer WS_2 is shown in Fig. 1.8. In the figure, we observe two Raman peaks at 356 cm^{-1} and 417 cm^{-1}. They represent the well-known active Raman modes E' and A_1', corresponding to the in-plane and the out-of-plane phonon vibrational modes, respectively. The in-plane mode E' tends to be unaffected by the number of layers due to weak van der Waals forces between the layers but can be slightly redshifted as the number of layers increases. As seen from Fig. 1.8, the E' peak at 356 cm^{-1} is overlapping with another strong peak, the 2LA(M) peak at 351 cm^{-1} which is a longitudinal acoustic mode caused by in-plane collective oscillations of W and S atoms. The second strong peak at 417 cm^{-1}, is the A_1' peak caused by out-of-plane vibrations. It is much more sensitive to the number of layers and blueshifts as the number of layers increases. This has been attributed to the restorative forces as well as the raising in the dielectric screening of the Coulomb forces. Combine both the shifts

in frequency with the changing number of layers, the difference between these two peaks used to identify the number of layers in TMDs. The difference in the frequency, for monolayer WS_2, of the two main Raman vibration modes (E', A_1') is ~60cm^{-1}, which is used as a fingerprint for the character of the sample.[62]

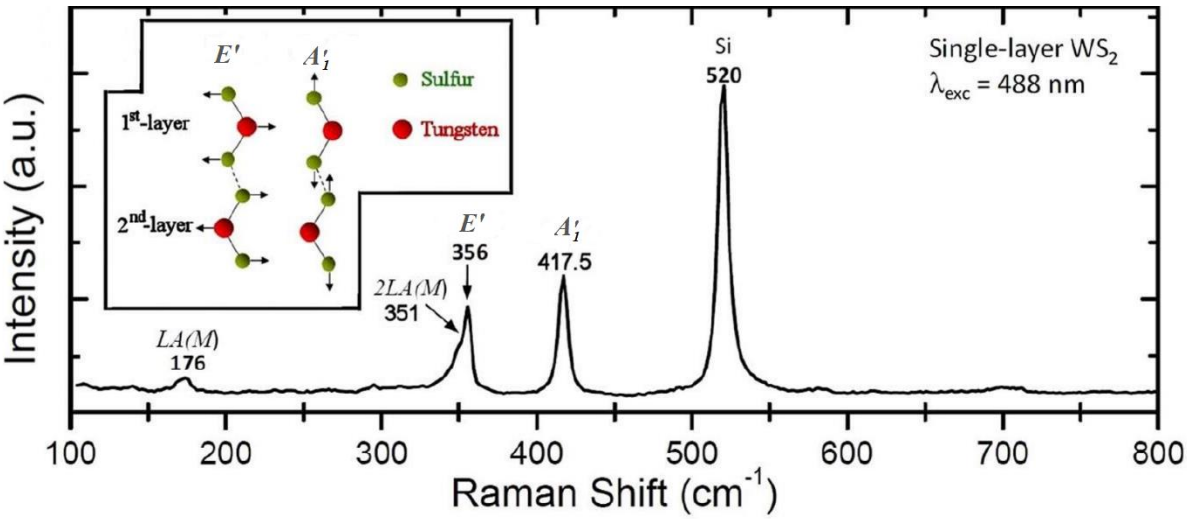

Figure 1.8 Room-temperature Raman spectra from a monolayer WS_2 region, using 488 nm laser excitation. The inset shows the atomic displacements for the in-plane phonon mode E' and the out-of-plane phonon mode A_1'.[66]

As the number of the layers in the TMC system increases from monolayer to bulk, the out-of-plane phonon mode becomes stiff and the in-plane bonding is relaxed, which leads to the blue and redshifts of the A_1' and E' modes, respectively. The increase in the temperature also results in spectral broadening and a redshift of both A_1' and E' modes. It found that the E' mode is not affected by electron doping, while the A_1' mode, as in the case of temperature increase, undergoes a redshift and an increase in the peak width.[67]

1.6 Graphite and Graphene

All carbon materials are available in multiple atomic structures. Graphene consists of carbon atoms tightly packed in a hexagonal lattice. Each hexagonal is made of 6 carbon atoms, referred to as a honeycomb lattice. Each carbon atom has four bonds, one σ- bond with each of three

neighbors and one π-bond oriented out-of-plane, above and below the graphene sheet and are highly mobile. The σ-bond made of a combination of hybridized orbitals (2s, $2p_x$, $2p_y$) or sp^2. The π-bond refers to the remaining p_z orbital and determines the low-energy electronic structure of graphene.[68] When layers of graphene are stacked together formed bilayer, tri-layer, or few layers of graphene that are electronically coupled. Graphite is many layers of graphene held together by weak van der Waals forces (Fig. 1.9).

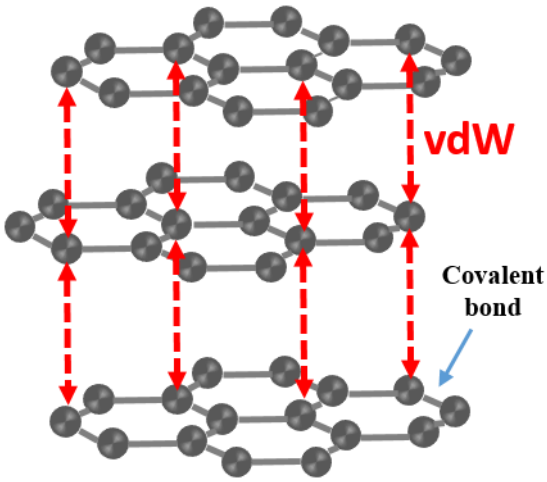

Figure 1.9 Van der Waals forces between graphene layers in bulk graphite.

Graphene is a zero-gap semiconductor, with a linear E vs k (unlike a 2D electron system which has parabolic bands) and charge carrier with zero effective mass and semi-metallic behavior. The conduction and valence band touch each other at the Brillouin zone corners. The touched point is referred to as the Dirac point.[69] It has unique electronic properties that make it promising for next-generation devices. However, graphene's lack of bandgap forces the scientific community explores the field beyond graphene. The bandgap is necessary for the on/off state of a transistor and the emission or absorption of the light.

Graphite is the most stable form of carbon under standard conditions and is a layered hexagonal crystal. Each layer is one atomic thick graphene sheet. Compared with the strong sp^2 intralayer bond, the interlayer interactions are controlled by weak van der Waals bonding. This contrast leads to many physical and mechanical properties of graphite, such as maximum values of

electric and thermal conductivities, in-plane elastic stiffness, and strength. These novel properties make graphite and graphene of intense interest for a wide range of applications. In this thesis, we explore these materials as a supporting layer of TMDs.

In basic terms, graphene is described as a single, one atomic thick layer of the commonly found graphite. Graphite is consists of hundreds or thousands of layers of graphene. In actuality, the structural morphology of graphite and graphene, and the method to create one from the other, is slightly different. Raman Spectroscopy can estimate the number of graphene layers and defines the limit between graphene and graphite.[70,71]

When a 2D material is stacked with another 2D material, the resulting structure is a vertical 2D heterostructure. Nevertheless, the layers are mostly composed of different types of crystals. Such stacked structures are entirely different from the usual 3D semiconductors heterostructures. The charge transfer between the layers is significant and can, in turn, induce large electric fields, thereby offering exciting possibilities in band-structure engineering. The optical and electronic properties are strongly dependent on the supporting layer of 1L-TMD.

Chapter II
Carrier modulation in 2D TMDs

2.1 Doping strategies in 2D TMDs

Tuning the properties of TMDs is essential to improve their performance and expand their applications. This chapter classifies the various doping methods of 2D TMDs and summarizes how the dopants interact with the materials. The performance of the materials depends on the synthesis methods and the species of the dopants. The synthesis methods and the dopant atoms greatly influence the morphologies and properties of these materials. Selecting both of them are critical. The doping methods and the resulting enhanced properties of 2D TMDs are reviewed at this point.

The principles of the doping strategy can be mainly categorized as (i) charge transfer, (ii) substitutional, (iii) intercalation, and (iv) electrostatic doping.

The charge transfer doping has attracted much attention in modulating the electronic behavior of semiconductors. In charge transfer doping, contact is established through either physical or chemical interactions between the host and dopant materials.[72] In contrast to substitutional doping with foreign dopant atoms incorporated into the lattice, the charge transfer doping takes advantage of charge transfer interaction between host material and any adjacent mediums, including atoms,[73–75] ions,[76] molecules,[77–92] particles and supporting substrates.[93,94] The Fermi level difference between the dopant and the host materials determines the charge transfer direction and whether the adsorbed dopant act as an acceptor or donor. When the dopant exhibit a lower Fermi level (E_F) than the host semiconductor, electrons are withdrawn from the semiconductor to the dopants, thus causing p-type doping. Conversely, n-type doping is obtained when the dopants have higher E_F than the semiconductor. For gas molecules, a similar analysis is made by considering the electron negativity, with the oxidizing molecules like O_2, NO_2 as the p-type dopant, while reducing molecules as the n-type dopants. [95]

Substitutional doping is based on the change in the total number of electrons in the compound by selecting a dopant having one more or one less electron in its valence shell than the

substituted atom. In MX_2, both cation and anion elements can be substitutionally replaced by foreign atoms. Depending on the number of valance electrons in the dopant atom, the MX_2 doped into n-type[96] or p-type conductance.[97] This is confirmed from the first-principles calculations showing the Fermi level shifting.[98–101] This method can induce strain[102] and phase transitions via chemical functionalization,[103] to the TMDs. Plasma functionalization is an efficient way to incorporate foreign atoms, such as hydrogen,[104105] nitrogen,[102] fluorine,[106] and phosphorus[107] in MoS_2, via anion substitutional doping. Substitutional doping can tailor both the material's bandgap and crystalline structure, as demonstrated theoretically[108,109] and experimentally. [92,79,110–119]

Intercalation doping: The van der Waals interlayer coupling in 2D materials enables the intercalation of foreign ions,[120–122] atoms,[123–126], and even molecules into the rather large interlayer space.[79,92] Such intercalation has been earlier used to exfoliate 2D materials in solutions, [3,127] and was generally exploited in batteries and electrochemical cells.[120,121] The two main sources of intercalation doping of 2D TMDs are H or alkali metal intercalation and zerovalent intercalation occurs with heavy metal elements.

Recently, the intercalation was also shown to be able to modulate the crystal lattice and electronic structure of host materials, thereby allowing a series of physical or chemical phenomena, including semiconductor-metal transition, charge density waves, and superconductivity.

Electrostatic doping is a technique in which charge carriers (electrons and holes) are induced in a semiconductor material due to band alignment near its interface with another contacting/semiconducting material. The concept of electrostatic doping, also defined as gate-induced charge, is a unique feature of nano-sized structures such as 2D materials. In a device composed of ultrathin crystals, a positive gate bias induces an electron population that spreads over the entire body (volume inversion or accumulation). This effect is different from the

charge-sheet interface layer formed in bulk semiconductors. The thinner the film, the more uniform the volume carrier distribution. The original undoped body suddenly behaves as an n-doped region. Changing the polarity of the gate bias turns the body into a p-type region. Due to the ultrathin nature, thin flakes of 2D materials are particularly perceivable to external field effects. This characteristic lead to the electrostatic doping strategy to tailor the carrier doping concentration and polarity in semiconductor 2D MX_2. Since the strategy is based on capacitance coupling between the external gate and 2D channels, it is known to exhibit ubiquitous advantages in non-destructive, reversible, stable, and durable regulation and industrial availability. [47,50,52,128–131]

Electrically tunable emission between X^-,X^+ and X has been observed in TMDs (1L-$MoSe_2$[50], WSe_2,[53] and WS_2[52]). The definition of the exciton binding energy of monolayer WS_2 with linear differential transmission spectroscopy and two-photon photoluminescence (2P-PLE) has been clarified. Similar work [47] demonstrates the spectroscopic identification in a monolayer MoS_2 field-effect transistor of tightly bound negative trions. These quasiparticles, which can be optically created with valley and spin-polarized holes, have no analog in conventional semiconductors. They have large binding energy (~20meV), even at room temperature.

In the following subchapters, we will review the response of TMDs to doping effects and how we can recognize the changes in materials properties with the Raman and Photoluminescence Spectroscopy, as well as the modulation of circular polarization.

2.2 Doping effects in the Raman Scattering

Two-dimensional materials are sensitive to perturbations due to the large surface–volume ratio. A widely used non-destructive experimental technique to characterize these perturbations is Raman spectroscopy. Raman Spectroscopy is a powerful method for probing changes in material properties by analyzing shifts in the phonon peaks. In the presence of external perturbations such as strain, stress, magnetic fields, charge doping, temperature, and defects, the electronic and lattice vibrations change significantly. These changes are identified by shifts in the Raman spectrum. [85,90,91,95,132–139]

This chapter mainly reviews several possible doping strategies for 2D TMD crystals and the effect on their vibration properties.

Raman spectroscopy can be quite useful and requires precise knowledge and understanding of the phonon renormalization of a single TMD layer as a function of the carrier concentration. Electron doping in single-layer TMD results in softening specifically of its Raman-active A_1' phonon, accompanied by an increase in the linewidth of its Raman peak. In comparison, the other Raman mode with E' symmetry is insensitive to electron doping. A_1' mode has stronger electron-phonon coupling than the E' mode, confirmed with first-principles DFT calculations and symmetry arguments.[133]

Theoretical calculations show that monolayer TMD is a direct bandgap semiconductor with a bandgap at the K point. Valence- and conduction-band edges primarily consist of metal 4d states with some hybridization with sulfur 3p states. In particular, states near the bottom of the conduction band near the K point have a character of the d_z^2 state of metal, and that at the top of the valence band has a d_{xy} character. We note that the charge density ($|\psi(r)|^2$) associated with each of these states has a full symmetry of the TMD layer, which has significant consequences for electron-phonon coupling. Electron doping leads to the occupation of the bottom of the conduction band at K-point states and has a character of d_z^2 of metal. The $|\psi(r)|^2$ of the states

near the K point also transform according to the identity representation A_1'. Hence, changes in occupation of these states with electron doping yield a remarkable modification in the e-ph coupling of the A_1' phonon. In contrast, the coupling of the E' mode with electrons is weakly dependent on doping. Frey et al.[140] put forward similar conclusions.

These results show how Raman scattering is useful to characterize the level of doping on a single-layer TMD.

Figure 2.1 shows the evolution of zone-center phonon E' and A_1' modes of the MoS_2 monolayer at different top-gate voltages. The A_1' phonon involves the sulfur atomic vibration in the opposite direction along the c axis (perpendicular to the basal plane), whereas for the E' mode the displacement of Mo and sulfur atoms are in the basal plane. The profile of the line-shape was obtained by fitting a sum of two Lorentzian functions of the data. Figures 2.1 (b) and (c) show the shift of the mode frequencies and the corresponding full width at half maximum (FWHM), respectively, as a function of gate voltage.

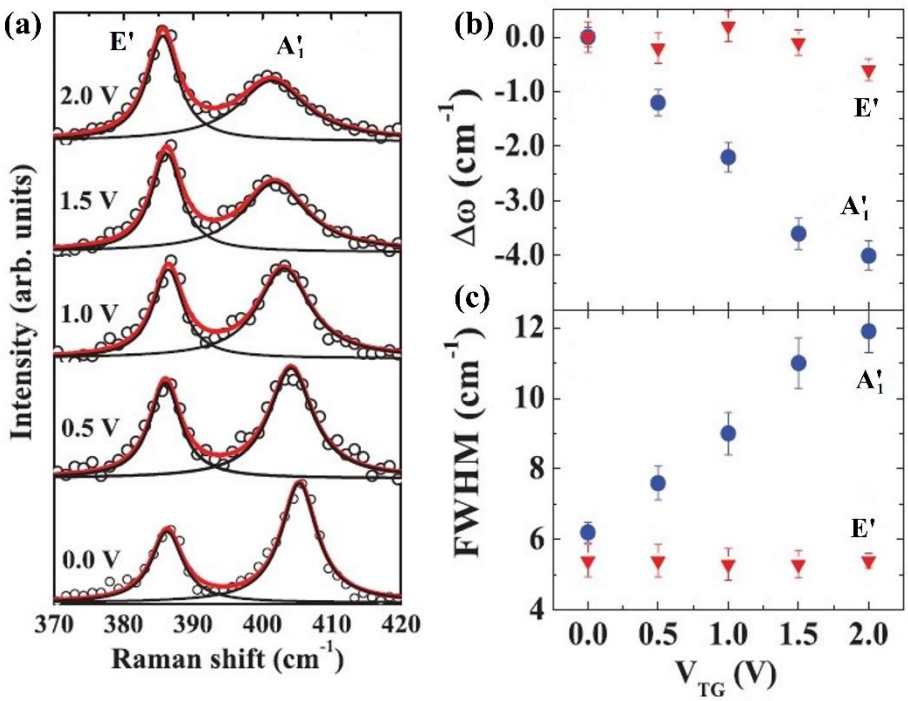

Figure 2.1 (a) Raman spectra of monolayer MoS_2 at different top-gate voltages V_{TG}. Open circles are experimental data points, the gray (red) lines are Lorentzian fits to the total spectra, and the black lines are the Lorentzian fit to the individual peak. Change in the (b) phonon frequency ω and (c) FWHM of A_1' and E' modes as a function of V_{TG}. [133]

By adding extra electrons to a monolayer MoS_2 the symmetries of the system are preserved. In Fig. 2.2 (a) are presented the Raman spectra for the 1L-MoS_2 with electron doping. The frequency of the E´ peak is not sensitive to doping, but the position of the A_1´peak with electron doping.[132] Lin et al. [91] report effective and stable electron doping of monolayer molybdenum disulfide (MoS_2) by cesium carbonate (Cs_2CO_3) surface functionalization. A typical Raman spectrum of as-prepared monolayer MoS_2 is shown in Fig. 2.2 (b) (blue line). The out-of-plane A_1' and in-plane E' Raman frequencies were red-shifted after the decoration of Cs_2CO_3 (red line). The A_1' phonon frequency downshifted by 3.6cm^{-1}, accompanied by a reduction in peak intensity and peak broadening. In contrast, only a 1.7cm^{-1} frequency shift was observed for the E' phonon with almost unchanged peak intensity and peak full-width at half-maximum (FWHM).

Controlling the growth thickness of Al_2O_3 layers could be regarded as a valid method to change the contact areas between gas molecules and MoS_2, allowing the gas molecules doping.[85] Fig.2.2 (c) demonstrates the interactions between gas molecules and monolayer MoS_2. In monolayer MoS_2, n-type doping usually could induce a red-shifting of out-of-plane Raman mode (A_1') due to the electron-phonon interaction and the peak-position of in-plane Raman mode (E') is almost unaffected.

One-step NaCl assisted Chemical Vapor Deposition method was employed to successfully synthesize large-area monolayer p-type Nb-doping MoS_2 directly on SiO_2 substrate.[118] DFT calculations confirm that substitutional Nb-doping in MoS_2 would shift the Fermi-level down to valance band maximum and induce impurity level close to VBM, leading to p-type doping. Raman spectroscopy was employed to demonstrate the doping effect using a 532nm excitation laser. Fig. 2.2 (d) shows the Raman spectra of pure MoS_2 and Nb-doped MoS_2. For Nb-doped MoS_2, both vibrational modes show a blue shift compared with the pure MoS_2. The shift in Raman spectra is affected by the coexistence of strain and charge doping. The p-type

substitutional Nb-doping in MoS_2 occurs during the growth process, which leads to the distorted lattice and injection of holes, inducing tensile stress and reducing the electron-phonon scattering.

Peimyoo et al. [90] have demonstrated that neutral and charged exciton emission can be tuned through adsorption of the electron-withdrawing dopants of F_4TCNQ and H_2O. The adsorption of F_4TCNQ molecules reduces the electron concentration in 1L-WS_2. Raman measurements were conducted before and after doping. Fig. 2.2 (e) shows the variations of Raman peak frequencies with doping. It is found that the A_1' mode slightly blue-shifts by 2cm^{-1} after the early few steps of F_4TCNQ deposition, while the peak position of the E' mode does not change. Thus, the observed Raman results indicate the F_4TCNQ/1L-WS_2 sample is less n-doped than that of 1L-WS_2 due to the charge transfer during F_4TCNQ adsorption.

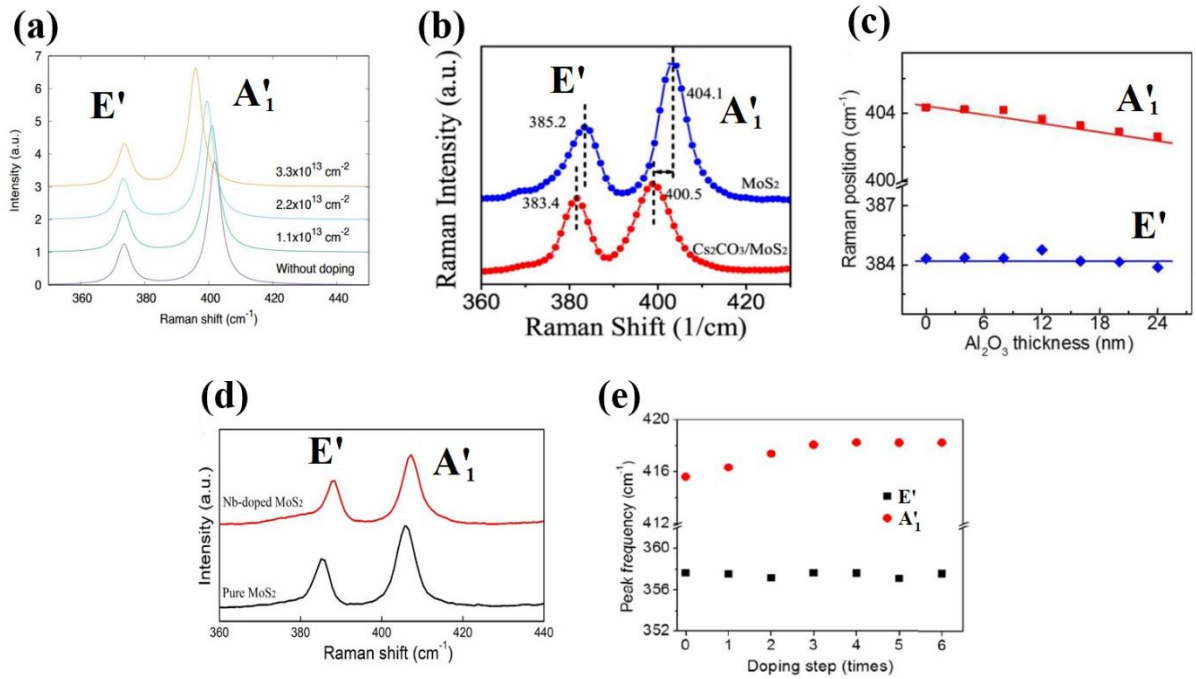

Figure 2.2 (a) Effect of electron doping on the Raman spectra of a monolayer MoS_2 (n-type doping).[132] (b) Raman spectra of 1L-MoS_2 before (blue line) and after (red line) Cs_2CO_3 doping at room temperature (n-type doping).[91] (c) Gas molecules doping in monolayer MoS_2 - The peak position of out-of-plane mode (red quadrate) and in-plane mode (blue rhombus) as a function of Al_2O_3 growth thickness, respectively.[85] (d) Raman spectra of monolayer MoS_2 and Nb-doped MoS_2 under 532 nm laser excitation (p-type doping).[118] (e) Peak frequencies of the E' and A_1' modes versus doping step of F_4TCNQ deposition for 1L-WS_2 (p-type doping).[90]

Molecular reductants (n-type doping) and oxidants (p-type doping) are introduced onto monolayer TMDs, specifically MoS_2, WS_2, $MoSe_2$, and WSe_2.[135] Doping is achieved by

exposing the TMD surface to solutions. Raman spectroscopy was performed to explore the effects of the solution dopants on the phonons of the host MX_2. Fig. 2.3 (a) and (b) summarizes the Raman spectra of monolayer MoS_2 before and after doping treatment. The peak positions as a function of doping for the two main vibrational modes of MoS_2 (in-plane and out-of-plane) are plotted in Fig. 2.3 (b). For MoS_2, and the other three MX_2 materials, the n-type doping leads to the redshifting (to lower energy) for both vibrational modes, whereas p-type doping leads to the blueshift (to higher energy) for both modes.[133] This is consistent with previous studies, which observed that higher electron concentration in the n-doped film increases electron-phonon scattering.[91] Whereas p-doping reduces the electron–phonon scattering as referred to previously reported effects of doping for TMDs.[141] As shown in Fig. 2.3 (b), the A_1' mode is more sensitive than the E' mode does since the A_1' mode couples much more strongly with electrons.[132,133] The Raman shift of the A_1' mode on the n-doping side is larger than the p-doping side. This result also confirmed that p-doping is less efficient than the n-doping for MoS_2.[133]

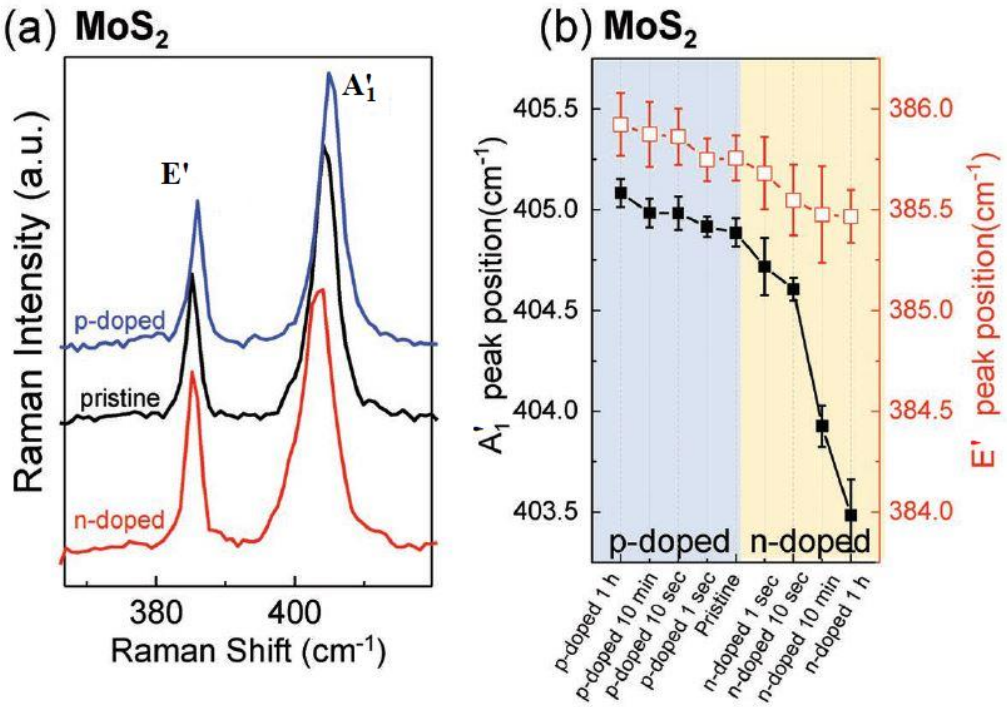

Figure 2.3 (a) Raman spectra of monolayer MoS_2 before and after different treatments. (b) E' and A_1' peak position shifts upon doping with various dopants.[135]

After this literature review, we conclude that there are plenty of different approaches to doped 1L-TMDs. In a typical 1L-TMD, the out-of-plane A_1' mode is susceptible to the charging effect and redshifts with the electron doping, but the in-plane E' mode is not affected by the doping effect, which is due to the strong electron-phonon coupling with the out of- plane mode.[133] On the contrary, the E' mode is sensitive to strain and red-shifted with increasing both uniaxial and biaxial strain, while the A_1' mode remains unchanged.[136,137]

Trying to take advantage of the powerful UV lasers, we used a unique approach to induce carriers in the crystal structure of a 1L-TMD. This method and its effects on Raman Spectroscopy will present in detail in Chapter IV.

2.3 Evolution of photoluminescence under charged carrier doping

The remarkable properties of 1L-TMDs make them potential candidates for nanoelectronics and optoelectronics applications. The large exciton and trion binding energy contribute to be stable even at room temperature. However, the excitons and trions are very sensitive to external factors, including strain, the dielectric of the surrounding environment, electrical and chemical doping, and temperature. Here we review the impacts of several doping approaches on exciton responses reflected via photoluminescence spectra for a monolayer of TMDs.

The evolution of the photoluminescence spectra with charged density obtained the competition between neutral exciton and trion. The formation of trion from neutral exciton and free electron (hole) is expressed by the following equation: $X^0 + e\ (h) \rightarrow X^-\ (X^+)$. The relation between the concentration of neutral exciton n_X, trion n_{X^-}, and free charged carrier n_e modeled by the law of mass action[50,142]:

$$\frac{n_X n_{e(h)}}{n_{X^-}} = \frac{4M_X m_{e(h)}}{\pi\hbar^2 M_{X^-}} k_B T \exp\left(-\frac{E_{bX^-}}{k_B T}\right) \tag{2.1}$$

where T is the temperature, k_B is Boltzmann constant, E_{bX^-} is trion binding energy, and $M_X=m_e+m_h$, $M_{X^-}= 2m_e+m_h$, or $M_{X^+}=me+2m_h$ is the effective mass of neutral exciton, negative trion, or positive trion. Equation (2.1) shows that the ratio of neutral exciton and trion concentrations is governed by free charged carrier density that pushes the chemical equilibrium forward and backward.

The solid understanding of optical properties of 1L-TMDs is essential for implementing them in future devices. In this regard, there have been remarkable efforts focusing on investigating PL spectra of monolayer TMDs as a function of carrier doping concentration via electrostatic or chemical doping.

Under electrostatic gating: The density and polarity of charge carriers in monolayer TMDs can be systemically modulated by electrostatic gating in a FET configuration. By using this

method, Mak et al. in 2012 reported trions in 1L-MoS_2 modulated by charged carrier concentration.[47] Similar studies have carried on other 1L-TMDs.[50,54,49] Fig. 2.4(a),(b),(c) demonstrates the variation of A exciton peaks in PL spectra of intrinsically negative doping channels such as WS_2 [54] with different applied gate bias. Photoluminescence spectra consist of two different peaks. The higher energy peak is the A^0 neutral exciton, and the lower one is the A^- negative trion. The spectra weight of neutral exciton peak is enhanced and becomes dominant in PL spectra when the channel is charge neutrality corresponding to negative gate bias. With sweeping gate bias to the positive side, it gradually decreases and goes to zero at a critical point of electron doping concentration. Meanwhile, the integrated intensity of the trion peak is nearly unchanged with gate bias. Consequently, the total PL integrated intensity follows a similar increasing trend to that of neutral exciton as a function of gate bias (Fig. 2.4 (c)).

In the case of $MoSe_2$ (Fig. 2.4(d)), under negative gate bias V_g, the sample is hole-doped, which favors excitons combining with free holes to form positive trions. When V_g decreased, more holes are injected into the sample, resulting in conversion from neutral excitons to positive trions. With positive V_g, a phenomenon occurs likewise for free electrons to form negative trions. The positive and negative trion resonances have close energy levels, which means nearly identical binding energy between them, subsequently the approximately same effective mass of electron and hole in monolayer $MoSe_2$. The reversible conversion of neutral exciton intensity to the saturated trion PL indicates conservation of the total number of the neutral exciton to trion under gate voltage bias and similar radiative decay rates for both quasi-particles (Fig. 2.4(e)). The conversion dynamics between the integrated intensity of neutral exciton and trion as a function of gate voltage simulated by the mass action model fits well with experimental data.[50]

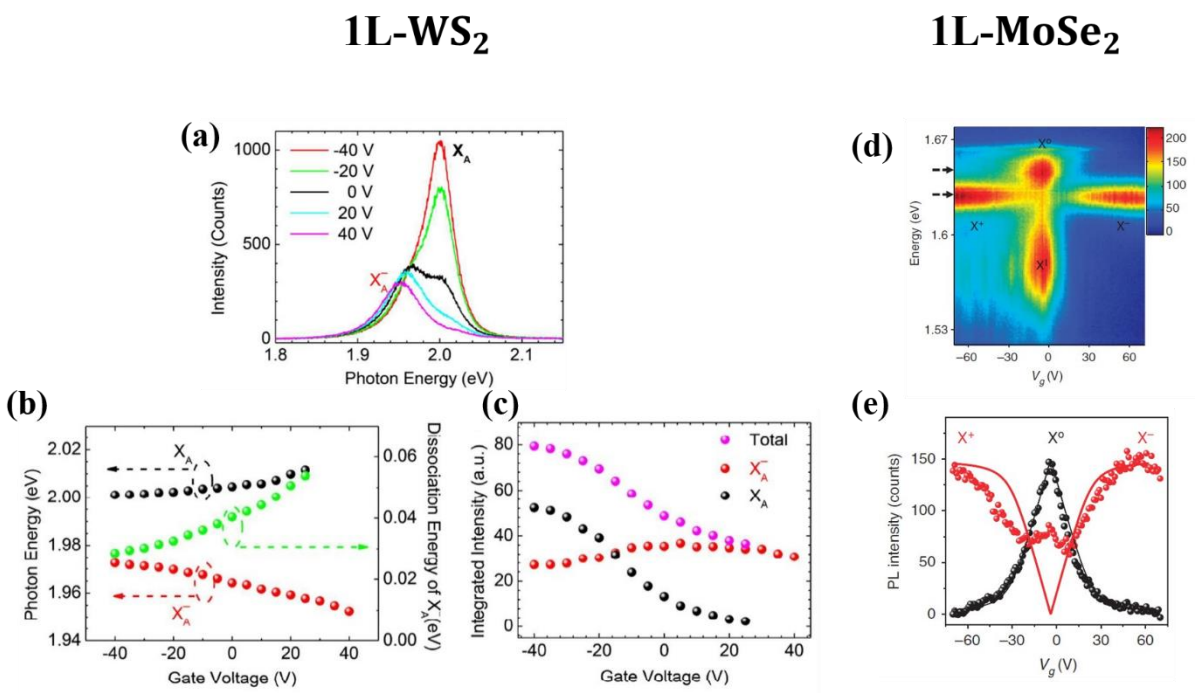

Figure 2.4: Evolution of photoluminescence of 1L-TMDs under electrostatic doping effect. (a) Photoluminescence spectra of monolayer WS_2 taken at different gate biases. (b) The variation of neutral exciton and trion position with various back-gate biases. (c) Integrated intensities of neutral exciton and trion peak. [54] (d) Colour contour map of monolayer $MoSe_2$ PL spectra at 30 K under different back gate biases. (e) The variation of trion and exciton peak intensity with gate voltage. The law of mass action is used to fit for trion and exciton intensity variation with gate bias (solid curves). [50]

Chemically driven tunable PL in TMDs: Besides electrostatic doping, the charge transfer process via interaction with adlayers, atoms, or molecules adsorption is a robust approach towards tuning doping to MX_2 crystals. Chemical doping consists of the adsorption of atoms or molecules on the surface of the TMD. This method leads to the alteration of its electronic structure as a consequence of surface charge transfer. This charge transfer process can induce either electron or hole doping depending on the relative position of Fermi level or electron affinity of doping species concerning conduction band minimum and valence band maximum of host semiconductor. This concept has been practiced in carbon nanotubes and graphene researches.[143,144] There is a wide range of reductants, such as alkali metals,[99] ammonia,[145] amines,[146] and imines,[147] the biological cofactor nicotinamide adenine dinucleotide (NADH),[82] tetrathiafulvalene (TTF),[148] benzyl viologen (BV),[76] hydrogen plasma[83] and cesium carbonate (Cs_2CO_3) surface functionalization[91] used as electron donors for TMD materials. Meanwhile,

oxidizing agents such as NO,[149] NO_2,[145] O_2,[86] tetracyanoquinodimethanes (TCNQ and its tetrafluoro analog F_4-TCNQ),[90,82] found as acceptors.[148] Also, chlorine plasma-induced p-type doping of 1L-MoS_2.[83]

Similar to electrostatic doping, withdrawing or donating electrons in the 1L-TMD offers tunability of its PL spectra. For example, a chemical doping method for the reversible transition between neutral and charged excitons of 1L-MoS_2 using chlorine-hydrogen-based plasma functionalization has been published (Fig. 2.5 (a), (b), (c)).[83] N. Peimyoo et al.[90] have observed enhancement for 1L-WS_2 coated with F_4-TCNQ solution. This enhancement is explained by switching the dominant PL process from radiative recombination of the negative trion to the neutral exciton under extraction of residual electrons. The PL intensity of 1L-TMDs can be easily controlled with varying carrier doping density by the number of dopants (Fig. 2.5 (d), (e), (f)). Mouri et al.[82] reported that the PL intensity of 1L-MoS_2 is drastically enhanced by the adsorption of F_4-TCNQ and TCNQ molecules, while is quenched after NADH solution treatment (Fig. 2.5(g)). Moreover, it found that gas molecules such as O_2, NO, NO_2, and H_2O adsorbing onto the surface of 1L-TMDs serve as charged dopants, strongly affecting PL. A report by Tongay et al. [86] indicates that O_2 and H_2O adsorption serve as a p-type dopant, remarkably enhancing emission efficiency of native n-type 1L-TMDs (MoS_2, $MoSe_2$) due to electron depletion (Fig. 2.5 (h)) while accumulating the majority of holes in p-type TMDs (WSe_2), resulting in strong suppression of the PL. Likewise, the PL intensity of another native n-type 1L-WS_2 also strongly increases as H_2O is drop-casted onto the surface.[90] Finally, in Fig. 2.5 (i), an electron doping of a monolayer MoS_2 has been achieved with Cs_2CO_3 functionalization at room temperature.[91]

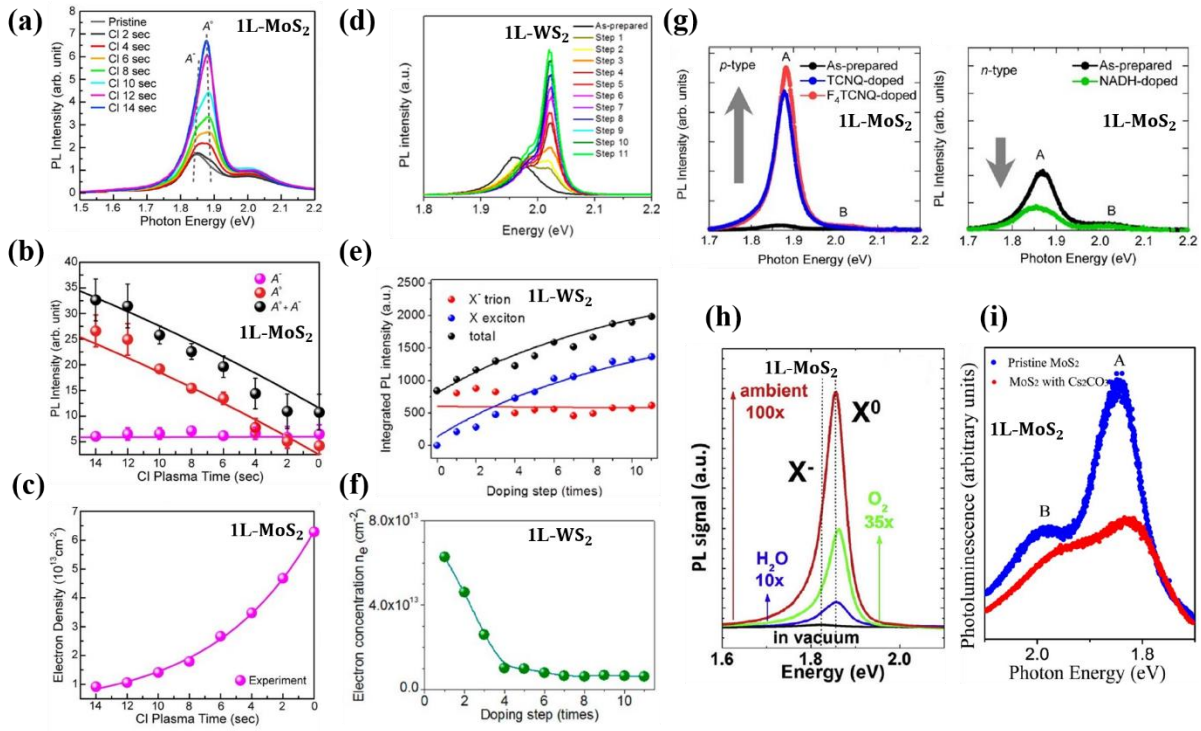

Figure 2.5: (a) Evolution of the PL spectrum of 1L-MoS_2 according to the duration of the chlorine plasma (b) The PL intensities of the excitons, trions, and their total contribution as a function of the plasma treatment time. (c) Electron density as a function of the plasma treatment time.[83] (d) Room-temperature PL spectra of 1L-WS_2 upon consecutive doping with molecular adsorbates F_4TCNQ. (e) Integrated PL intensities of X^-, X, and the sum as a function of doping step. Solid lines are the theoretical calculation results. (f) Calculated electron concentration as a function of F_4TCNQ doping step.[90] (g) Room-temperature PL spectra of 1L-MoS_2 before and after being doped with p-type molecules (TCNQ and F_4TCNQ) (left panel) and after being doped with an n-type dopant (NADH) (right panel).[82] (h) Effects of exposure to different gas species on the PL intensity of annealed monolayer TMDs. Change in PL of MoS_2 (from its annealed but measured in vacuum value) upon exposure to H_2O alone, O_2 alone, and ambient air. The pressure of these gases is 7, 200, and 760Torr, respectively. Trion X^- and exciton X^0 peak positions indicated.[86] (i) PL spectra of 1L-MoS_2 before and after Cs_2CO_3 doping at room temperature.[91]

The result suggests that chemical doping combining provides a simple and effective way to control the electrical and optical properties of 1L-TMDs. The evolution of trion and exciton features as a function of electrostatic or chemical doping provides an efficient approach to manipulate the emission in 1L-TMDs. These results impact the rising of new photonic and optoelectronic devices such as optical detectors, light emission devices, and solar cells.

2.4 Control of valley polarization with different doping approaches

As for the PL and Raman measurements, various approaches were adopted to obtain a sizable circular polarization (P_C), like using different excitation energy,[61,150] temperature,[151] electron-phonon coupling,[61,152], electron-hole exchange,[153], applying a magnetic field, or building van der Waals heterostructure.[58,60,154–160] More practical and desirable methods could be electrical and optical control of valley polarization in TMDs at non-cryogenic temperature and off-resonance conditions. Toward this goal, one of the most effective means is in situ carrier doping by physical or chemical approaches.[54,90,161] The introduced resident carriers in TMDs not only tailor the exciton species but are expected to tune the valley polarization dynamics with large P_C values as well. The changes in valley polarization/relaxation dynamics due to carrier doping have been noticed by many research groups.[53,162–165]

Probing correlations between valley polarization and carrier concentration is crucial for future manipulations and potential applications based on valleytronic properties in TMDs. Recent theoretical studies with an experimentally proved framework based on carrier screening effects on excitonic valley relaxation in 2D semiconductors,[166,167] provide a strategy to enhance P_C. The theoretical investigation focused on the exchange of interactions between electrons and holes.[166] The results show that the valley relaxation time is highly dependent on the extent of carrier doping. Also, a finite degree of doping is predicted to induce additional valley relaxation temperature dependence at low temperatures, an effect that is absent at zero doping. These calculation results suggest a possible increasing the valley relaxation time by tuning carrier doping, which could present a means of handling the valley degrees of freedom.

The temperature dependence of valley relaxation time becomes noticeable at $n > n_0$, and this is obvious in the carrier density dependence of the valley relaxation time shown in Fig. 2.6. Here, they plot the valley relaxation time at various carrier densities. In the case of a low density, the valley relaxation time rapidly decreases with increasing temperature. However, as the carrier

density increased, it exhibits a linear temperature dependence, and the linear dependent region at low temperatures extends to higher temperatures.

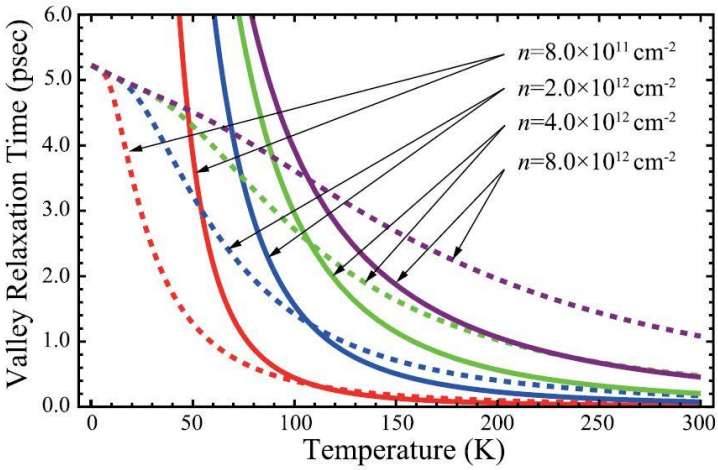

Figure 2.6: Carrier density dependence of the valley relaxation time for WS_2 as a function of temperature. The dashed lines indicate the relaxation time in the collisional broadening regime, while the solid lines indicate the thermal broadening regime. The red, blue, green, and purple curves represent the dependence at $n=8\cdot10^{11}$, $2\cdot10^{12}$, $8\cdot10^{12}$, and $8\cdot10^{12}$ cm^{-2}, respectively.[166]

The temperature-dependent exciton valley relaxation times under various exciton and carrier densities can be understood using a unified framework of intervalley exciton scattering. The intervalley exciton scattering in 1L-WSe_2 strongly dependent on the carrier density and exciton linewidth. The overall circular polarization degree P_C is determined by the following equation:[58,59,164,168,169]

$$P_C = \frac{P_0}{1 + 2\frac{\tau_r}{\tau_v}} \tag{2.2}$$

Where P_0 is the initial valley polarization generated in the system and τ_v^{-1} is the intervalley scattering rate. The effective exciton lifetime decay rate τ_r^{-1} includes both radiative (τ_R) and non-radiative (τ_{NR}) contributions. The term τ_r/τ_v indicates that the value of P_C largely depends on the competition between two processes: radiative recombination of valley polarized excitons (τ_r) and intervalley scattering (τ_v). Intervalley scattering (τ_v) can be significantly tuned by the screening effect induced by carrier doping.

Fig. 2.7(a) shows the temperature dependence of the exciton valley polarization in 1L-WSe_2 stacked on graphene and quartz. For the graphene sample, we observed much higher valley polarization compared with the quartz sample. The exciton linewidth, for a sample on top of

graphene, is narrow because of the reduced scattering on the graphene flake and the shorter τ_r. Shorter τ_r resulting from charge or energy transfer to the graphene. Exciton linewidths are much narrower than those on quartz, and the carrier density is higher than the sample on the quartz substrate. The predicted Fermi energy for sample on graphene is E_F = 19meV ($n_{C=}$ $3\cdot10^{12}$ cm^{-2}) and for sample on quartz is E_F= 13meV ($n_{C=}$ $2.1\cdot10^{12}$ cm^{-2}). The exciton valley polarization (P_C) becomes high when: the narrower linewidth, the larger E_F (carrier density), and the shorter τ_r will be the key to achieve a longer τ_v and a higher P_C.[167]

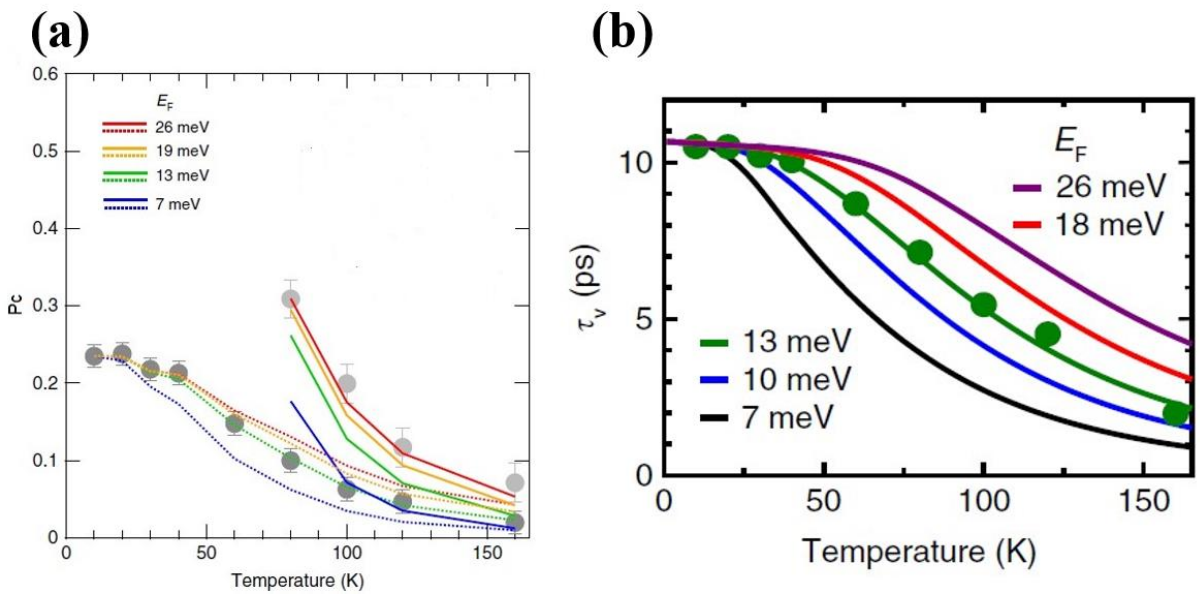

Figure 2.7 (a) P_C as a function of temperature for 1L-WSe_2 predicted for various E_F as functions of temperature. Solid and dotted curves are for on-graphene and on-quartz samples, respectively. The error bars correspond to the uncertainties of the polarization-resolved measurements. (b) The predicted temperature dependence of τ_v for various E_F (carrier density).[167]

The results provide a guideline for controlling the exciton valley relaxation times via Fermi energy tuning (carrier density tuning) and linewidth modulations via materials engineering and optical means.

Feng et al. [164] designed a strategy to enhance P_C at liquid nitrogen temperature. Doping dependent circularly polarized PL spectra of monolayer WS_2 at the temperature of 80K under off-resonance excitation (2.33 eV) are studied. The carrier density of the sample is controlled by electrostatic and optical doping. The evolution of neutral (A) and charged exciton (A^-)

emission states has been extracted. Surprisingly the electrostatic doping drives a continuous increase of P_C for charged exciton emission. Besides, by controlling photoexcitation strength, a considerable modulation of polarization degree is also depicted, parallel with the electrical doping effects. Helicity resolved PL spectra from p-type (−45 V) and n-type (+55 V) gated sample are shown in Fig. 2.8. When the WS_2 is negatively gated, the negatively charged exciton indicates a low polarization degree of 7%. While at a positive gate voltage and a higher induced carrier density, the sample exhibits a single A^- peak and a drastically higher polarization degree of 25%.

With regards to the optical doping dependent valley polarization, as shown in Fig. 2.8, the P_C value of A^- shows great distinction at 1.72μW and 1754μW excitation. Threefold enhancement of P_C from 7% to 22% achieved with increasing power. At both low and high powers, the carrier doping induced screening effect is prominent to influence valley polarization.

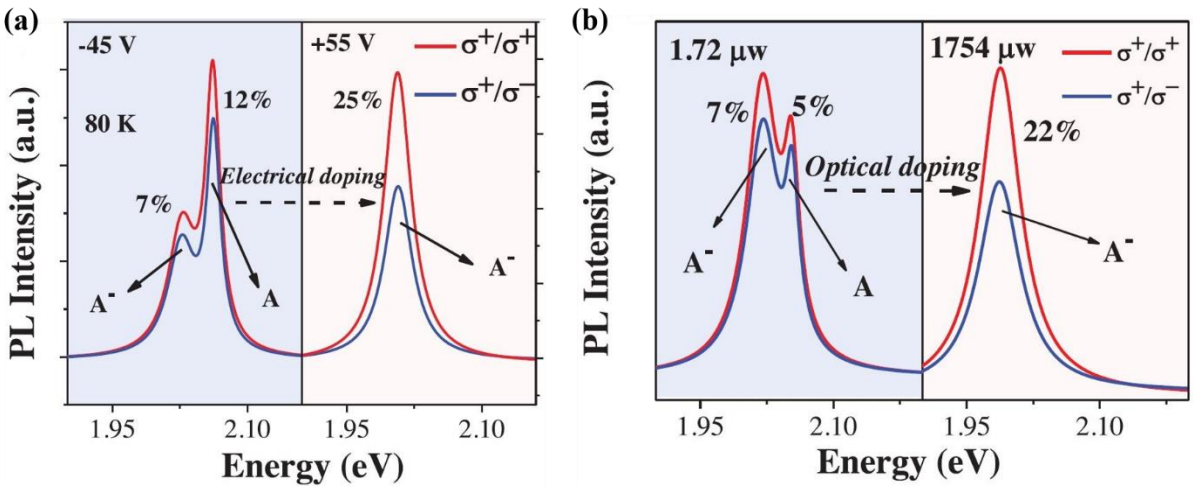

Figure 2.8 (a) Gate voltage-dependent circularly polarized PL measurement of monolayer WS_2 at 80 K. Polarization resolved PL spectra of gated WS_2, both with σ+ (σ−) detection. (b) Power dependent circularly polarized PL measurement of monolayer WS_2 at 80 K. Polarization resolved PL spectra of WS_2 pumped at different powers.

Hanbicki et al. [157] show that by applying a gate voltage, they can continuously tune the trion emission energy and vary the polarization from 20-40%. Interestingly, the polarization tracks the emission energy, with the polarization increasing with decreasing emission energy. This indicates the multi-particle nature of the trion has consequences on the details of the intervalley

scattering process. While the neutral exciton emission has zero polarization at room temperature, they observe a room temperature optical polarization over 40% for the trion. Using an applied gate voltage can modulate the electron density.

Chapter III
Experimental Methods

3.1 Optical spectroscopy setup

This chapter will mainly focus on the basic experimental setups used for the projects presented by this dissertation. Optical spectroscopy is used to characterize 1L-TMDs, to acquire information about the morphology and the quality of the flakes. This chapter covers the basic concepts of the characterization tools as well as the photochlorination doping process.

3.1.1 Micro- Photoluminesence (μ-PL) setup

Photoluminescence measurements provide information about excitonic behavior by using a specific wavelength that corresponds to the energy of the relevant exciton or similar feature of interest. In this thesis, PL measurements performed using an iHR-320 spectrometer (Horiba Scientific/Jobin Yvon Technology) via a backscattering geometry with two different excitation lasers (543nm and 594nm).

The selected continuum laser beam passes through a spatial filter, which creates a uniform Gaussian beam and expands the beam to achieve a diffraction-limited spot size. A neutral density filter follows and keeps the power lower than 1mW to prevent heating effects and minimize sample damage. The beam reaches a 50:50 beam splitter, which reflects and drives the light to the objective lens. The laser beam focused on the sample through a Mitutoyo 50x (NA:0.42, f=200mm) objective lens resulting in an approximately ~1μm spot size. The sample inserted in a helium flow cryostat (ST500, Jannis) and a XYZ mechanical stage (Thorlabs) controls the sample position.

Additionally, filters are put in place to stop laser light from entering the spectrometer. A 550nm and 600nm long pass and short pass filters (FESH0550/FELH0550 and FESH0600/FELH0600, Thorlabs) used for 543nm and 594nm laser lines, respectively.[170]

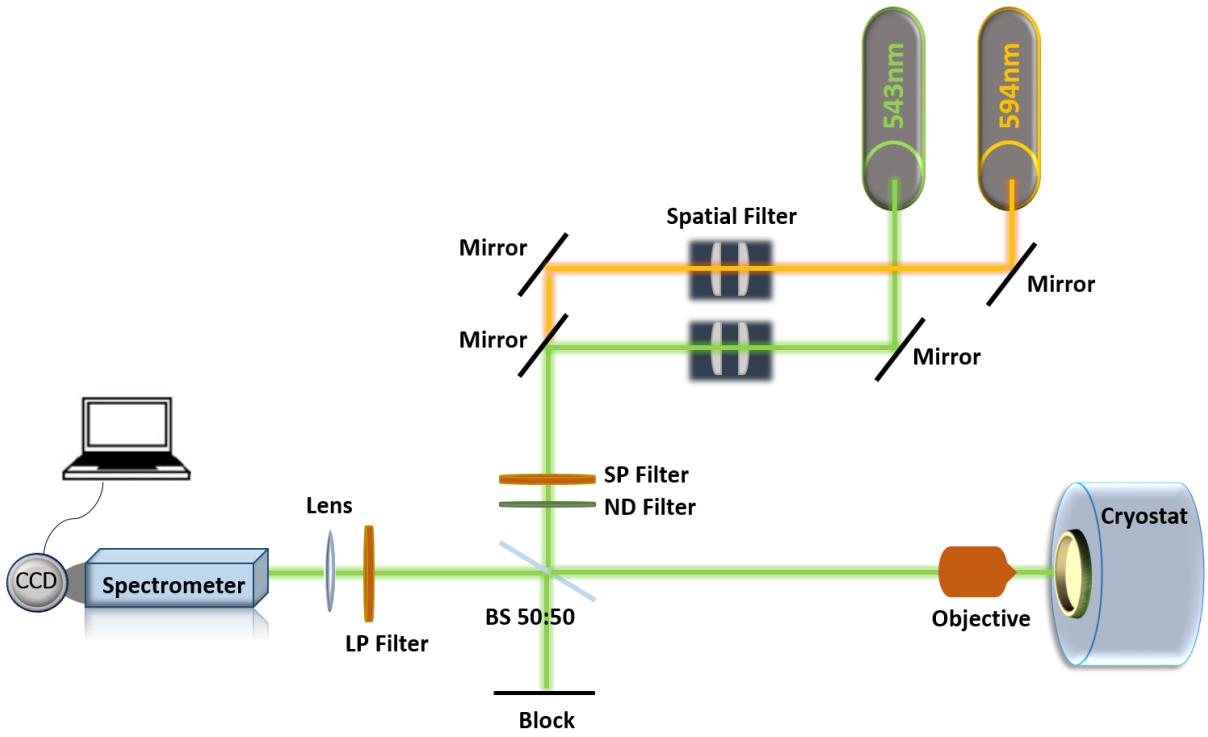

Figure 3.1 Schematic representation of the experimental setup used for micro-Photoluminescence (μ-PL) measurements. The setup was developed at the ULMNP lab of IESL/FORTH.

3.1.2 Micro-Differential Reflectivity setup

Differential reflectance is used to study the optical properties of 2D materials, especially transition metal dichalcogenides (TMDCs). This technique provides a powerful tool to characterize 2D materials in a broad range of the electromagnetic spectrum. Reflectance is a type of measurement that encodes information about sample reflectivity and absorption. This information is, furthermore, related to the dielectric function of the material. To use this setup, one must align the lamplight onto the sample and into the spectrometer. Reflectance measurement collected both of the selected ultrathin flake and the reference (usually the substrate). The substrate is subtracted from the sample and then the whole quantity is divided by the background-subtracted reference. The setup was developed to carry out differential reflectance measurements on 2D materials with ~3μm spot size in the wavelength range of 360nm to 2600nm (0.5eV to 3.4eV).

For the reflectance contrast measurements, we focused light from a supercontinuum tungsten-halogen source (SLS201L, Thorlabs) onto the samples using a Mitutoyo 50x (NA:0.42, f=200mm) objective lens (the same with μ-PL setup). The reflected light was collected by the objective and guided to a grating spectrometer equipped with a charge-coupled device detector. The optical path is similar to μ-PL configuration, but now the long and short pass filters are removed (Fig. 3.2). The reflectance contrast from the monolayer TMD flake was measured by the difference between the intensity from the monolayer (R_{ON}) and the bare substrate (R_{OFF}) and normalized to the intensity of the bare substrate.

$$\Delta R = \frac{R_{ON} - R_{OFF}}{R_{OFF}} \tag{3.1}$$

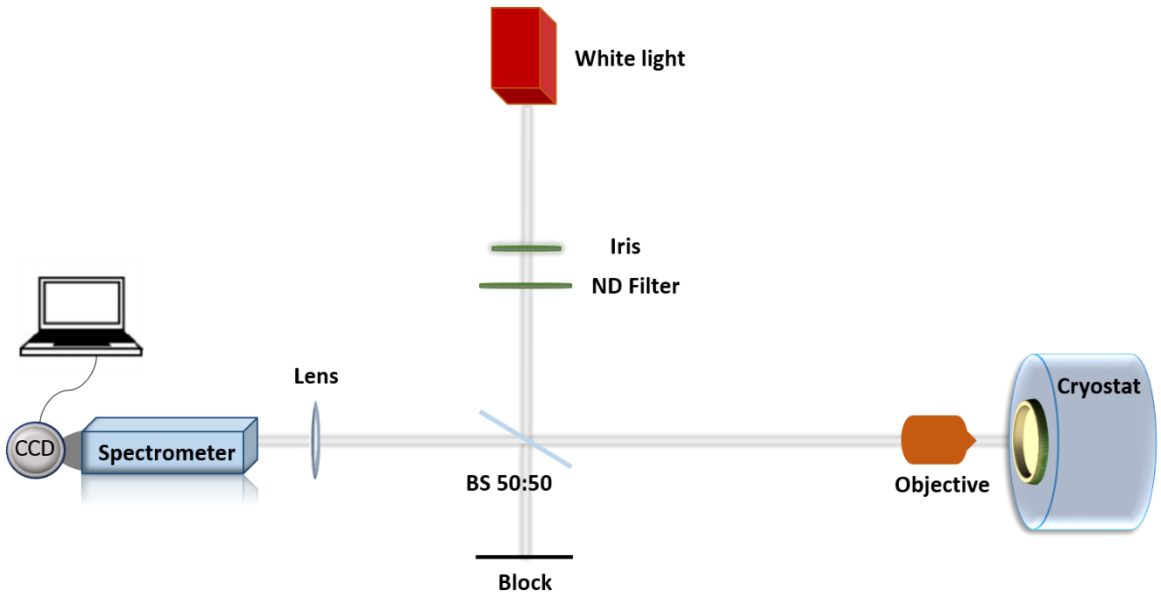

Figure 3.2 Schematic representation of the experimental setup used for micro-Reflectivity measurements. The setup was developed at the ULMNP lab of IESL/FORTH.

For a thin sample, the reflectance contrast spectrum is approximately proportional to the absorption of the flake.

3.1.3 Experimental setup for Valley Polarization measurements

We used the same micro-Reflectivity/PL setup (spatial resolution of 1μm) with a 50x objective, appropriate filters, and incorporated a continuous-flow He-cryostat (ST500, Jannis) to collect

PL in backscattering geometry. In this configuration, the beam splitter is flipped and the long pass filter placed at a critical angle. Samples were excited with continuous-wave lasers (543nm, 594nm) polarized as σ^+. An achromatic $\lambda/4$ waveplate changes the polarization of laser beams from linear to circular with positive (σ^+) helicity. Luminescence comes from the sample is analyzed as σ^+ and σ^- using a combination of a liquid crystal variable retarder (LCVR) and a linear polarizer placed before the spectrometer entrance slit. The emitted light is dispersed by the spectrometer equipped with a multichannel CCD detector. The total circular polarization is calculated by the following equation, $P_C = \frac{I_{\sigma^+} - I_{\sigma^-}}{I_{\sigma^+} + I_{\sigma^-}}$, where I_{σ^+}, I_{σ^-} are the emission intensities analyzed for positive/negative helicity, respectively. The emitted circular polarization is 0% when the sample is excited with linearly polarized light.

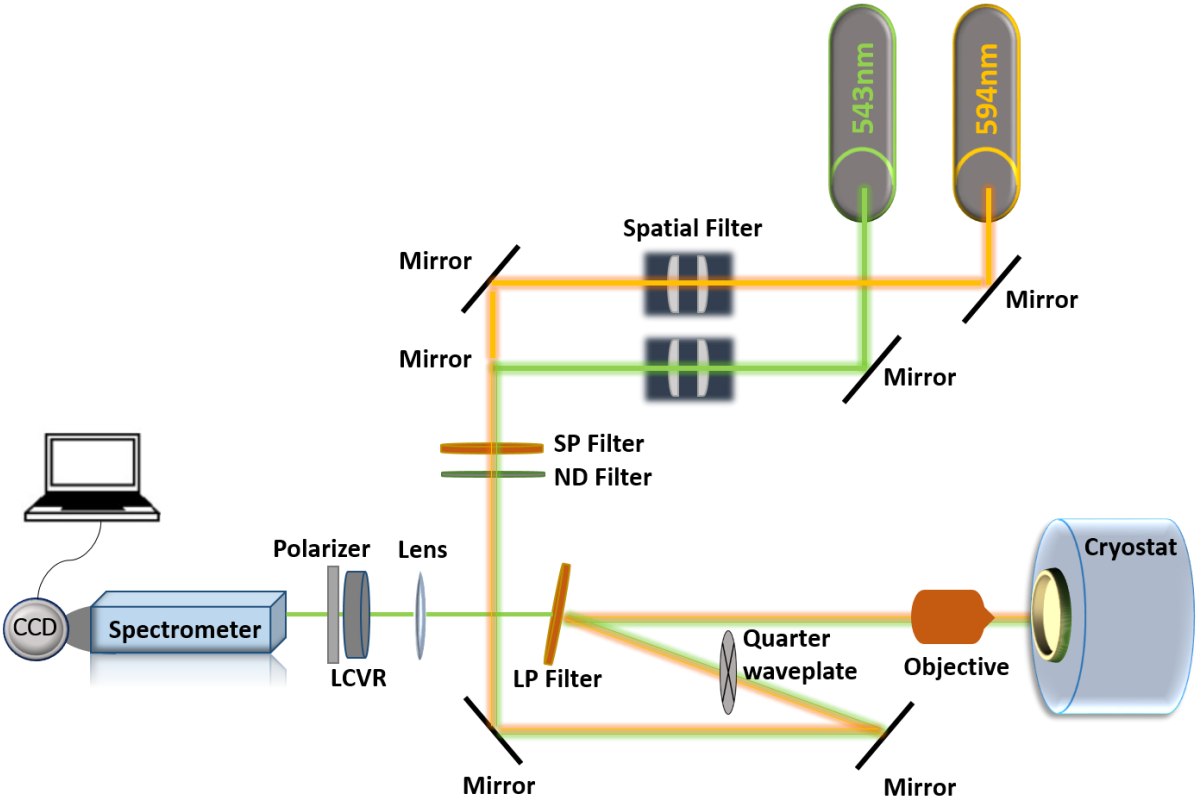

Figure 3.3 Schematic representation of the experimental setup used for spin-valley polarization measurements. The setup was developed at the ULMNP lab of IESL/FORTH.

3.1.4 Experimental setup for micro-Raman Spectroscopy measurements

The following experimental techniques that will describe is micro-Raman spectroscopy, which probes encoded information about a material's vibrational behavior. For example, in WS_2, the Raman spectrum is quite rich and slightly dependent on the incoming wavelength. A laser beam is aligned to interact with the specimen. The scattered photons are collected to measure the shifts in energy caused by inelastic scattering. Raman spectra were measured using a 473nm diode-pump solid-state laser as an excitation source. A 100x objective is used to focus the laser beam and to collect the Raman signal. The Thermo Scientific, Nicolet Almega XR Micro Raman analysis system utilized to measure Raman signals. Raman spectra were detected using 1200gr/mm gratings for high resolution. During measurements, the laser power used on the sample was 50μW to avoid possible heating effects by the laser and is controllable with the software. The experimental setup for measuring the Raman spectra shown in Fig. 3.4. A long pass filter with cut-on wavelength 473nm used to block short wavelength signals, and only the Stokes shift spectra could be measured. The filter cuts out the Rayleigh emission. The CCD sensor converts the incoming photons into an electrical signal. The result from the software is a spectrum with several counts assigned to each resolvable energy.

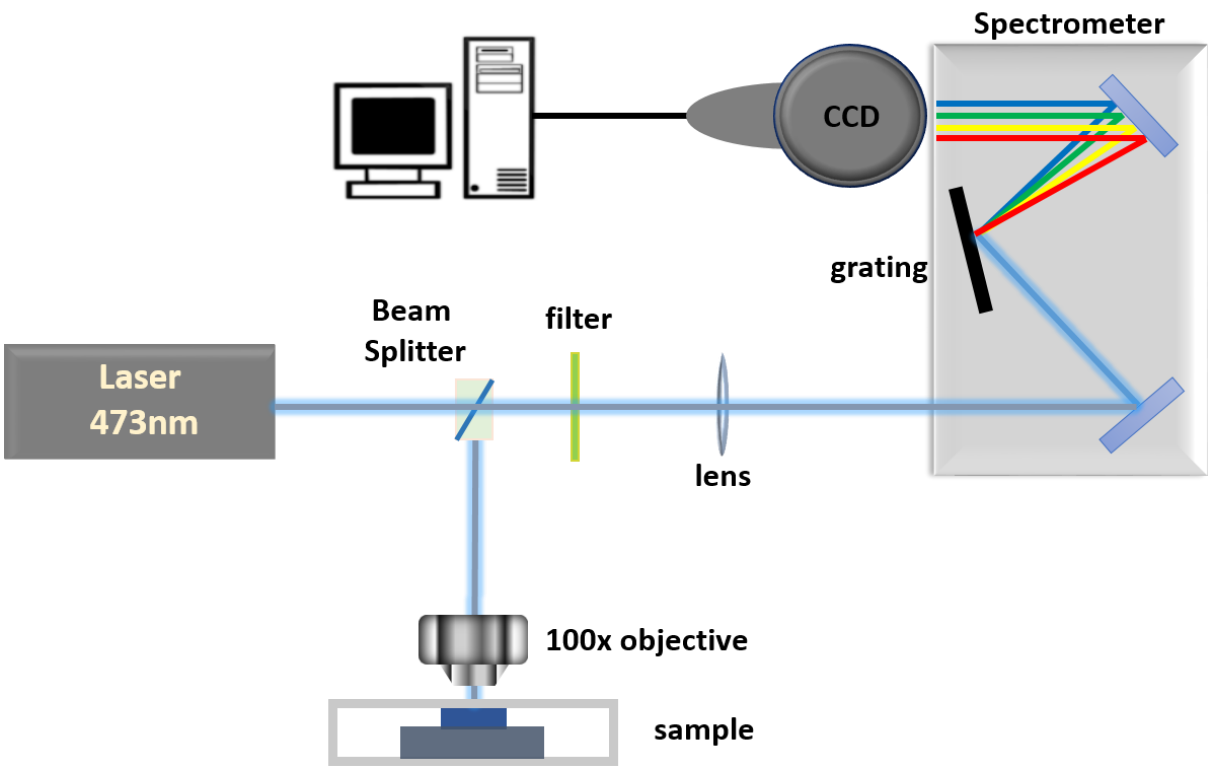

Figure 3.4 Schematic representation of the experimental setup used for the Raman measurements.

3.2 Cryogenic System

During the low-temperature experiments, the sample was kept in a continuous flow cryostat (ST500, Jannis) and cooled down by evaporating a cryogen (Liquid Helium (LHe), Liquid Nitrogen (LNi)). For this purpose, LHe or LNi is usually stored outside the cryostat in a mobile dewar and supplied through a transfer line. The transfer line (Janis flexible helium transfer line) connects the cryostat with the mobile dewar (Janis). The controlled transfer of LHe/LNi from a dewar into a heat exchanger adjacent to the sample holder used to vary the temperature in the range 4−475 K. The temperature of the sample is monitored with a two channel temperature controller (Lake Shore Cryotronics).

Vacuum systems are commonly used in low-temperature experiments to pump out the cryostat and transfer cube. The sufficient operation of a vacuum system is the thermal insulation of the vessel from the surrounding area. The cryostat is pumped down to 10^{-5} Torr or less, and a continuous helium/nitrogen flow is supplied by a pressurized dewar (250 mbar). In our lab, the vacuum system is a combination of a mechanical and a turbo pump. The Helium/Nitrogen flow can be monitored and regulated by a flow meter panel that has control valves in it. Continuous flow cryostat has to be supplied steadily with the liquid cryogen i.e. the cooling agent to maintain stable operating conditions. In this thesis, low-temperature experiments were carried out with a 100lt capacitance LHe dewar and 20lt capacitance LNi dewar.

3.3 Photochlorination process

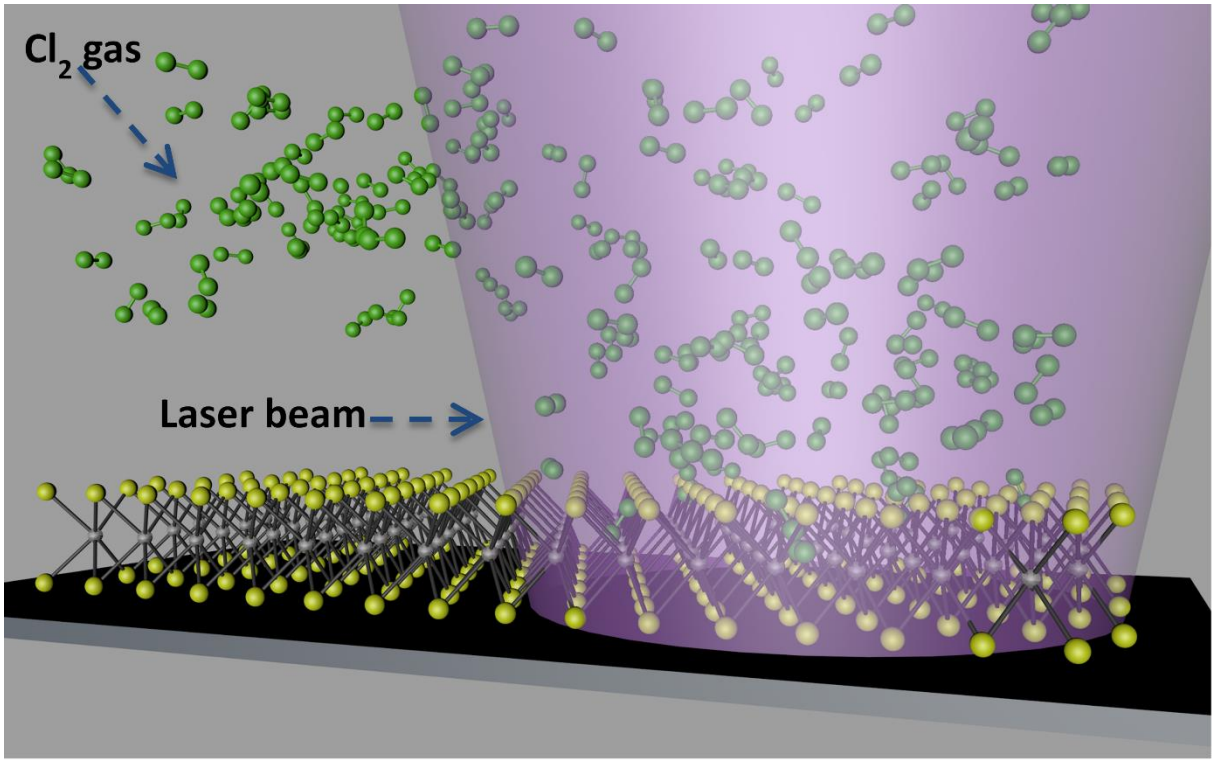

Scheme 1: Schematic representation of the process used for the photochlorination of TMDs

The as-prepared TMDs monolayers were subjected to irradiation by a KrF excimer UV laser beam emitting 20ns pulses of 248nm at 1Hz repetition rate that translated onto the monolayer area. For uniform exposure to laser radiation, a top-flat beam profile of 20×10 mm^2 was obtained using a beam homogenizer. The whole process took place in a vacuum chamber at 120Torr Cl_2 gas pressure maintained through a precision microvalve system. Different combinations of laser power (P) and the number of pulses (N_p) were tested to optimize the photochlorination process. In a typical experiment, the sample was irradiated at a constant power with N_p = 1, 5, 10, 20, 30, and 40 pulses, corresponding to different photoreaction times equal to 1, 5, 10, 20, 30, and 40 seconds. The photo-induced doping of TMDs was realized following irradiation in the presence of NH_3 gas, in the same configuration with chlorine. This simple, rapid, and scalable method is performed in the presence of ammonia (NH_3).

The safest way to irradiate the monolayers without damaging effects is to define all the radiation parameters. We conclude that the threshold fluence for a monolayer TMD (WS_2, MoS_2) is around ~$10\frac{\mathbf{mJ}}{\mathbf{cm^2}}$, after parametric experiments.

We can calculate the fluence by the following type:

$$\text{Fluence } \left({}^{\text{mJ}}/_{\text{cm}^2}\right) = \frac{\text{Energy (mJ)}}{\text{Beam Area (cm}^2)} \tag{3.2}$$

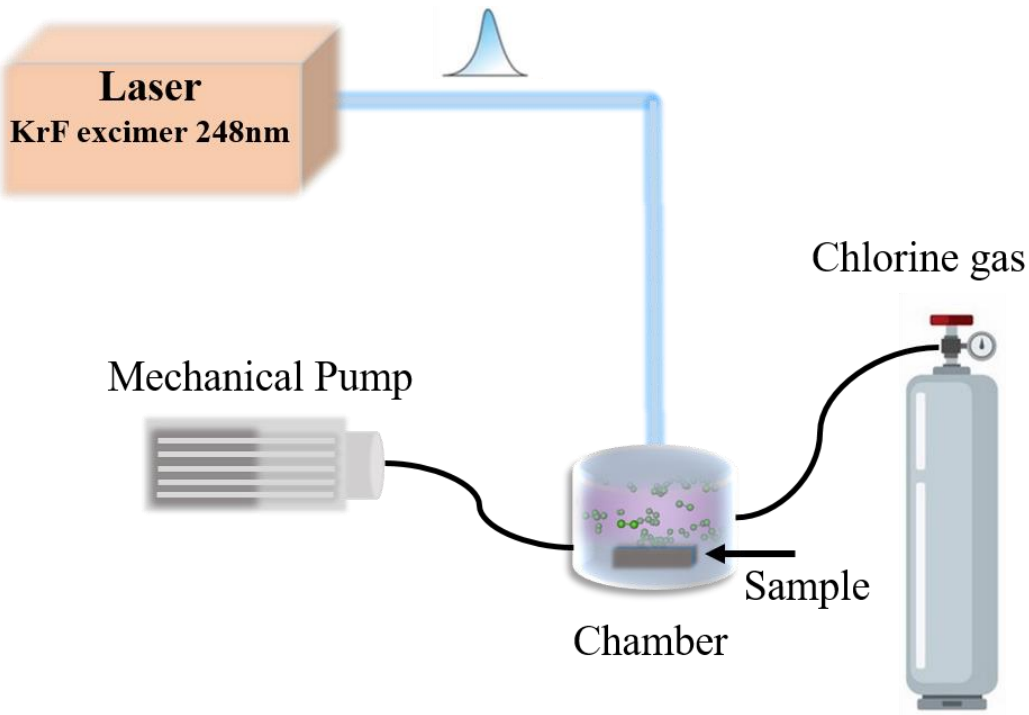

Figure 3.5 Experimental setup of the photochlorination process

3.4 Sample preparation

Commercial WS_2 crystal (2D Semiconductors, HQ Graphene) was mechanically exfoliated from a bulk crystal using an adhesive tape onto n-doped Si wafers covered by a 285 nm thick SiO_2 wafer. We also mechanically exfoliated high-quality hexagonal Boron Nitride, graphene, and graphite flakes.

In the present work, we fabricate and investigate the following different types of samples:

1) Monolayer WS_2 on Silicon dioxide (SiO_2) substrate (Chapter 4.1, 4.2, 4.3).

2) Monolayer WS_2 on a few layers of h-BN deposited on a highly doped 285nm thick SiO_2/Si wafer (Chapter 4.2, 4.3).

3) Monolayer WS_2 on single and few layers graphene deposited on a highly doped 285nm thick SiO_2/Si wafer. (Chapter 4.3)

4) Monolayer WS_2 on graphite flakes deposited on a highly doped 285nm thick SiO_2/Si wafer. (Chapter 4.3)

5) Monolayer WS_2 on Indium Tin Oxide (ITO). (Chapter 4.3)

6) Monolayer WS_2 on 50nm layer thick gold (Au) sputtered on a highly doped 285nm thick SiO_2/Si wafer. (Chapter 4.3)

Optical microscopy is used to locate the TMDs flakes on the samples and provide morphological information. A 100x objective lens was employed to capture high-resolution images. The monolayer and the substrate character of the samples were confirmed by micro-Raman spectroscopy at room temperature. Photoluminescence spectroscopy is another tool to recognize the monolayer flakes from 78K to room temperature.

Chapter IV
Experimental Results

4.1 Spatially Selective Reversible Charge Carrier Density Tuning in WS_2 Monolayers via Photochlorination

Chlorine-doped tungsten disulfide monolayer (1L-WS_2) with tunable charge carrier concentration has been realized by pulsed laser irradiation of the atomically thin lattice in a precursor gas atmosphere. This process gives rise to a systematic shift of the neutral exciton peak towards lower energies, indicating the reduction of the crystal's electron density. The capability to progressively tune the carrier density upon variation of the exposure time is demonstrated; this indicates that the Fermi level shift is directly correlated to the respective electron density modulation due to the chlorine species. Notably, this electron-withdrawing process enabled the determination of the trion binding energy of the intrinsic crystal, found to be as low as 20 meV, in accordance with theoretical predictions. At the same time, it is found that the effect can be reversed upon continuous-wave laser scanning of the monolayer in the air. Scanning Auger Microscopy and X-ray photoelectron spectroscopy are used to link the actual charge carrier doping to the different chlorine configurations in the monolayer lattice. The spectroscopic analyses, complemented by density functional theory calculations, reveal that chlorine physisorption is responsible for the carrier density modulation induced by the pulsed laser photochemical reaction process. Such bidirectional control of the Fermi level, coupled with the capability offered by lasers to process at pre-selected locations, can be advantageously used for spatially resolved doping modulation in 1L-WS_2 with micrometric resolution. This method can also be extended for the controllable doping of other TMD monolayers.

4.1.1 Introduction

Carrier modulation is an important parameter in the study of the electronic properties of semiconductors and at the heart of many applications in microelectronics. Tuning the charge carrier density, i.e. doping, can be realized chemically, via bonding of foreign atoms to the crystal structure,[99,171,172] or electrostatically, by inducing a charge accumulation.[47,86,173] Electrical doping measurements of 1L $MoSe_2$[50] and WSe_2[53] have shown the tunability in the photoluminescence (PL) emission of the neutral (X) and negatively (X^-) or positively (X^+) charged excitons (so-called trions). Moreover, electrically tunable PL emission between X^- and X components observed in MoS_2 and WS_2.[47,52] At the same time, chemical doping via the absorption of atoms in the gas phase and organic molecules demonstrated to be a promising approach to tune the carrier density in TMDs. [86,90,82,83,174,175] Despite the numerous studies on TMDs' doping reported to date, the fine control in charge carrier tunability, as well as the doping reversibility, remain unresolved issues.

In this thesis, we demonstrate the reversible tunability of the position of the neutral exciton emission peak of 1L-WS_2 via photoinduced chlorination of the atomically thin lattice. It is found that this is a consequence of the adsorption of electron-withdrawing chlorine adatoms that strongly suppresses the electron concentration and enhances the PL efficiency. Theoretical calculations indicate that the charge transfer between the dopant species and the monolayer induces a shift in the Fermi level, giving rise to the observed modulation of the optical properties. Notably, it is found that the lattice can be driven back to its pristine state upon continuous wave (CW) laser-induced removal of chlorine dopants. It is concluded that photo-assisted chemical doping provides a useful and fast tool for bidirectional control of the Fermi level in 1L-WS_2. More importantly, it enables, on-demand, spatially resolved doping modulation, upon laser-induced adsorption/desorption in preselected locations, in a write-erase manner. More information about the photochlorination process is included in Chapter 3.3.

4.1.2 Results and discussion

WS_2 samples were mechanically exfoliated from a bulk crystal (2D semiconductors) using an adhesive tape and placed onto 290 nm-thick SiO_2/Si substrates. Monolayer regions were identified via optical microscopy and confirmed with micro-Raman spectroscopy (Fig. 4.1) with low laser power to avoid structural damage. The energy difference between the two main Raman vibrational modes, E′ (in-plane mode) and A_1' (out-of-plane mode), is used extensively in the literature as the fingerprint of the number of layers.[66]

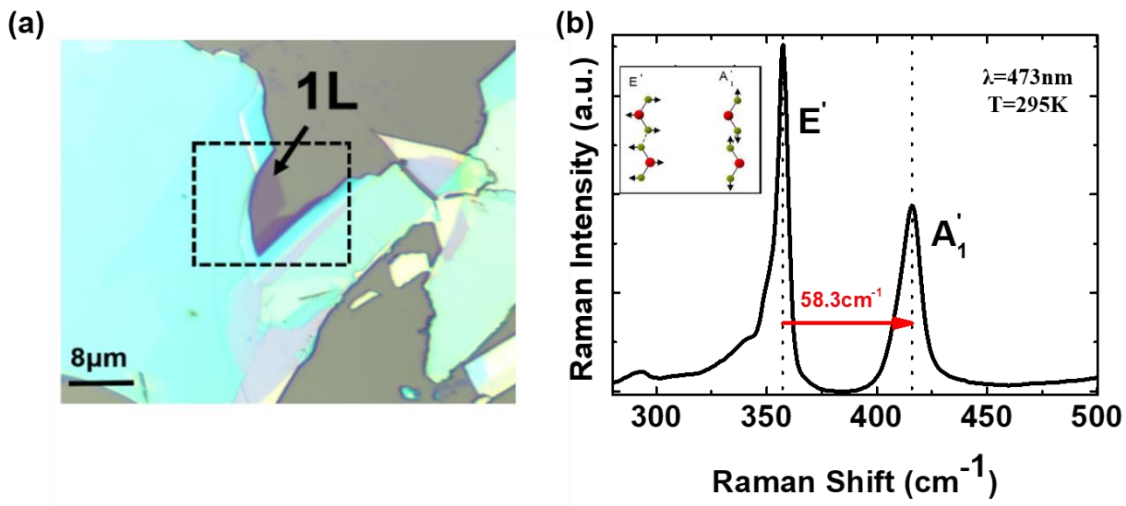

Figure 4.1 (a) Optical microscopy image of exfoliated WS_2 flakes. The light purple area indicates the monolayer region with a size of 5-8μm across. (b) Room temperature Raman spectra collected with 473nm laser excitation for monolayer WS_2.

Following exfoliation, the WS_2 monolayers were exposed to the irradiation of a 248nm UV laser source emitting 20ns pulses (Scheme 1) at a repetition rate of 1Hz, as we discussed in Chapter 3.3.

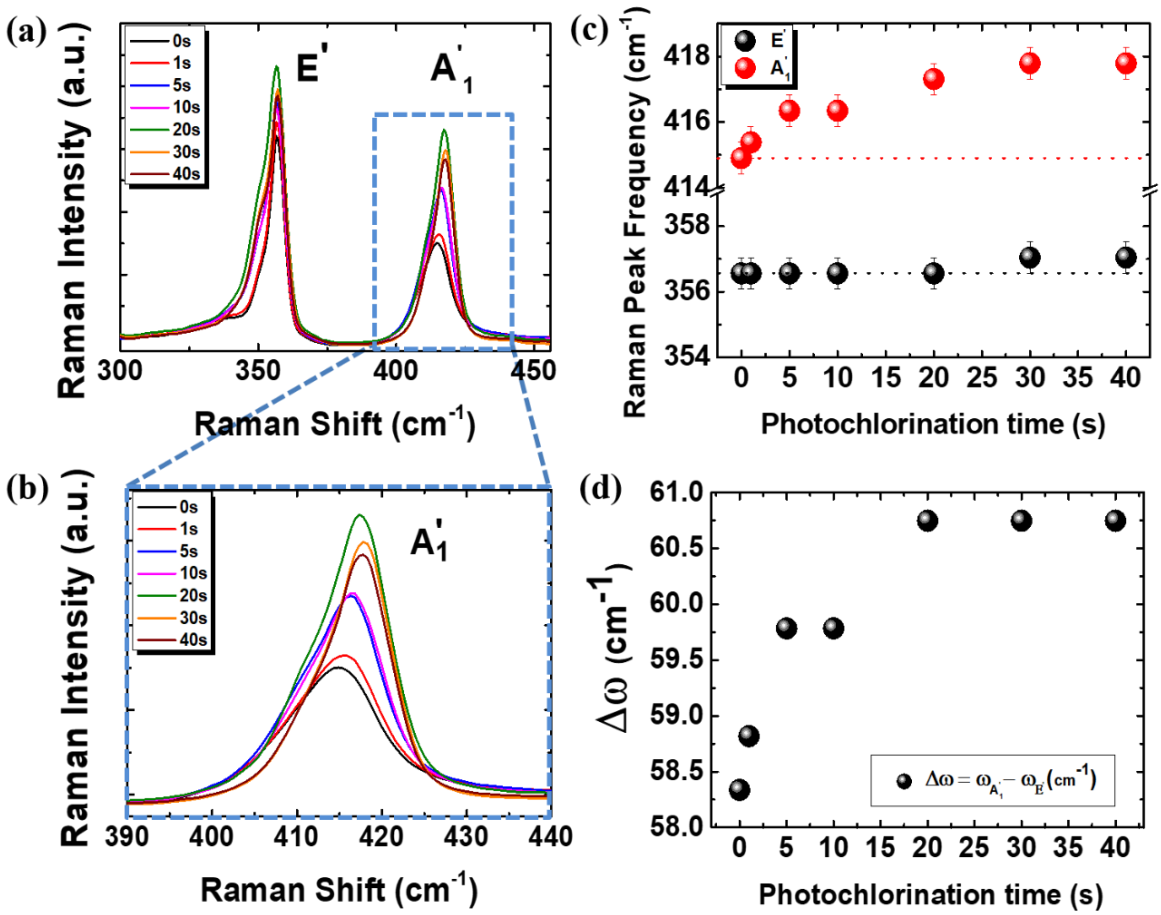

Figure 4.2 (a) Evolution of the Raman Spectra of WS_2 monolayer with the photochlorination time shown in the inset; (b) Evolution of the out-of-plane vibrational mode A_1'; (c) Dependence of the E' and the A_1' peak frequencies on the photochlorination time; (d) Frequency separation between the E' and the A_1' modes as a function of the photochlorination time.

Fig. 4.2 (a) presents the evolution of the micro-Raman spectrum of a 1L-WS_2, subjected to UV irradiation in Cl_2 environment, upon increasing the exposure time. The corresponding dependence of the E' and A_1' peak frequencies with doping steps shown in Fig. 4.2 (b). It is found that the A_1'mode progressively blue-shifts upon irradiation for 40s in Cl_2, while the peak position of the E' mode remains unaffected. It is well reported that, in a typical 1L-TMD, the out-of-plane mode, A_1' is sensitive to charging effects due to the strong electron-phonon coupling.[95,133] In particular, the observed blue shift of the A_1' peak complies with electron-withdrawing, i.e. p-type doping. On the contrary, it is demonstrated that the in-plane, E', mode is not significantly influenced by electron doping. [90,95,133] Fig. 4.2 (d) shows the corresponding increase of the Raman frequency difference ($\Delta\omega = \omega(A_1')$-$\omega$(E')) with the doping time, which

remains within the reported limit of the monolayer energy difference of 59-61 cm^{-1}.[62,176] All the above observations indicate a hole-doping effect induced upon such photochlorination treatment.

Micro-PL spectroscopy and reflectivity measurements were used to further explore the hole doping effect induced by photochlorination. Fig. 4.3 (a) shows the PL spectra of monolayer WS_2 at 78K at different photochlorination times. For the analysis of the different emission peaks, we fit the spectra with Gaussian functions acquiring high values of coefficient of determination ($R^2 > 0.99$). The corresponding PL spectra were deconvoluted into three peaks (Fig. 4.3 (b)), which are assigned (from higher to lower energy) to neutral exciton (X) at 2.085eV, negatively charged exciton (trion, X^-) at 2.045eV, which arise from direct optical transitions at the K point and emission from biexcitons and localized states (XX/L). [55,176,177] Notably, the X^- and X emissions behave differently as a function of the photochlorination time. A first finding is that the X emission intensity is remarkably enhanced at the expense of the X^- which can be explained as follows: WS_2 is a well-known n-type 2D material and its PL spectrum is accompanied by negatively charged trions even at room temperature.[55] Under the photochlorination treatment, the electron concentration is reduced, suppressing the oscillator strength of the negatively charged trions and leading the PL spectral weight towards the neutral exciton emission. More importantly, the X peak progressively redshifts with photochlorination time and tends to saturate at elevated exposure times (Fig. 4.3 (c)); On the other hand, the X^- peak weakly blueshifts (Fig. 4.3 (c)). As a result, the trion binding energy, corresponding to the energy difference between the X and X^-, decreases with the photochlorination time (Fig. 4.3 (d)), in agreement to previous reports on electron doping in 1L-WS_2, 1L-MoS_2, and 1L-WSe_2.[47,90] Such reduction in the trion binding energy can be attributed to the Fermi level lowering upon photochemical doping with chlorine.

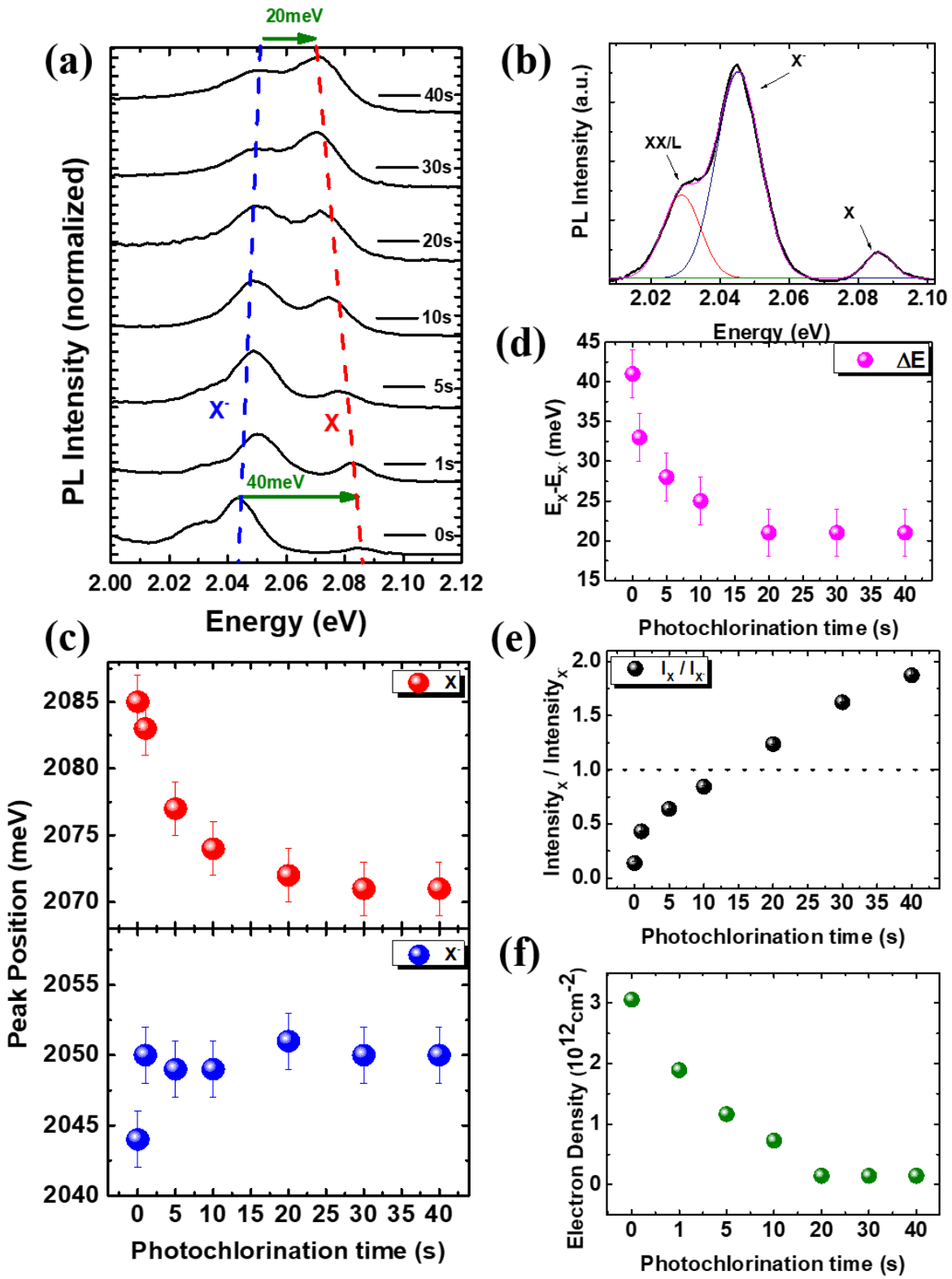

Figure 4.3 (a) Evolution of the PL spectra of a 1L-WS_2 at 78K, with the photochlorination time. (b) Deconvolution of the initial PL spectrum obtained before the photochlorination process; the neutral exciton (X), negatively charged exciton (trion, X^-), and emission from localized states (XX/L) peaks are assigned. (c) The peak position of X and X^- as a function of the photochlorination time. (d) Dependence of the trion binding energy, corresponding to the energy difference between the X and X^- peaks, on the photochlorination time. (e) The ratio of normalized intensities of the X and X^- peaks as a function of the photochlorination time. (f) Evolution of the calculated electron density with the photochlorination time.

Interestingly, the trion binding energy saturates to the quite low value of ~20meV, which is in agreement with theoretical predictions for the 1L-WS_2 intrinsic (undoped) crystal.[178] The observations will be further discussed in the DFT calculations section below. Fig. 4.3 (e) shows the ratio of normalized intensities of two excitonic components as a function of the doping steps. The as-exfoliated 1L-WS_2 is of n-type and thus rich in electrons, which enhances the probability of X^- formation; as a result, the spectral weight of the X^- peak is initially predominant. The progressive suppression of the X^- peak, coupled with the monotonical enhancement of the X peak observed upon photochlorination can be interpreted as a reduction of the 1L-WS_2 electron density, which can be also attributed to the Fermi level lowering. The corresponding splitting between the exciton (ω_x) and trion energy (ω_x^-) is predicted to be linearly dependent on the Fermi energy [179] and obey the equation: $\hbar\omega_x - \hbar\omega_x^- = E_{bX^-} + E_F$. Based on this equation, the electron density n_e can be calculated, assuming the measured E_{bX^-} of 20meV and the effective mass of electrons as m_e=0.35m_0 [47] where m_0 is the free electron mass. The calculated electron density n_e as a function of the photochlorination time shown in Fig. 4.3 (f); the electron densities of 1L-WS_2 before and after doping in the saturation region are ~3.05 × 10^{12} and ~0.14 × 10^{12} cm^{-2}, respectively, while their difference is Δn_e ~ 2.91 × 10^{12} cm^{-2}. The capability to progressively tune the carrier density upon variation of the photochlorination time, shown in Fig. 4.3 (e), implicates that the Fermi level shift can be directly correlated to the respective electron density modulation due to the chlorine species.

The estimate of the electron density in monolayer WS_2

We have analyzed the Photoluminescence spectra to determine the energies to create both neutral excitons (X) and trions (X^-) as a function of the doping level. The analysis is based on the Fermi energy ($E_F = \frac{\hbar^2 \pi n}{m^*}$) using an electron band mass of m_e = 0.35m_0 [50,83] where m_0 is the electron mass. When the Fermi energy varied from 1 to 21 meV, the exciton energy red-shifts, whereas the trion energy remains largely unchanged, after a slight initial blueshift (Fig. 4.3 (c)).

The splitting between the exciton and trion energy predicted to be linearly dependent on the Fermi energy and obey

$$\hbar\omega_X - \hbar\omega_{X^-} = E_{bX^-} + E_F \quad (4.1)$$

where E_{bX^-} is the trion binding energy. Because the exciton can be considered as an ionized trion, $\hbar\omega_X - \hbar\omega_{X^-}$ defines the minimum energy for the removal of one electron from the trion. In the limit of infinitesimal doping, the trion binding energy E_{bX^-} is the energy required to promote one of the electrons in a trion to the conduction band edge.[179] We also determine the trion binding energy to be 20meV. The result indicates that sufficient charge neutralization ($\Delta n_e = (3.05 - 0.14)\cdot 10^{12}$ cm^{-2} = $2.91\cdot 10^{12}$ cm^{-2}) has been achieved in 1L-WS_2 via photochlorination process (Fig. 4.3 (f)).

Temperature-dependence measurements have been performed in another exfoliated WS_2-monolayer that has gone through the photochlorination process for t=15s and below we plot the data for 2 different powers, 120μW (Fig. 4.4 (a)) and 550μW (Fig. 4.4 (b)).

At 78K, the PL spectra are dominated by the emission from neutral and charged excitons for both powers. As we increase the temperature, it is clear the dissociation of the charged to neutral exciton. At room temperature measurements, the neutral exciton dominates the PL spectra as it is expected since the binding energy of the trion is 20meV (Fig. 4.3(d)).

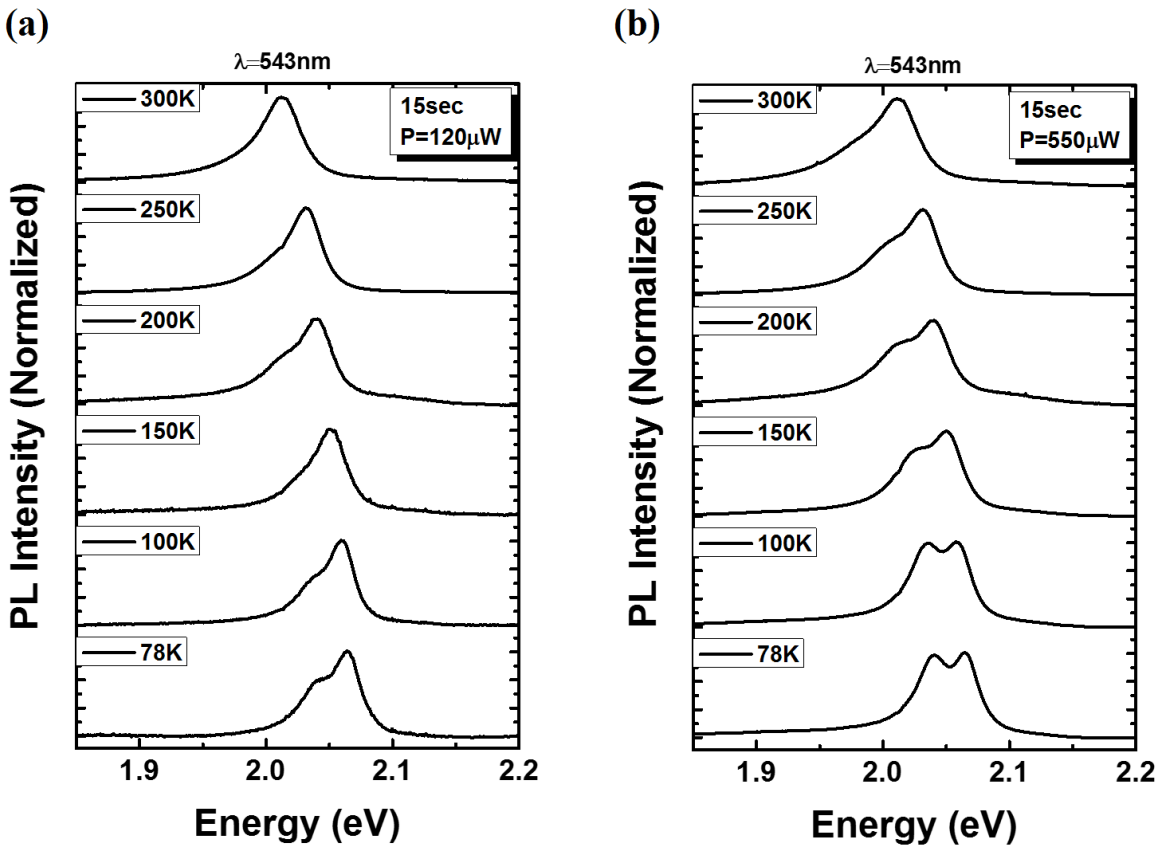

Figure 4.4 Temperature dependence measurements for a photochlorinated 1L-WS_2 at two different laser powers (a) 120μW and (b) 550μW.

The excitation power dependence of the PL intensity provides insights into the physical origin of the corresponding PL peaks. Since the behavior is the same for all plots in Fig.4.4, the following Fig. 4.5 present the data for the photochlorinated monolayer at 15s. The PL spectrum is dominated by the neutral and charged excitons and XX/L emission is suppressed after UV irradiation.

In Fig. 4.5, left panel (a), we show power dependence data at T=78K taken with 543nm excitation wavelength. A typical behavior is observed where for low power densities the neutral exciton dominates the spectrum and as we increase the power, the intensity of the charged exciton increases due mainly to photodoping. The way to reveal the nature of the two emission channels is to plot the integrated intensity for both peaks as a function of the excitation power density in a log-log plot (Fig. 4.5(b)). A linear dependence with power law exponent of 1 is evident for both peaks verifying the excitonic nature of these emission channels.

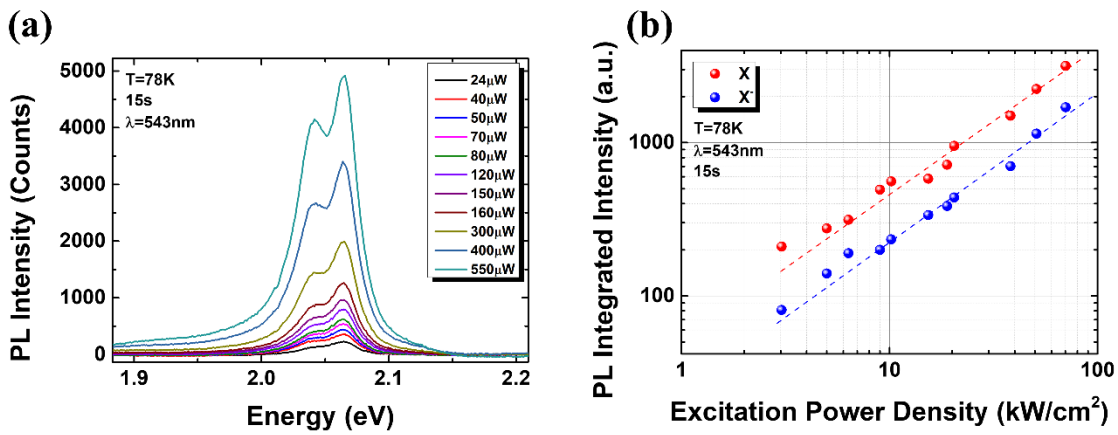

Figure 4.5 (a) Power dependence measurements for a photochlorinated 1L-WS_2 at 78K with laser excitation λ=543nm. (b) The integrated intensity for both peaks as a function of the excitation power density.

Differential reflectivity measurements performed in the same 1L-WS_2 are in remarkable agreement with the micro-PL results described above. The respective spectra show the two distinct excitonic absorption peaks, X^- and X, at ~2.04eV and ~2.086eV, respectively.[177] Moreover, the X^- absorption, in differential spectra, was suppressed by doping, while the trion binding energy saturates to the same value of ~20 meV (Fig. 4.6 (a), (b)), following the results obtained by the micro-PL spectra.

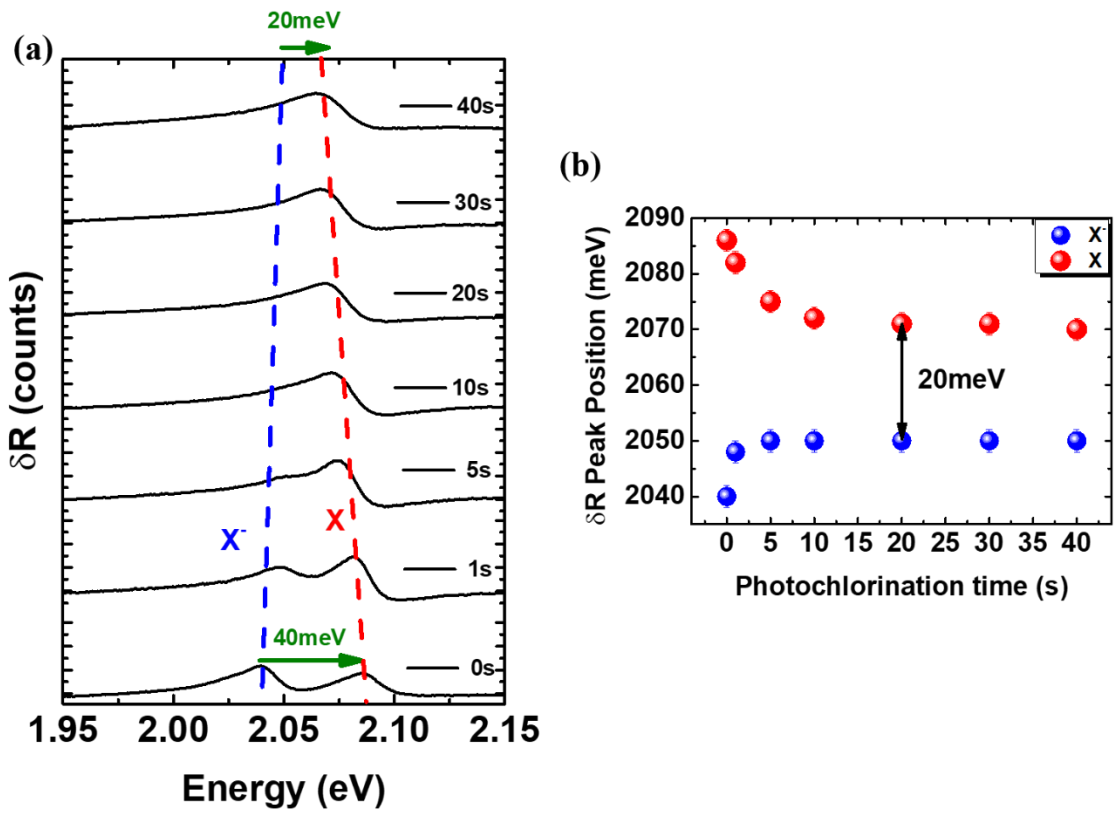

Figure 4.6 (a) Differential reflectance spectra of the same 1L-WS_2 obtained at each doping step. Differential reflectivity measurements are in agreement with the micro-PL results described above. (b) The peak position of the neutral (X) and the negatively charged exciton (trion, X^-), as the doping step increases.

To shed light on the photoinduced reaction process between 1L-WS_2 and Cl_2, topographic X-Ray Photoelectron Spectroscopy (XPS) and Scanning Auger Microscopy (SAM) were used to determine the chemical state of the W, S, and Cl. In a first step, the XPS spectra of single WS_2 layers before and after the photochlorination treatment were compared, as presented in Fig. 4.7(a). Notably, in the spectrum of the photochlorinated sample, a characteristic Cl peak was detected, in addition to the photoelectron lines of W, S, adventitious C and Si (due to the substrate) observed in the pristine sample. The corresponding [S]/[W] ratio, however, remained close to 2 showing that there is no significant replacement of S with Cl. On the other hand, SAM detected no Cl on the surface of the laser-treated sample, suggesting that Cl is loosely bonded on WS_2 and that desorption of chlorine species from WS_2, due to the heating of the surface by the high energy/high flux electron beam, takes place. More detailed information on the chemical bonding can be deduced from analyzing the XPS core-level spectra of the constituent elements. Fig. 4.7(b) and 4.7(c) show the S-2p and the W-4f core level spectra, respectively, for the two samples (pristine and Cl-doped). In both lines, the split due to spin-orbit coupling is observed, so the core level spectra consist of doublets (S-$2p^{1/2}$ and S-$2p^{3/2}$ as well as W-$4f^{5/2}$ and W-$4f^{7/2}$).

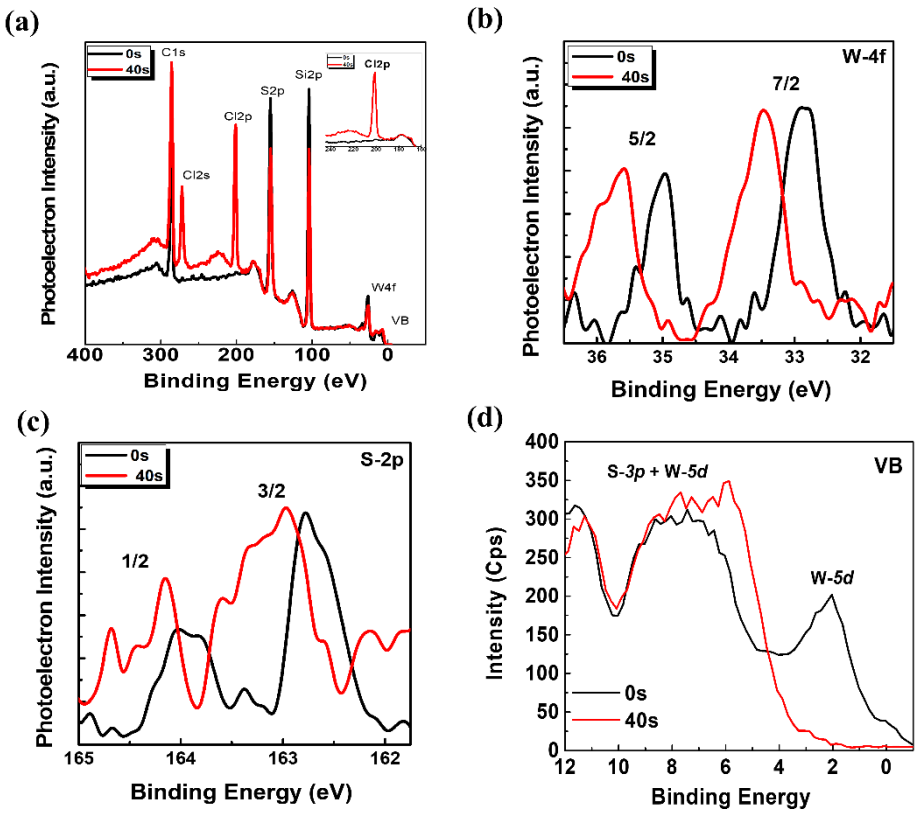

Figure 4.7 (a) XPS wide scan spectra of the pristine (black curve) and photochlorinated for 40s (red curve) 1L-WS_2. The legends indicate the assignment of the corresponding photoelectron peaks; Corresponding W-4f (b) and S-2p (c) core level spectra, showing splitting due to spin-orbit coupling; (d) Corresponding valence band spectra of the 1L-WS_2 samples.

In the case of W-4f core-level spectra, the binding energy of the W-4f$^{7/2}$ is observed to be that of pure WS_2,[180] thus proving the quality of this reference sample. In the case of the sample exposed to Cl, the dominant W-4f$^{7/2}$ peak is located at higher binding energy, indicating a charge transfer due to Cl incorporation, which is also observed for W-Cl bonds in WCl_4. Further insight is provided by analyzing the S-2p$^{3/2}$ core-level spectra (Fig. 4.7(d)). Indeed the S-2p$^{3/2}$ peak for the pristine WS_2 is detected at the expected binding energy for pure WS_2. In the case of the Cl-doped sample, there is both a shift of the S-2p doublet from the 162.8eV for pure WS_2 and a fine structure of the S-2p$^{3/2}$ peak with contributions at 163.1 and 163.5eV. The former can be attributed to S-containing aromatic compounds, such as thiophenol which might be formed on the surface of the samples by the reaction of the adventitious carbon with S in the presence of Cl upon laser irradiation; the latter might be attributed to either S-containing aliphatic compounds, formed on the surface of the samples by reaction of the adventitious

carbon with S in the presence of Cl upon laser irradiation, or to S-Cl bonds similar to those observed in disulfur dichloride (S_2Cl_2).[181] All of the aforementioned compounds (e.g. thiophenol, and S_2Cl_2) decompose or desorb upon annealing at mild temperatures (e.g. 137 ^oC for S_2Cl_2), while even W chlorides decompose and desorb upon electron irradiation [182]; this explains the lack of detection of Cl in SAM experiments due to the heating of the sample's surface by the incoming electron beam. As a conclusion, Cl seems to develop Cl-S bonds mostly with the S atomic layer, which result in charge transfer from W, as well, due to the high electronegativity of Cl. Finally, the valence band spectrum (Fig. 4.7(d)) of pristine 1L-WS_2 is characterized by two distinct bands at 7 and 2eV below the Fermi level assigned to hybridized S3p-W5d states, and pure W5d states, respectively; the latter band is depleted upon photochlorination resulting in the substantial suppression of the X^- PL peak (Fig. 4.3(e)).

To gain a deeper understanding of the chemical bonding attained due to photochlorination reactions, spin-polarized Density Functional Theory (DFT) calculations, were carried out, using the Vienna Ab-initio Simulation Package (VASP)[183,184] with projector augmented wave (PAW) pseudopotentials[185] and the Perdew–Burke–Ernzerhof (PBE) exchange-correlation functional.[186] The 1L-WS_2 with Cl is modeled using a 6x6 supercell. Two different scenarios for the interaction of chlorine with 1L-WS_2 have been investigated, namely chlorine atoms are filling S vacancies or become adsorbed on a basal plane. The DFT calculation revealed that in the former bonding configuration, chlorine creates a donor level (due to the more electron of Cl compared with S) in 1L-WS_2 (Fig. 4.8(a)), giving rise to a Fermi level shift towards the conduction band and therefore cannot account for the observed redshift of the neutral exciton peak. On the contrary, chlorine adsorption creates an acceptor level (due to the unpaired electron of Cl), which shifts down the Fermi level of n-type WS_2 (Fig. 4.8(b)) and therefore complies with the neutral exciton peak redshift. The chlorine desorption effect revealed by the DFT calculations complies with the XPS findings discussed above.

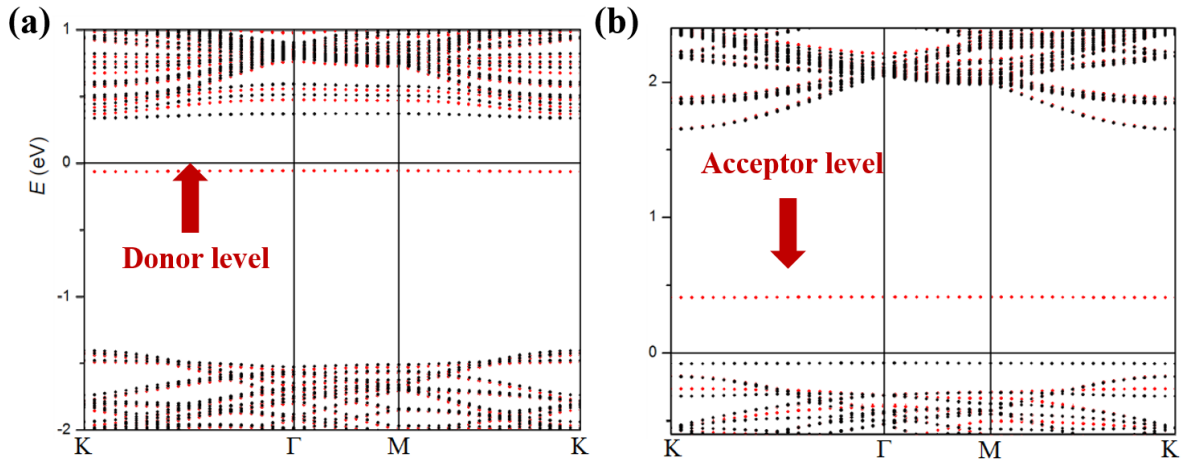

Figure 4.8 Electronic band structures of 1L-WS_2: (a) with Chlorine atoms filling S vacancies; (b) with Chlorine atoms adsorbed on the basal plane.

We find that the observed photochlorination effect can be reversed upon CW laser (473nm) rastering of the chlorine-doped 1L-WS_2, possibly due to the laser-induced desorption of chlorine atoms from the monolayer. In particular, following such a dechlorination process, the Raman A_1' mode position, the PL intensity, as well as the trion binding energy, return practically back to the levels before photochlorination (Fig. 4.9, 4.10, 4.11). The respective micro-PL and differential reflectance spectra are presented in Fig. 4.9 (a) and (b). As shown in this Figure, both the PL and reflectivity spectra evolve upon increasing the CW laser power from 316kW/cm^2 to 356kW/cm^2, but become stable upon further increasing the CW power. It is also found that the degree of dechlorination can be also controlled with the variation of the rastering time. Based on the above observations, we can postulate that the photochlorination approach, demonstrated here, provides a useful tool for bidirectional (extraction or injection of electrons) control of the electron density levels in 1L-WS_2.

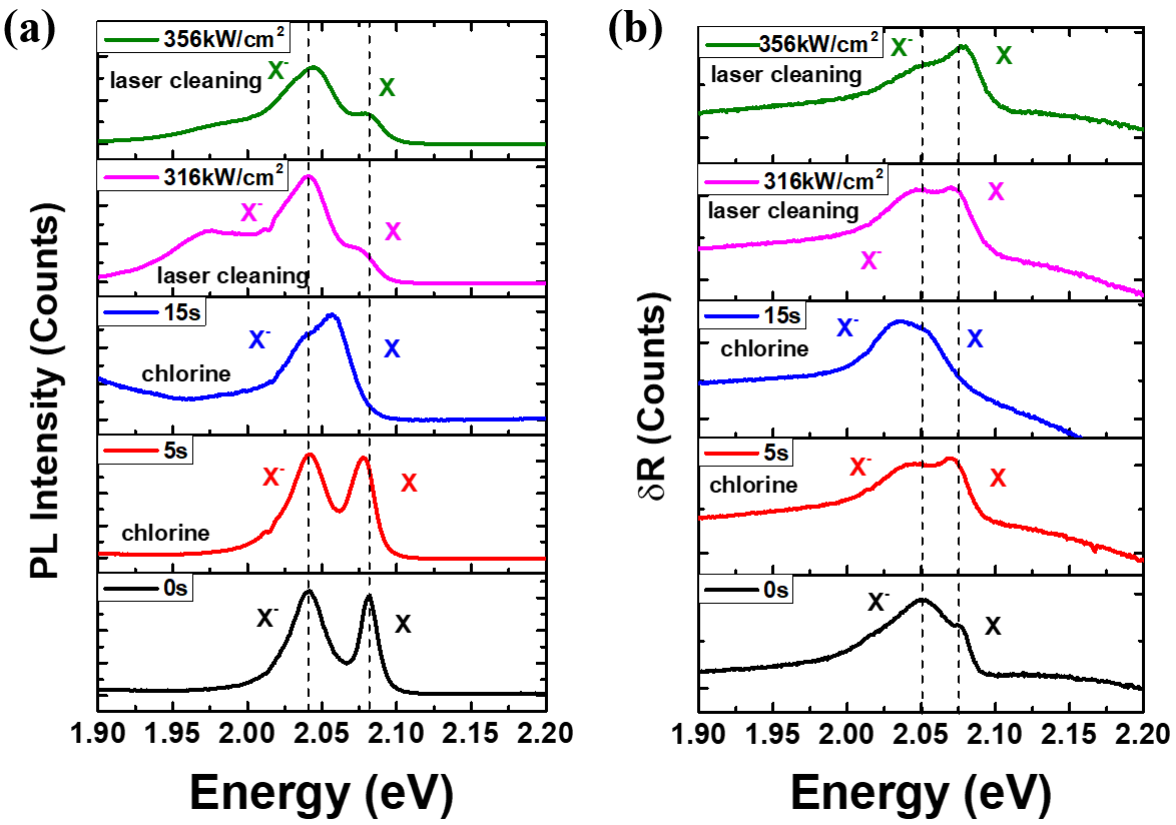

Figure 4.9 PL (a) and differential reflectance (b) spectra of a pristine 1L-WS_2 (black curves) and photochlorinated for 5s (red curves) and 15s (blue curves) respectively, at 78K. The corresponding spectra obtained after CW laser rastering of the monolayer area using 316 kW/cm^2 (magenta curves) and 356 kW/cm^2 (green curves) are also presented. The resonant energies of the X and X^- excitons are indicated with dotted lines.

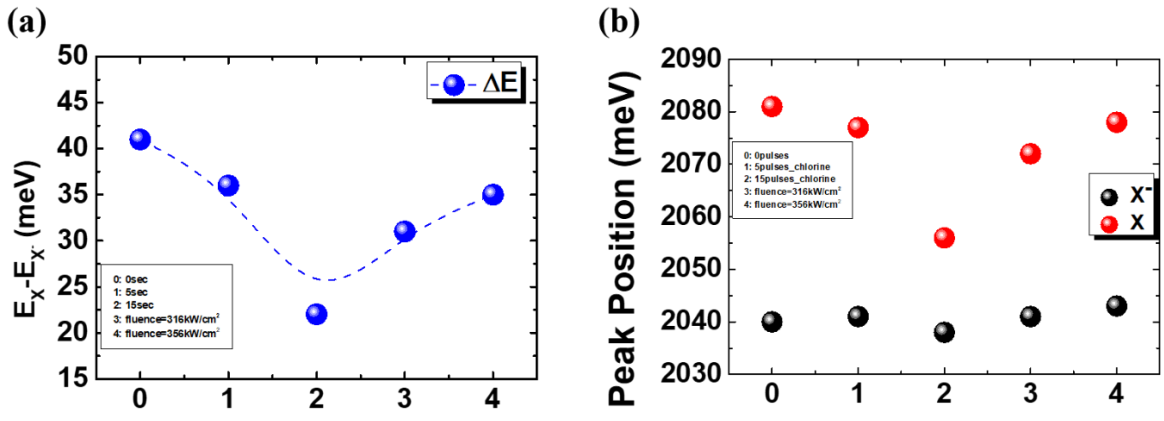

Figure 4.10 The observed photochlorination effect can be reversed upon CW laser (473nm) rastering of the chlorine-doped 1L-WS_2. (a) Following the CW laser treatment, the trion binding energy return to the levels corresponding to the pristine 1L-WS_2. (b) Similar results can be observed with the peak position of the neutral exciton (X).

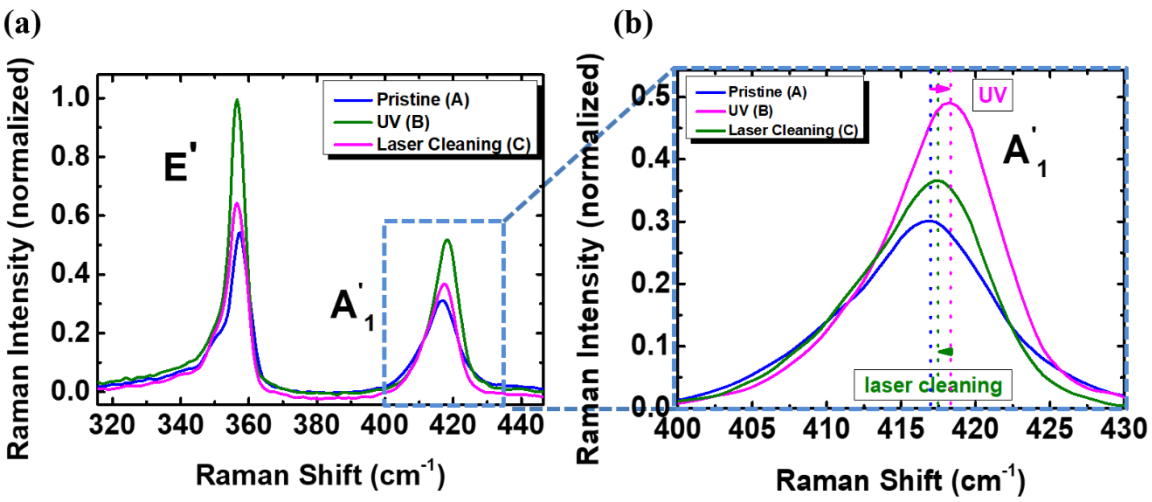

Figure 4.11 Following the CW laser treatment, the Raman A_1' mode position returns to the levels corresponding to the pristine 1L-WS_2.

The above results indicate the possibility of a laser-induced chlorination/dechlorination process enabling spatially selective doping changes with a beam size, i.e. micrometer, resolution. As proof of this concept, we have exposed part of a pristine (Fig. 4.12(a)) WS_2 monolayer to UV pulses in chlorine (Fig. 4.12(b)) and subsequently, we scanned the same area with a 473nm CW laser beam in the air (Fig. 4.12(c)). Fig. 4.12(d) shows the respective normalized-intensity PL spectra, indicating the reversibility of the photochlorination effect. Furthermore, due to the spatial control of photochlorination, we observe a much stronger PL emission by the photochlorinated area (area B in Fig. 4.12(b) and magenta curve in Fig. 4.12(d)) compared to the pristine one (area A in Fig. 4.12(b) and blue curve in Fig. 4.12(d)), which is restored to the levels of the monolayer in its pristine state upon CW laser cleaning (area C in Fig. 4.12(c) and green curve in Fig. 4.12(d)). This light-induced bidirectional doping process could potentially provide erasable regions of customized doping levels or even the formation of in-plane electronic junctions.

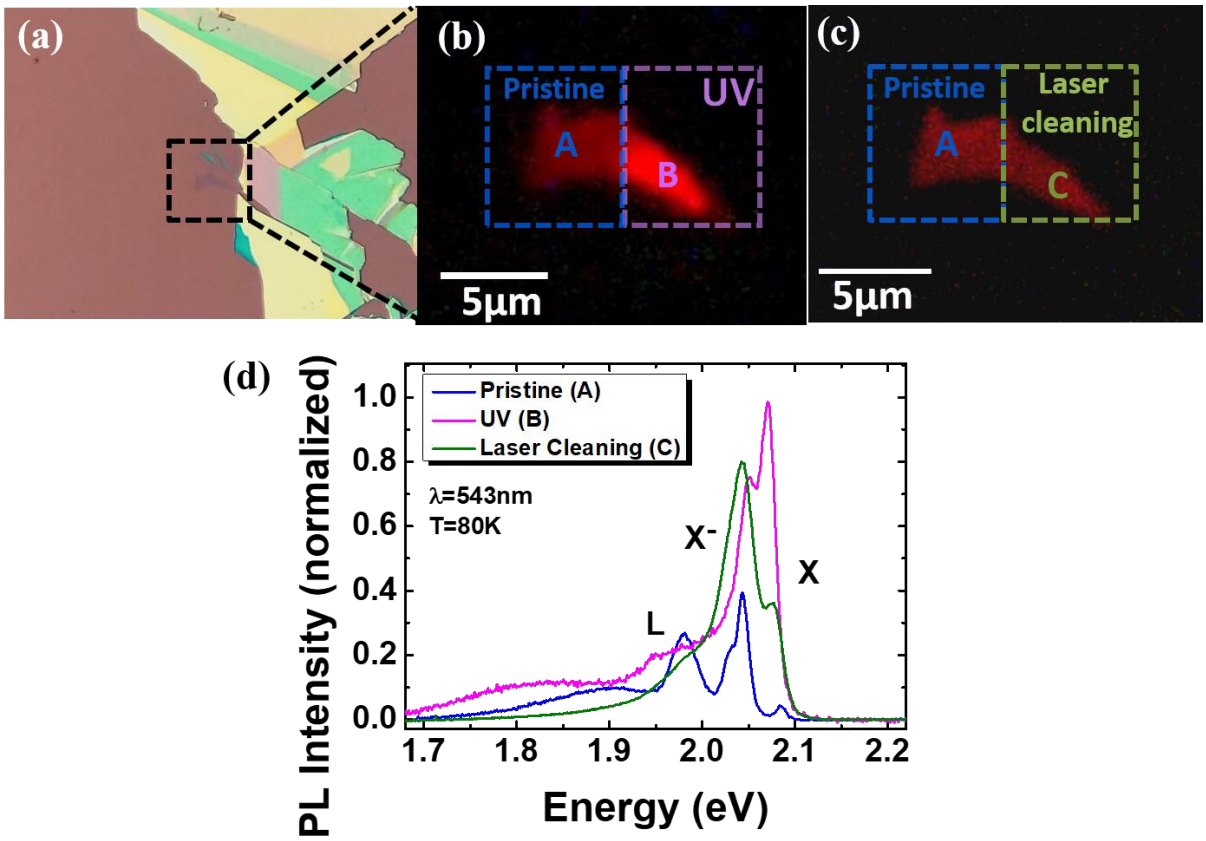

Figure 4.12 (a) Optical microscopy image of an exfoliated 1L-WS_2. (b) Fluorescence image of the monolayer following selective photochlorination of the area assigned as B, as indicated by the stronger PL emission compared to the area denoted as A. (c) Reversal of the photochlorination effect upon CW laser rastering of the chlorine-doped area, indicated by the suppression of the PL emission by the area assigned as C (d) The corresponding PL spectra of the pristine1L-WS_2 (blue curve), photochlorinated (magenta curve) and dechlorinated (green curve) areas.

4.1.3 Conclusions

In summary, we have demonstrated the spatially resolved and reversible tuning of the PL properties of 1L-WS_2 using a pulsed laser photodoping process. It is shown that the PL intensity can be significantly enhanced via the photo-assisted adsorption of p-type chlorine dopants to the monolayer lattice. This is due to the switching of the dominant PL process from the recombination of negative trions to that of neutral excitons, under the annihilation of residual electrons from the pristine crystal. DFT calculations confirm that chlorine adsorption can significantly affect the lattice electron density resulting in considerable shifts in the Fermi level position and to complete charge neutralization. Another remarkable finding is that the doping effect can be gradually reversed upon CW laser removal of the adsorbed chlorine species. This all-optical, bidirectional tuning of the electron density developed here can be advantageously used for spatially resolved doping modulation in 1L-WS_2 with micrometric resolution. It can therefore be important for the fabrication of TMD-based light-emitting and photovoltaic devices as well as in reducing the contact resistance between the TMD channel and the metal electrodes in field-effect transistors. Although in the present study we have introduced a photochemical chlorination method to control the carrier density in 1L-WS_2. This process can be readily extended to alternate combinations of dopants and TMD materials.

4.2 Tuning the valley polarization in WS_2 monolayers with photochemical doping

The sufficient control of the carrier density of a single layer WS_2 (1L-WS_2) has been realized by pulsed laser irradiation doping technique. Chlorine atoms are incorporated on the surface of the atomically thin lattice in a precursor gas atmosphere. This process has boosted interests in controlling valley polarized light emission of doped monolayer WS_2. In this thesis, we demonstrate spin-valley polarization tunability by more than 40% in 1L-WS_2 on hBN via photochlorination. Polarization photoluminescence spectroscopy was performed in the temperature range from 4K to 300K. The reduction of circular polarization after the photochlorination treatment was attributed to the reduction of defect sites in the crystal lattice and consequently to the increase of the non-radiative exciton lifetime. Ultrafast time-resolved transient absorption spectroscopy measurements support our findings.

4.2.1 Introduction

Single layers (1L) of transition metal dichalcogenides (TMDs) arise as an exciting class of atomically thin, two-dimensional (2D) materials for electronics, optics, and optoelectronics. [17,21,128,187,188] TMDs have demonstrated to be excellent candidates for field-effect transistors, photovoltaic cells, light-emitting diodes.[18,64,189] Apart from light-based applications, these materials are good candidates for quantum information processing based on valley degrees of freedom, valleytronics.[11,12,47,58,61,190] Additionally, they demonstrate high optical responsivity and sensitivity to the surrounding environment.[146] Their reduced dimensional hexagonal lattice combined with strong spin-orbit coupling and broken inversion symmetry, together with time-reversal symmetry lead to two non-equivalent K points in the Brillouin zone (K^+ and K^- respectively) and consequently to unique optical selection rules.[17,56,59] It is therefore possible to selectively populate and interrogate the K^+ and K^- valleys using circularly polarized light.[59,60,190]

These unique optical selection rules open up fascinating opportunities for carrier manipulation in different valleys.

Valley polarization can be affected by many experimental conditions, as we referred to in chapter 2.4. The emerging field of valleytronics has raised great interest in investigating valley polarized light emission of doped monolayer TMDs.

In this thesis, we demonstrate controllable tunability of the degree of spin-valley polarization of 1L-WS_2 using a pulsed laser photodoping process.[191] Motivated by recent theoretical and experimental studies based on carrier screening effects on excitonic valley relaxation in 2D semiconductors,[164,166,167] here we designed an approach to control the polarization degree (Pc) at liquid Helium temperature through chemical control of the carrier density upon photochlorination. Indeed, the PL intensity of the neutral exciton is significantly enhanced after several laser pulses in the chlorine environment and the circular polarization is decreased systematically. Using this approach, the doping-dependent circularly polarized PL of 1L-WS_2 at 4K under off-resonance excitation (2.28 eV) has been studied. In particular, the PL of neutral and charged exciton emission states monitored at different doping levels and a considerable modulation of P_C is demonstrated, attributed to the respective changes of the non-radiative exciton lifetime (τ_{NR}). Comparing these findings with doping dependent valley relaxation mechanisms,[164,167] we reveal the relationship between P_C and photochlorination doping. Low values of P_C are correlated with long τ_{NR} and a lower number of active defect sites. Our results demonstrate a significant tunability of circular polarization degree under effective chemical doping.

We fabricate and investigate two different types of samples: 1) monolayer WS_2 on a few-layer h-BN deposited on 285nm thick SiO_2/Si wafer, 2) monolayer WS_2 directly on SiO_2 substrate. Optical measurements were performed using the μ-PL setup for spin-valley polarization measurements with excitation wavelength 543nm. (Chapter 3.1.3 – Fig. 3.3) The exfoliated

monolayer sample size is approximately 10μm which is larger than the laser spot size (~1μm). The as-prepared WS_2 monolayer was subjected to irradiation by a KrF excimer UV laser beam emitting 20ns pulses of 248nm at 1Hz repetition rate that translated onto the monolayer area. More information about the photochlorination process is listed in chapter 3.3.

Transient absorption spectroscopy (TAS) measurements were performed on the as-prepared and the photo-chlorinated WS_2 monolayers for 10 seconds. A (Yb:KGW) femtosecond laser source was used with a pulse duration of 170 fs, 200 kHz repetition rate, and 1026 nm central wavelength. The beam split 90:10 to pump and probe respectively where the probe beam was guided through a delay line with time delay resolution of ~1fs. A BBO crystal was used to generate second harmonic (513nm) for the pump beam while the probe beam was focused into a sapphire crystal to produce a supercontinuum white light. The pump and the probe beam were focused using a 50x (NA:0.55, WD=13mm) objective lens in a collinear arrangement. The reflection of the probe from the sample was collected with an optical fiber coupled to a high sensitivity spectrograph. The spot size was 1.5μm in diameter for the probe beam and 6μm in diameter for the pump beam. The overall time delay resolution of the setup was 260fs.

4.2.2 Results and discussion

We examined flakes of WS_2 monolayers of ~10μm in lateral size, transferred on hBN by mechanical exfoliation. An optical microscope image of a representative WS_2/hBN is shown in Fig. 4.13 (a). Fig.4.13 (b) shows the corresponding Raman spectrum of the monolayer region taken at 295K with excitation energy of 473nm. The splitting of the in-plane E′ and the out-of-plane A_1' mode of the WS_2 confirms the monolayer character of the sample.[66] The peak at 1356cm^{-1} corresponds to the vibrational mode of the hBN supporting flake.[192] The effect of chlorination treatment on Raman scattering was studied in previous chapter. (Chapter 4.1)[191] PL spectra at 4K (and under 2.28eV excitation) analyzed for positive (red color) and negative (blue color) helicity at various photochlorination times are shown in Fig.4.13 (c). The main

emission channels are due to neutral excitons (X), trions or negatively charged excitons (X^-), and the biexcitons/localized-bound excitons (XX/L).[55] The neutral exciton is identified as the peak with the highest energy (2.09eV) while the charged exciton is at 2.05eV in the case of the pristine sample (t=0s). The neutral exciton (X) redshifts while the charged exciton (X^-) slightly blueshifts, which are signatures of photochlorination treatment. This phenomenon is clear from Fig. 4.13 (c).

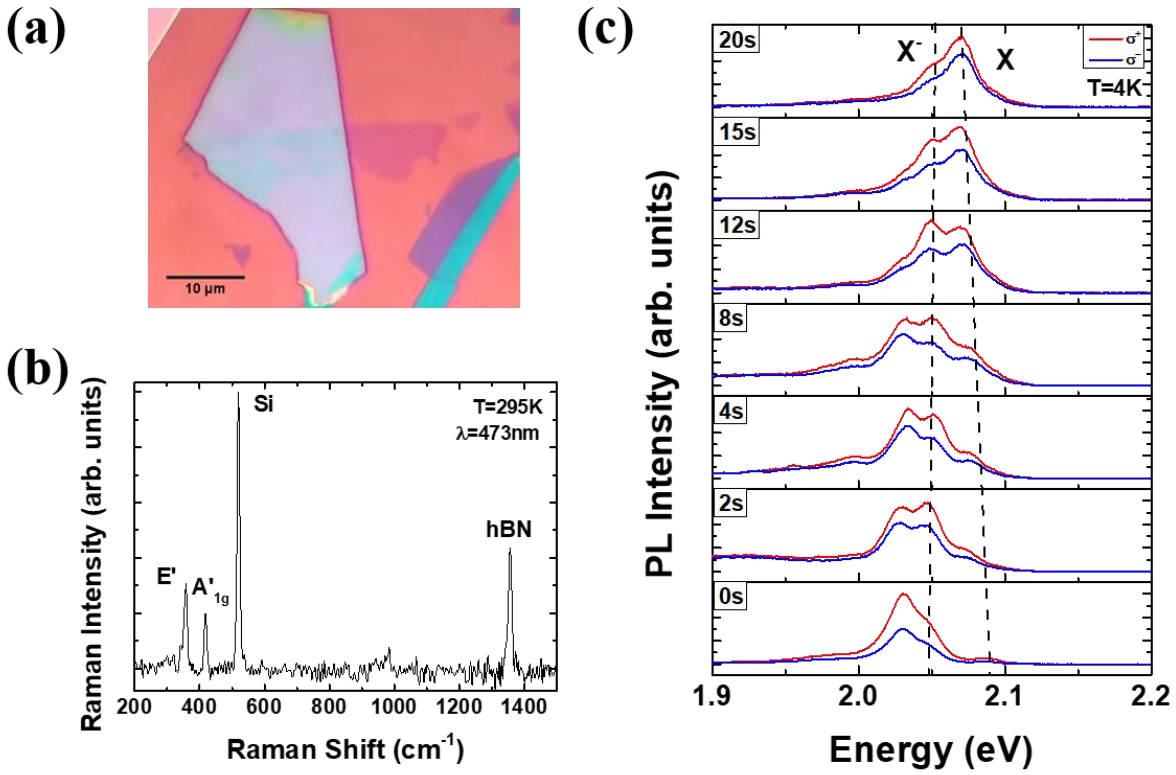

Figure 4.13 (a) Optical image of WS_2/hBN. (b) Raman spectrum at 295K with 473nm excitation laser line. (c) PL spectra at 4K excited with 543nm laser for different photochlorination times analyzed for σ+ (red) and σ- (blue) helicity.

More information about the behavior of PL components shown in Fig. 4.14. We can observe that excitonic peaks follow the same trend after doping steps, as we discussed in the previous chapter (Chapter 4.1). The repeatability and reproducibility of the photochlorination process are evident.

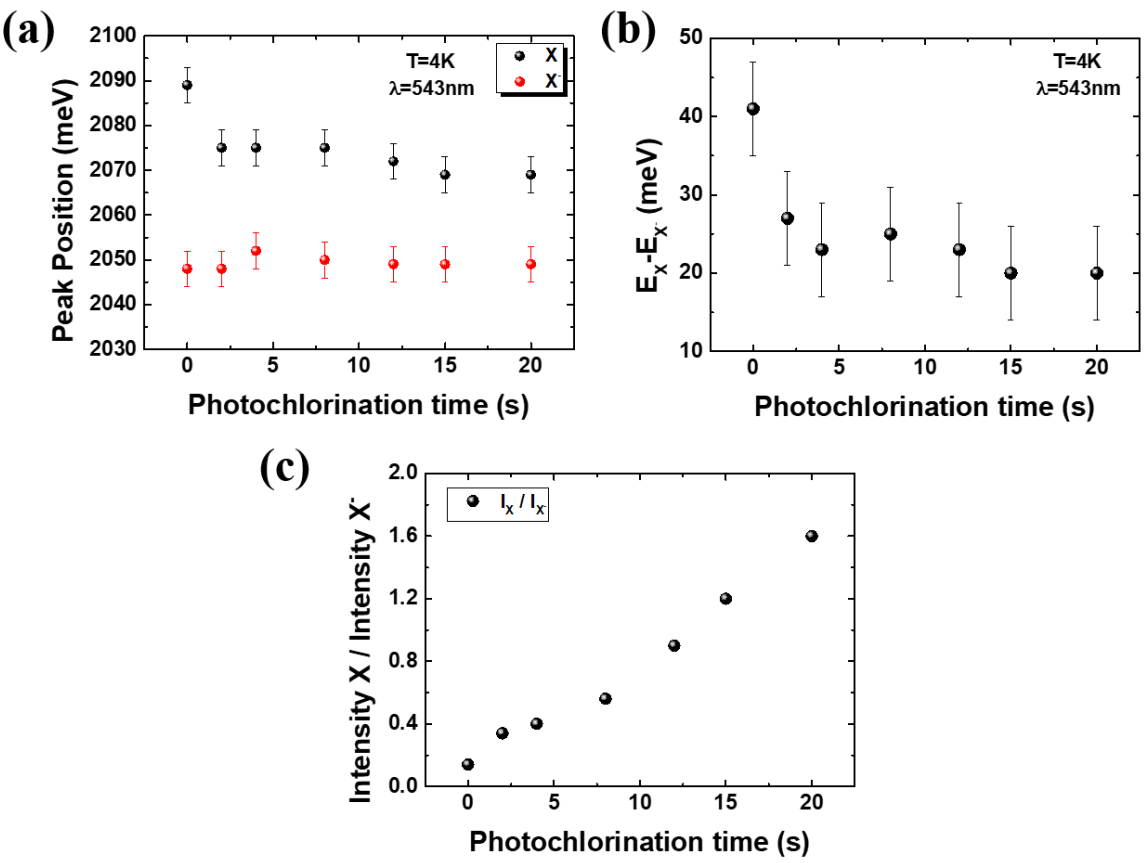

Figure 4.14 (a) Peak position of X and X^- of 1L-WS_2 on hBN as a function of the photochlorination time, at T=4K with excitation energy 2.28eV. (b) Dependence of the trion binding energy, corresponding to the energy difference between the X and X^- peaks, on the doping step (c) The intensity ratio I_X/I_{X^-} as a function of photochlorination time.

The corresponding intensities of neutral (Int of X) and charged exciton (Int of X^-) for different number of pulses in chlorine environment, that used to calculate the ratio of I_X/I_{X^-} in Fig. 4.14 (c) are recorded below in Table 1.

Table 1: The intensities of neutral (Int of X^0) and charged exciton (Int of X^-) for different number of pulses in chlorine environment.

Number of Pulses	Int of X	Int of X^-	Int X / Int X^-
0	1342	9638	0.14
2	1603	4668	0.34
4	2345	5792	0.4
8	2784	4980	0.56
12	4139	4593	0.9
15	3900	3216	1.2
20	2219	1399	1.6

For the analysis of the different emission peaks, we fit the spectra acquiring high values of coefficient of determination ($R^2 > 0.99$). The fitting analysis is included in Fig. 4.15.

The corresponding PL spectra deconvoluted into three peaks, the neutral exciton (X), charged exciton (X−), and emission from bound excitons (XX/L) peak assigned.

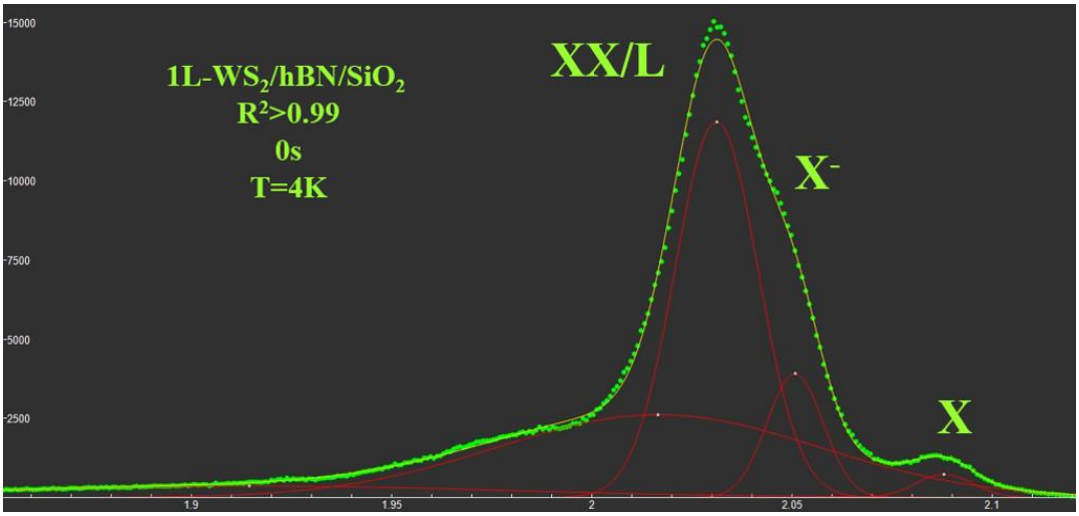

Figure 4.15 Voigt fitting of pristine 1L-WS_2/hBN/SiO_2 at 4K with excited energy 2.28eV. The green spots correspond to the experimental data, red curves represent the Voigt function of each component and the yellow line is the sum of the two functions.

It is important to note that X and X^- show similar values of polarization degree at all photochlorination times. The emergence of the charged exciton in the pristine 1L-WS_2 indicates the n-type nature of the crystal. At lower energies (2.03eV), we can observe the existence of localized/bound excitons (XX/L). This feature, which dominates at t=0s, is a signature for the presence of defect sites in the crystal lattice.[193] As the doping step increases, we observe two significant changes in the spectra: (a) the XX/L feature loses dramatically its intensity above 12s of photochlorination time and (b) the intensity of the neutral exciton increases significantly with respect to the trion intensity. The corresponding intensities of the neutral and charged exciton for different doping steps are presented in Table 1. Both changes strongly support the reduction of active defect sites in the lattice and at the same time the decrease of the intrinsic e-density. The chlorine creates a basal plane[191] that covers more and more defect sites that acted as non-radiative channels.

The circular polarization degree P_C is defined as $P_C = \frac{I_{\sigma^+} - I_{\sigma^-}}{I_{\sigma^+} + I_{\sigma^-}}$, where $I_{\sigma^+}/I_{\sigma^-}$ denotes the right/left hand circular polarization resolved PL intensity.[1159]

Using this equation and the data from Fig.4.13 (c), we evaluate the circular polarization P_C for the neutral exciton as a function of the photochlorination time at 4K and we plot these values in Fig.4.16 (a). We observe an almost linear depolarization as a function of photochlorination up to t=15s. At t=0s (pristine sample), we measure 33% polarization, which drops to 19% at t=15s, an almost 40% reduction. After t=15s, the circular polarization tends to saturate. The dependence of the polarization on the photochlorination time reflects the dependence on the electron density and consequently on the active defect sites that are responsible for the n-type character of WS_2.

The polarization study was completed by the temperature dependence of Pc for the neutral exciton for various chlorination times. Fig. 4.16 (b) shows this dependence for t=0s, 4s, and 20s treatment. There is a systematic monotonic depolarization, almost linear, for all treatment times

which is due to intervalley scattering. Insignificant variations of Pc across the same monolayer are observed, related to spatial non-uniformities across the monolayer surface of exfoliated 1L-WS_2.[176] The error bars of the circular polarization degree are given by taking into account both the deviation of scattered data from the averaged value at each temperature. Our experimental results, where the carrier density is controlled by photochemical doping in the chlorine environment, demonstrate the important role that the active defect sites have on the spin-valley polarization degree.

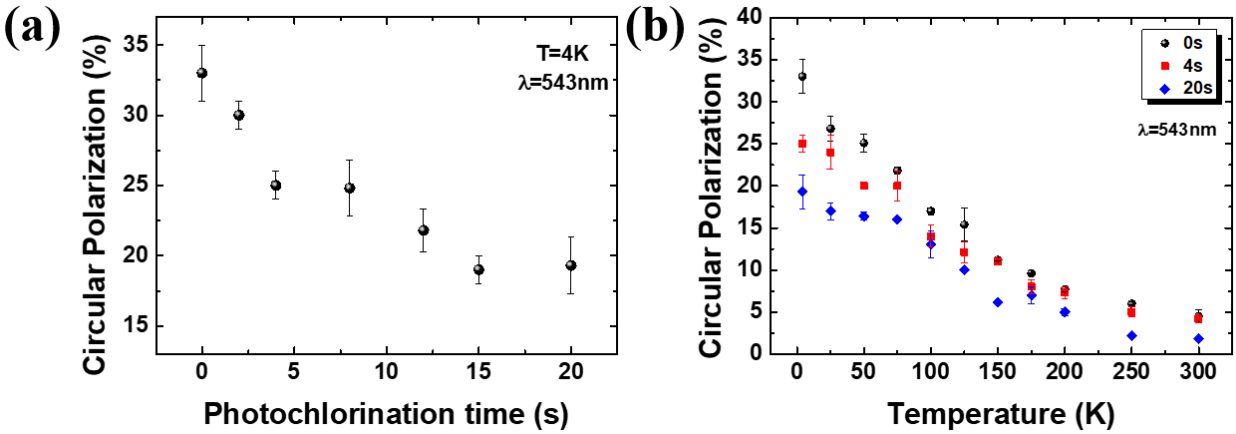

Figure 4.16 (a) Circular polarization as a function of the photochlorination time at T=4K. (b) Temperature dependence of the circular polarization for the neutral exciton for the pristine sample (black points) and for photochlorination times 4s (red) and 20s (blue). The photoluminescence was excited using the 543nm laser.

Let's return to Fig. 4.16 (a) that demonstrates the systematic tunability of the spin-valley polarization as a function of the photochlorination time at 4K, i.e. as a function of the effective electron density of the WS_2 monolayer. This e-density is not controlled electrically but rather chemically during the photochlorination treatment, affects the number of the defect sites on the lattice. Defects such as sulfur vacancies are the source of the n-type character of WS_2 and therefore controlling the active defect sites leads to control of the e-density, as it is the case in our system.

The change in valley polarization described, as we mentioned in Chapter 2.4, by a rate equation model leading to the following formula[61]:

$$P_C = \frac{P_0}{1 + 2\frac{\tau_r}{\tau_v}} \tag{4.2}$$

Where P_0 is the initial valley polarization generated in the system and τ_v^{-1} is the intervalley scattering rate. (Similar to Eq. 2.2) The exciton decay rate τ_r^{-1} includes both radiative (τ_R) and non-radiative (τ_{NR}) contributions:

$$\frac{1}{\tau_r} = \frac{1}{\tau_R} + \frac{1}{\tau_{NR}} \Rightarrow \tau_r = \frac{\tau_R \tau_{NR}}{\tau_R + \tau_{NR}} \tag{4.3}$$

Thus the valley polarization reads

$$P_C = \frac{P_0}{1 + 2\frac{\tau_R \tau_{NR}}{(\tau_R + \tau_{NR})\tau_v}} = \frac{P_0}{1 + 2\frac{A}{\frac{1}{\tau_{NR}} + B}} \tag{4.4}$$

where $B=\tau_R^{-1}$ and $A=\tau_v^{-1}$ are the radiative and valley scattering rates, respectively. We will use this equation to fit the experimental data of Fig. 4.16 (a). From the above equation is evident that the polarization is a function of the non-radiative lifetime (τ_{NR}) and depends on the parameters P_0, A, and B. It is known that for WS_2, τ_v at 4K is about 10ps and, most importantly, it does not depend on the carrier density.[167] We, therefore, fix it at A=0.1 ps^{-1}. Then we fit the data as a function of τ_{NR} for two extreme cases of P_0=40% (Fig. 4.17 (a)) and P_0=60% (Fig. 4.17 (b)) letting B as a free parameter. The best fit is for P_0=40% that gives τ_R=6.6ps and describes very well the depolarization at 4K as a function of the photochlorination time.

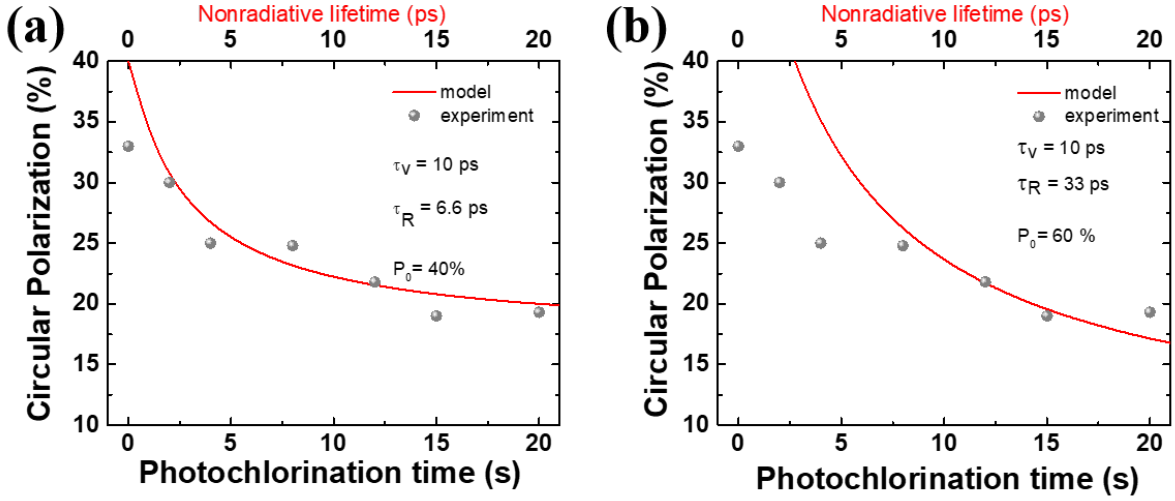

Figure 4.17 (a) Circular polarization as a function of the photochlorination time at 4K (gray points). The red line is the simulation using Eq. (4.4) with P_0=40% as a function of τ_{NR}. (b) Same as (a) using P_0=60%.

Fig.4.17 (a) strongly reveals the correlation between the treatment time and the increase in the non-radiative time. The non-radiative decay rate is related to the availability of trapping states. These states (sulfur vacancies) are filled as the number of pulses increases leading to a decrease of active defect sites and therefore to an increase in the non-radiative lifetime and a corresponding decrease in circular polarization. This point is obvious from Fig. 4.18 where we estimate the corresponding trap concentration for a typical semiconductor. A crude approximation of the non-radiative decay rate in a typical semiconductor is given by

$$\frac{1}{\tau_{NR}} = N_T u_e \sigma_e \qquad (4.5)$$

u_e: electron velocity

σ_e: electron trapping cross section

N_T: trap concentration

Choosing u_e=4x10^{6}cm/s , σ_e=10^{-10} cm^2, the non-radiative lifetime as a function of the trap concentration has the behavior of Fig. 4.18. It is clear that there is a strong correlation of the

non-radiative relaxation time to the defect trap density. Since the valley polarization saturates above 20 pulses (which roughly correspond to τ_{NR}=20ps), we can estimate the corresponding trap concentration to be of the order 10^{14} cm^{-3}.

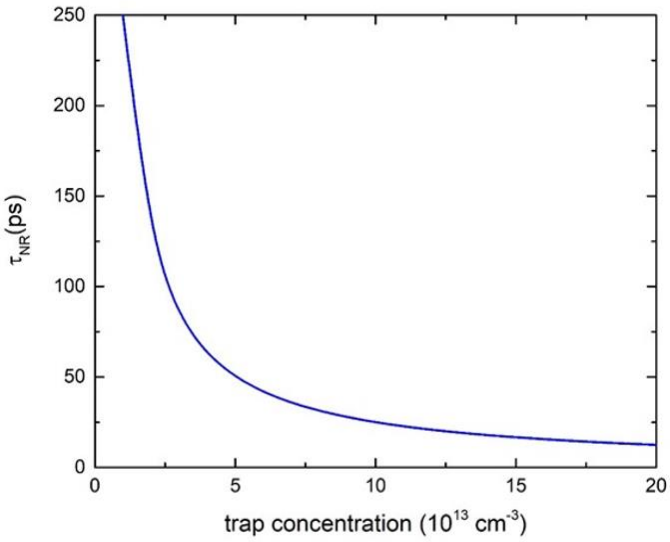

Figure 4.18 Non-radiative lifetime as a function of the trap concentration in a typical case.

We propose that the photochlorination process reduces the number of active defect sites and increases τ_{NR}. In a pristine monolayer, there are many defect sites and τ_{NR} is short, so we have fast non-radiative transitions. On the other hand, in a photo-chlorinated monolayer there are few defect sites and τ_{NR} is long, so we have slow non-radiative transitions. This phenomenon leads to the increase of the exciton radiative lifetime τ_r (effective lifetime) and consequently to a lower circular polarization, as we experimentally observe. The dependence of τ_r as a function of τ_{NR} is illustrated in Fig. 4.19. The effective exciton lifetime τ_r includes both the radiative (τ_R) and non-radiative lifetimes (τ_{NR}).

$$\frac{1}{\tau_r} = \frac{1}{\tau_R} + \frac{1}{\tau_{NR}} \Rightarrow \tau_r = \frac{\tau_R \tau_{NR}}{\tau_R + \tau_{NR}} \Rightarrow \tau_r = \frac{\tau_R}{1 + \frac{\tau_R}{\tau_{NR}}} \tag{4.6}$$

In Fig. 4.19, we plot the exciton effective lifetime (τ_r) as a function of the non-radiative lifetime (τ_{NR}), both in units of the radiative lifetime (τ_R). As the non-radiative lifetime increases, as in the case during photochlorination, the effective exciton lifetime increases too and approaches

its maximum value that corresponds to the radiative time. This increase leads to the reduction of the emitted circular polarization observed in the photochlorinated samples.

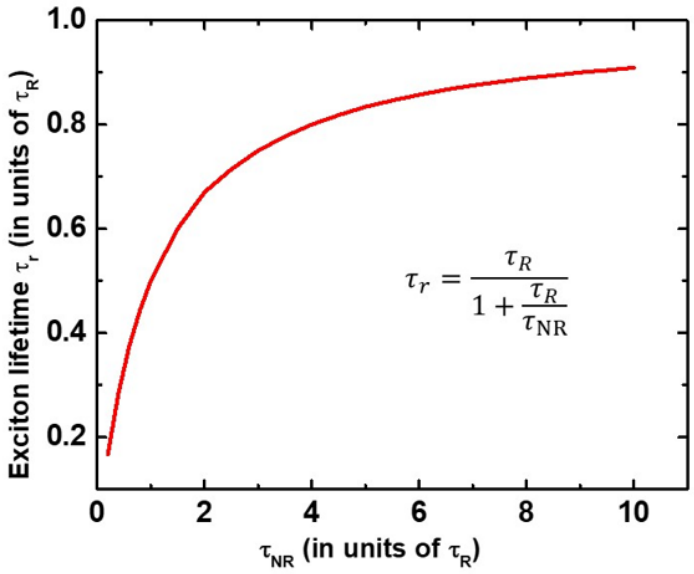

Figure 4.19 Exciton effective lifetime (τ_r) as a function of the non-radiative lifetime (τ_{NR}), both in units of the radiative lifetime (τ_R).

To further shed light on the decrease of circular polarization after the photochlorination treatment, we investigated the corresponding charge carrier relaxation dynamics utilizing ultrafast pump-probe time-resolved transient absorption spectroscopy (TAS). To examine the time evolution of the excitons, we have fitted the TAS signal with a multi-exponential decay equation containing three-time constants: T_1 assigned to Auger scattering, T_2 describes the non-radiative recombination channel due to rapid relaxation to surface defect sites, and T_3 is due to radiative recombination. We can observe from Fig. 4.20 that T_2 increases from 7±1ps for the pristine 1L-WS_2 to 39± 3ps for the photochlorinated sample. These values are not exactly the same as the predicted ones from Fig. 4.17 (a) that are based on a rate equation model, but certainly are in the same order of magnitude and follow a similar trend. An increase of T_2 (non-radiative recombination), as a result of the photochlorination process, indicates a reduction of the active defect sites and subsequently a decrease of the electron density. This is strongly supported from the data of Fig.4.13 (c) where the PL intensity of the charged exciton decreases while the intensity of the neutral exciton increases.

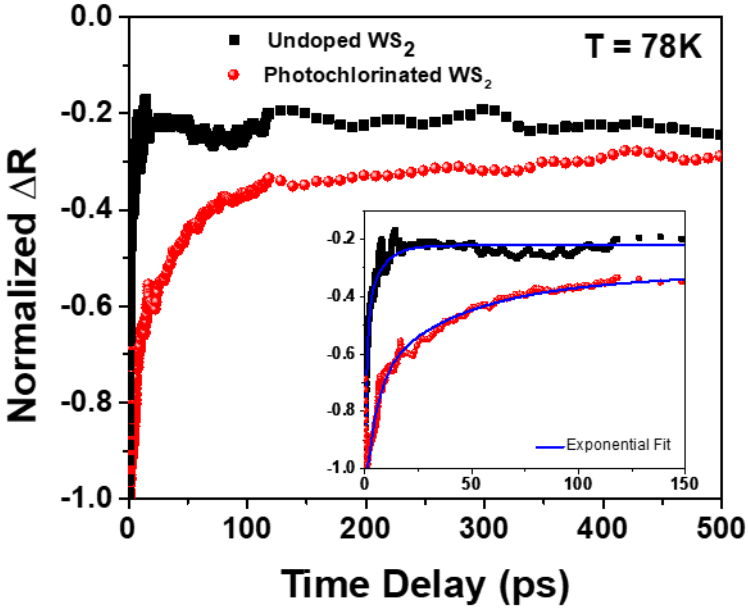

Figure 4.20 TAS spectra of the A-exciton for the photochlorinated WS_2 (red) and the as-prepared WS_2 (black) at 78K. Inset: Fitting the data for the photochlorinated sample yields a non-radiative lifetime of T2=39ps (red line) and T2=7ps for the as-prepared WS_2 (black line).

A photochlorinated WS_2 and as-prepared WS_2 monolayer samples were placed on a cryostat holder under vacuum with continuous liquid nitrogen flow. The temperature stabilized at 78K and the laser pump fluence set to 28 μJ/cm^2. During the experiment, two spectra of the probe taken at each delay time with and without pump. The differential reflectivity is defined as $\Delta R = R_{without\ pump} - R_{with\ pump}$. Fig. 4.20 presents the A exciton bleaching of the two samples with negative ΔR as a function of time delay. T_1=5.4±0.3ps, T_2=39± 3ps, and T3=627±57ps are the extracted relaxation times of the photochlorinated WS_2 and T_1=1.0±0.1ps, T_2=7±1ps, and T3=37±5ps are the extracted relaxation times of as-prepared WS_2.

The study on 1L-WS_2/hBN/SiO_2 also extended to 1L-WS_2/SiO_2 with very similar results. The corresponding PL spectra for 1L-WS_2/SiO_2 are illustrated in Fig. 4.21 (a). In Fig. 4.21 (b), the spin-valley polarization degree at 4K is plotted for different doping steps (from 0s to 20s) for the neutral exciton (X). The excitation wavelength is 543nm (2.28eV). At 4K we obtain 30% polarization for the as-prepared 1L-WS_2/SiO_2. At 4K and t=4s, we obtain 22% polarization and for t=20s, we get 18% polarization. It appears that the maximum spin-valley polarization degree

is achieved in the pristine 1L-WS_2/SiO_2 case, followed by the other photochlorination times, over the whole range of temperatures.

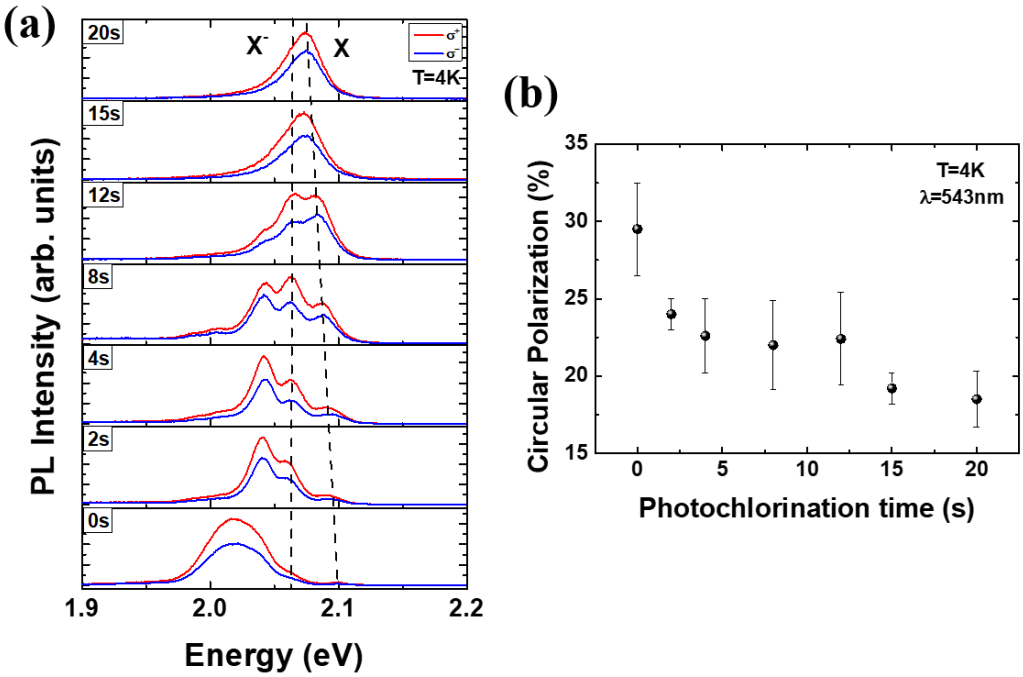

Figure 4.21 (a) Photoluminescence spectra analyzed for positive (σ +: red solid line) and negative (σ –: blue solid line) helicity of 1L-WS_2 on SiO_2 as a function of the photochlorination time. Spectra measured at 4K and the excitation was with an energy of 2.28 eV. (b) Circular polarization of neutral exciton of monolayer 1L-WS_2/SiO_2 at T=4K.

4.2.3 Conclusions

In conclusion, we have demonstrated high tunability of the valley polarization in a monolayer WS_2/hBN system using a photochlorination doping process. A reduction of more than 40% in the circular polarization of the neutral exciton at 4K was achieved. Similar results were also obtained for the 1L-WS_2/SiO_2 system. The decrease of the polarization was attributed to the reduction of the active defect sites as a result of the chlorine doping. That affects the non-radiative recombination time τ_{NR} and therefore the degree of the emitted circular polarization. Our results are supported by transient absorption spectroscopy measurements.

4.3 High room temperature valley polarization in WS_2/Graphite

Transition metal dichalcogenide (TMD) monolayers in the 2H-phase are two-dimensional semiconductors with two valleys in their band structure that can be selectively addressed using circularly polarized light. Their photoluminescence spectrum is characterized by neutral and charged excitons (trions). In a typical case of 1L-WS_2 on top of SiO_2, neutral and charged exciton emission have zero polarization at room temperature under on- and off-resonance measurements. In this chapter, we performed room-temperature valley polarization measurements of monolayer WS_2 with different substrates. By illuminating WS_2/Graphite with on-resonance (2.09eV) circularly polarized light at room temperature, we measure significantly large circular polarization (P_C up to 25%). Using the photochlorination process, we can modulate the polarization of the neutral exciton emission continuously from 27% to 38% for 1L-WS_2/Graphite. We show that valley polarization strongly depends on the relationship between the doping and the supporting layer of TMDs. These preliminary results shed light on the significant role of the substrate on valley polarization in monolayer TMDs.

4.3.1 Introduction

As we mentioned in previous chapters, when TMDs are excited with circularly polarized light, electron-hole pairs are created in a single valley. The subsequent radiative decay of excitons within this valley produces circularly polarized light due to optical selection rules. Therefore, measuring the circular polarization of PL provides a direct way to monitor the valley population. These populations are altered by intervalley scattering, a process that is enabled by phonons that conserve momentum or by exchange interactions. [61,152,194] At high temperatures or high photoexcitation energy, a large phonon population can readily couple the valleys, reducing valley specific populations. Because of this strong intervalley coupling, exciton polarization is often only seen in systems measured at low temperature or near-resonant

pumping conditions.[58,60,61,154,194] Many parameters can affect the degree of valley polarization. Here, we focus on the strong effect of substrate on circular polarization for 1L-WS_2 and the reasons for a substrate like graphite maintain high values of polarization at room temperature.

For applications, it is very important to measure a high degree of circular polarization at room temperature. Spintronics and valleytronics fundamentally differ from conventional electronics in that, in addition to a charge state, electron spins and valley-index exploited as a further degree of freedom, with implications in the efficiency of data storage and transfer. As a result, these devices gain particular interest in the field of quantum computing.

Unfortunately, valley depolarization in 1L-TMDs occurs on picosecond timescales. [168,195,196] As a result, high degrees of circular polarization have demonstrated at cryogenic temperatures, [12,58–61,154,168,195] where the exciton lifetime is on the order of a few ps only[197]. The major challenge is the high degree of P_C at room temperature, where the effective exciton lifetime typically exceeds 100ps in 1L-TMDs.[197,198] Room temperature valley polarization has been observed in 1L-MoS_2 [154] and 1L-WS_2. [199,200] Obtaining robust RT valley contrasts in 1L-TMD is challenging but is, at the same time, a key for emerging opto-spintronic and -valleytronic devices.[201,202] Such devices typically consist of (i) 1L-TMD as a chiral optical material and/or as an injector of spin/valley polarized electrons with (ii) graphene as a high mobility channel for efficient spin-polarized electron transport.[203–205] Many research teams demonstrate that monolayer TMD directly stacked onto graphene provides highly stable room-temperature valley polarization.[158,206,207] Motivated by these experimental works based on high room temperature valley polarization on 1L-TMD/Graphene heterostructures, we fabricate and investigate different types of samples with reference point the 1L-WS_2.

We performed on-resonance (2.09eV excitation) and off-resonance (2.28eV excitation) valley polarization measurements at 295K at van der Waals heterostructures consist of 1L-WS_2 and different types of substrates. More specific, these types are listed below:

1) 1L-WS_2 on monolayer graphene

2) 1L-WS_2 on few layers graphene

3) 1L-WS_2 on graphite

4) 1L-WS_2 on Silicon dioxide (SiO_2)

5) 1L-WS_2 on hexagonal Boron Nitride (hBN)

6) 1L-WS_2 on Indium Tin Oxide (ITO)

7) 1L-WS_2 on 50nm layer thick gold (Au)

We observed that only three types of samples give a high degree of circular polarization (P_C) at near resonance conditions. These types of samples are 1L-WS_2 on top of one and few layers of graphene, as expected, and the 1L-WS_2 on graphite. This result gives rise to further measurements at low and room temperature conditions. Also, we investigate the behavior of 1L-WS_2/Graphite in chlorine environment with promising results.

The circular polarization degree P_C, as we mentioned in Chapter 4.2, is defined as $P_C = \frac{I_{\sigma^+} - I_{\sigma^-}}{I_{\sigma^+} + I_{\sigma^-}}$, where $I_{\sigma^+}/I_{\sigma^-}$ denotes the right/left hand circular polarization resolved PL intensity.

4.3.2 Results and discussion

We investigate seven different cases of samples. Fig. 4.22 and 4.23 illustrated the optical images and the characteristic Raman spectra. Fig. 4.22 shows three different types of samples, 1L-WS2 on top of 1L-graphene, on top of a few layers of graphene and graphite. The G and 2D Raman peaks change in shape, position, and relative intensity with the number of graphene layers. This reflects the evolution of the electronic structure and electron-phonon interactions. Raman Spectroscopy is used to monitor the number of graphene layers.[71] Fig. 4.22 (c) compares the Raman spectra of 1L-graphene, few layers of graphene, and bulk graphite measured at 295K and 473nm laser excitation. The two most intense features are the G peak at 1580cm^{-1} and a band at ~2700cm^{-1}, which is the second-order most prominent band referred to as the 2G peak. A significant change in the shape and intensity of the 2D peak of graphene compared with graphite is obvious. The 2D peak in bulk graphite consists of two components, $2D_1$ and $2D_2$, roughly ¼ and ½ the height of the G peak, respectively. Monolayer graphene has a single sharp 2D peak, roughly four times more intense than the G peak. A further increase in the number of layers leads to a significant decrease in the relative intensity of the lower frequency 2D1 peaks. For more than five layers, the Raman spectrum becomes hardly distinguishable from that of bulk graphite. Thus Raman spectroscopy can identify a single layer from bi-layer and few (less than five) layers. In Fig. 4.23 are presented the Raman spectra for the remaining four cases. All the samples fabricated with the exfoliated method except from gold (Au), where 50nm thick film of Au are deposed in SiO_2 by sputtering. Raman spectrum of the exfoliated hBN onto SiO_2 shows a Raman band at 1364 cm^{-1} (magenta line).

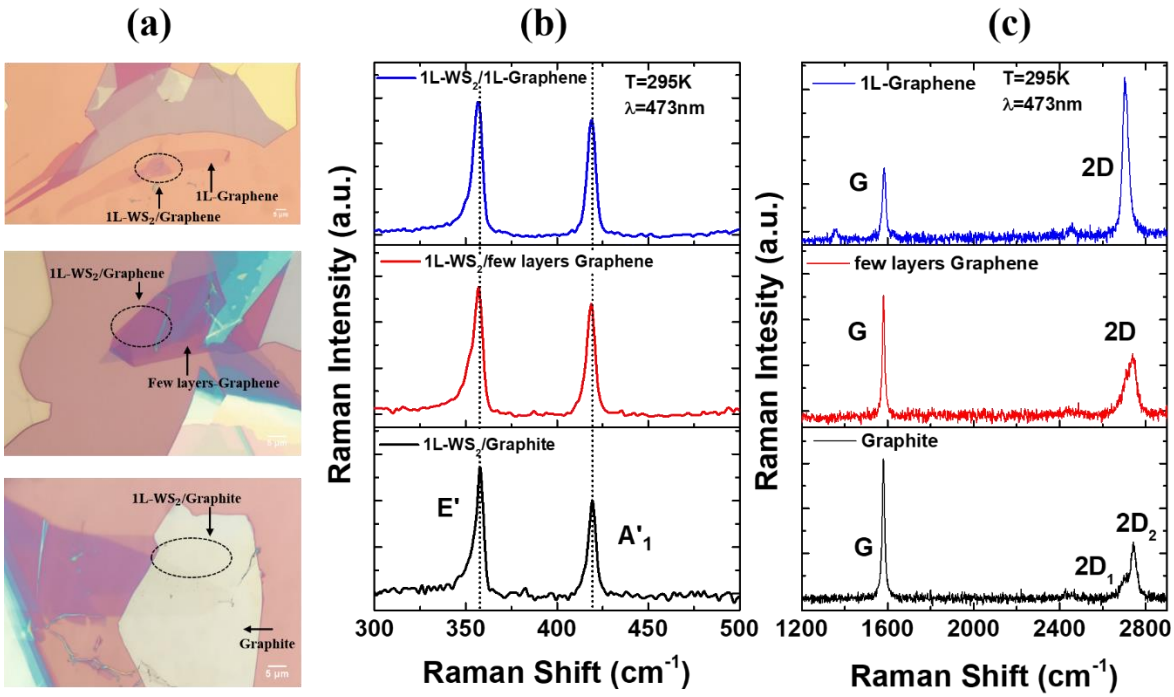

Figure 4.22 (a) Optical image of 3 different cases. (b) Raman spectra at T=295K with laser excitation 473nm for 1L-WS_2 on top of 1L-Graphene (blue line), for 1L-WS_2 on top of few layers of graphene (red line) and 1L-WS_2 on top of graphite (black line) (c) Raman spectra of the supporting 1L-graphene (blue line), few layers graphene (red line) and graphite (black line).

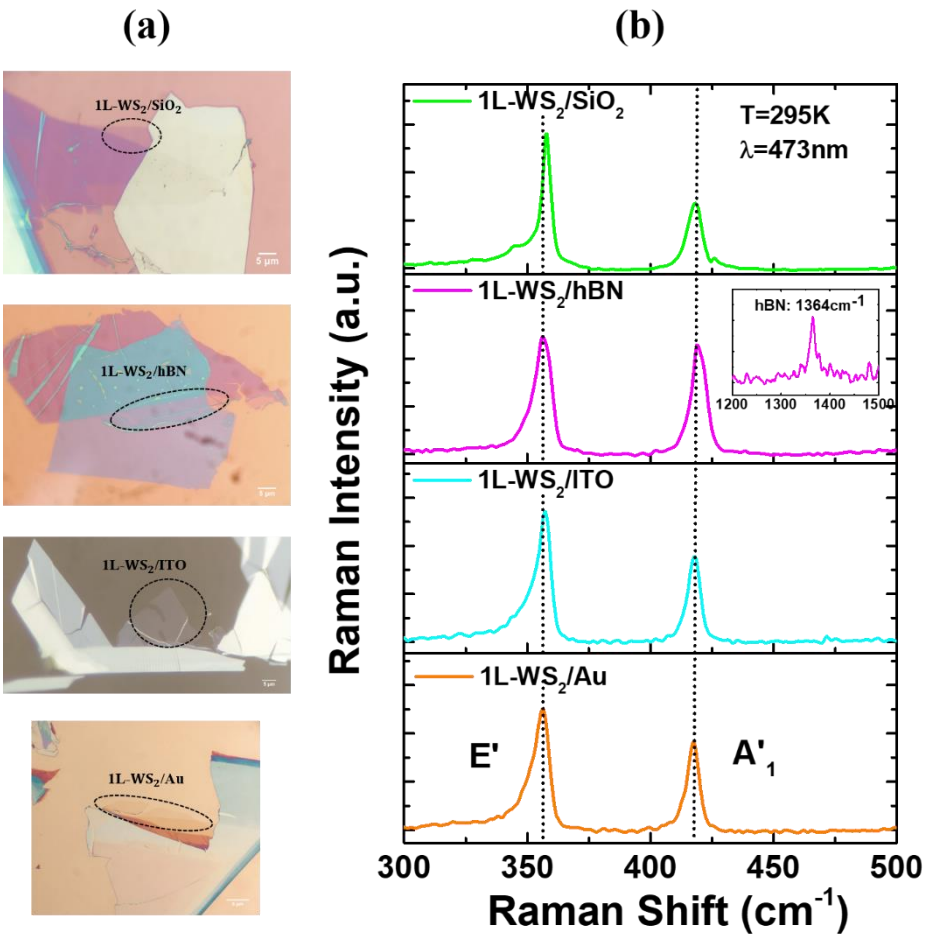

Figure 4.23 (α) Optical image for the remaining 4 cases (b) Raman spectra at T=295K with laser excitation 473nm for 1L-WS_2 on top of SiO_2 (green line), for 1L-WS_2 on top of hBN (magenta line), for 1L-WS_2 on top of ITO (cyan line) and 1L-WS_2 on top of Au (orange line).

In the following, we present room temperature spin-valley polarization measurements with (a) 594nm (2.09eV) and (b) 543nm (2.28eV) laser excitation. It is obvious that only at on-resonance (2.09eV) conditions and in the case of 1L/few layers of graphene and on graphite, the degree of valley polarization is high. In table 2 are listed the values of circular polarization for all the cases. The degree of circular polarization on top of 1L and a few layers of graphene is high enough, as it was previously demonstrated.[206] We measure 33% and 32% for 1L and a few layers of graphene, respectively, at room temperature conditions. The surprising result is that on top of graphite. We measure 25% circular polarization at room temperature. Monolayer WS_2 on top of graphene/graphite shows a single excitonic photoluminescence peak with a Lorentzian profile and a very small full width at half maximum (FWHM) of ~14meV at room temperature. In a typical exfoliated 1L-WS_2/SiO_2, a trion feature appears at the lower energy side due to unintentional doping of the sample. Asymmetric and broad peaks are observed in other cases. In the case of WS_2 on top of graphene/graphite, the trion feature disappears since residual charges in the WS_2 could flow into lower energy states via static charge transfer in the semi-metallic graphene and metallic graphite layer. The Fermi energy for these materials located in the gap of the WS_2.

The dependence of the peak energy on the substrate (Fig. 4.24, Table 2) is mainly attributed to the effect of both lattice strain and dielectric screening. Dielectric screening is known that affect the excitonic transition energy of the low dimensional semiconductors. Similar studies indicate that the lattice strain and electronic properties of WS_2 are uniform on the graphite substrates.[208] We attributed the redshift of the neutral exciton (Fig. 4.24) to screening by the dielectric environment associated with graphene and graphite. The observed shift in the exciton transition energy reflects the combination of a significant renormalization of the quasiparticle bandgap and a decrease in the exciton binding energy. The charge neutrality of WS_2 on top of

graphene/graphite is due to the energy and charge transfer of photoexcited carriers from WS_2 to graphene/graphite. The circular polarization (P_C), peak energies, and FWHM are given in Table 2.

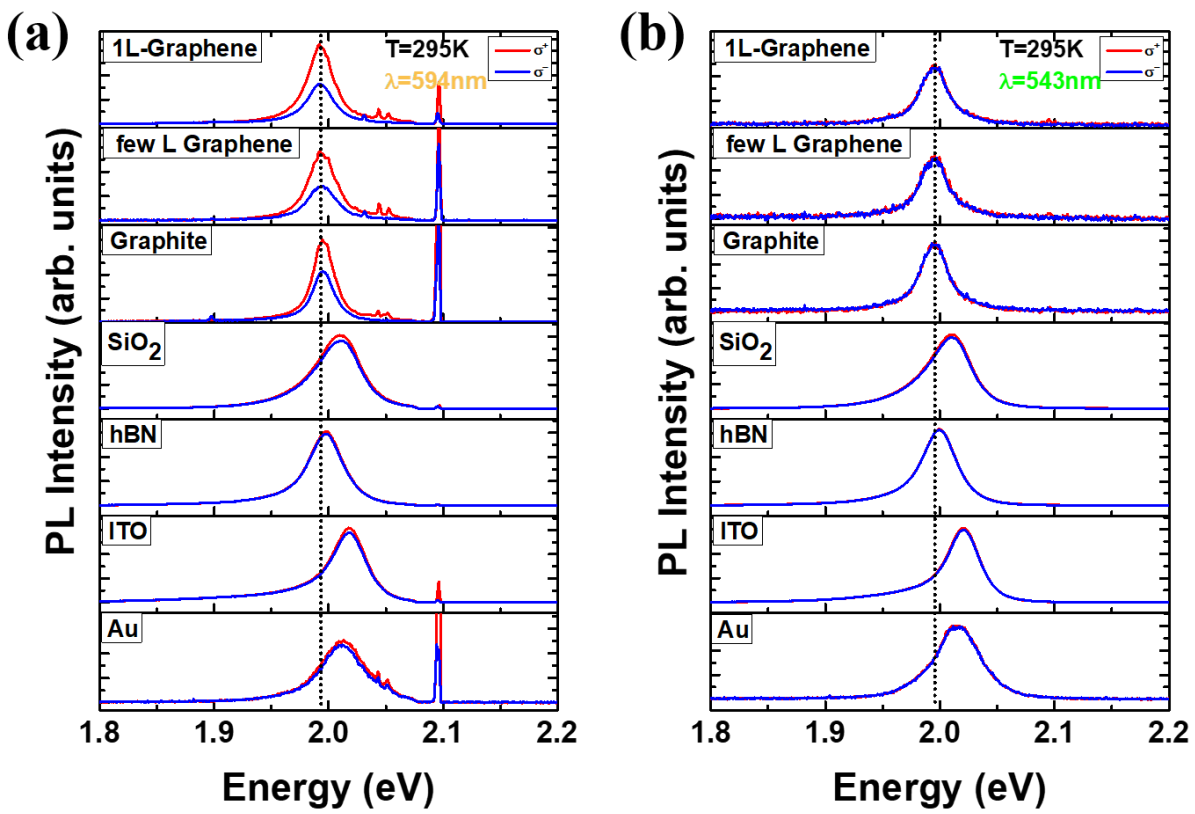

Figure 4.24 (a) Photoluminescence spectra analyzed for positive (σ +: red solid line) and negative (σ –: blue solid line) helicity for seven different cases. Spectra measured at 295K and the excitation was with energy of (a) 2.09eV and (b) 2.28 eV.

Table 2: Circular Polarization, peak position and FWHM of neutral exciton at T=295K.

Type of sample	λ=594nm P_C (%)	λ=543nm P_C (%)	Peak Position (eV)	FWHM (meV)
1L-WS_2/1L-Graphene	33	2	1.991	16
1L-WS_2/few layers Graphene	32	1	1.991	14
1L-WS_2/Graphite	25	1	1.994	14
1L-WS_2/SiO_2	4	2	2.013	24
1L-WS_2/hBN	2	1	2.000	22
1L-ITO	3	1	2.018	21
1L-WS_2/Au	4	1	2.013	21

In the WS_2/graphene and WS_2/graphite systems, the strong interlayer interaction leads to a significant PL quenching due to a fast non-radiative charge transfer from the WS_2 to the underlying layers.

In the following pages, we will focus on graphene and graphite. We will start with 1L-Graphene (Fig. 4.25 (a)). We expose the sample in the chlorine environment and the results after the photochlorination treatment are presented in Fig. 4.25 (b), (c), and (d).

Raman spectra of 1L-WS_2 on top of 1L-Graphene measured at 295K with laser excitation 473nm before and after photochlorination. A slight blue shift of out-of plane mode A_1' (Fig. 4.25(b)) after the photochlorination is observed (magenta line), but the G and 2D peaks from graphene are unaffected. This shift of A_1' is an indication of the chlorine effect on 1L-WS_2.[191] The behavior of neutral exciton in the photoluminescence spectra with the photochlorination treatment (Fig. 4.25 (c)) is similar to previous results in chapters 4.1[191] and 4.2. Valley polarization measurements were performed for two different types of substrates, 1L-graphene and SiO_2 at the same time. The shape and peak position of neutral exciton of 1L-WS_2 is different for 1L-graphene and SiO_2. A systematic redshift of the neutral exciton for both types appeared after several pulses in the chlorine environment. The results of circular polarization after the photochlorination treatment give some first signs of an increase in polarization degree (Fig. 4.25(d)). Fig. 4.26 is a clear picture of the difference between 1L-Graphene and SiO_2. When we use as a substrate for 1L-WS_2 the 1L-Graphene, the degree of circular polarization is high, in contrast with SiO_2, which is almost zero. The redshift of neutral exciton as the photochlorination step increases is shown in both cases (Fig. 4.26 (a) and (b)).

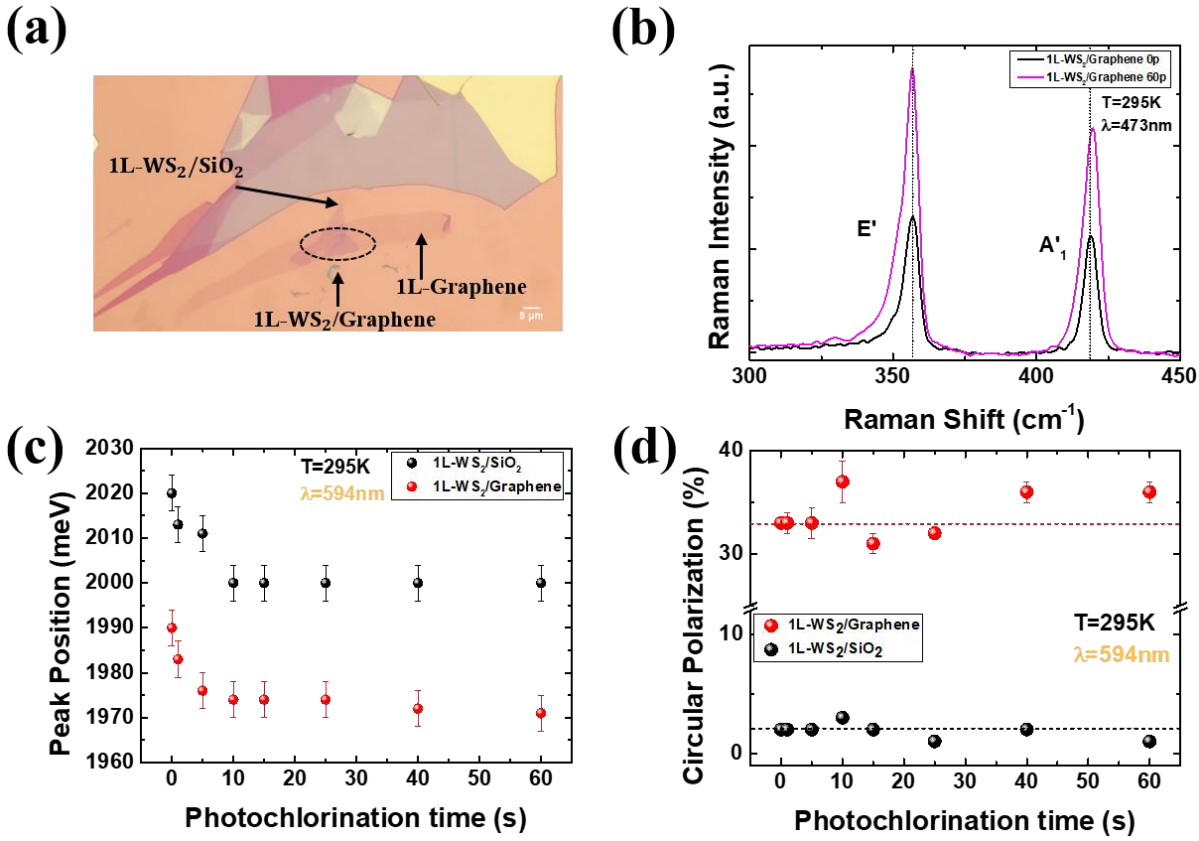

Figure 4.25 (a) Optical image of 1L-WS_2 on top of 1L-Graphene (b) Raman spectra before (black line) and after (magenta line) photochlorination treatment. (c) The peak position of the neutral exciton (X) for 1L-WS_2/SiO_2 (black bullets) and 1L-WS_2/1L-Graphene (red bullets) (d) Circular Polarization of 1L-WS_2/SiO_2 (black bullets) and 1L-WS_2/1L-Graphene (red bullets) as the photochlorination time increases.

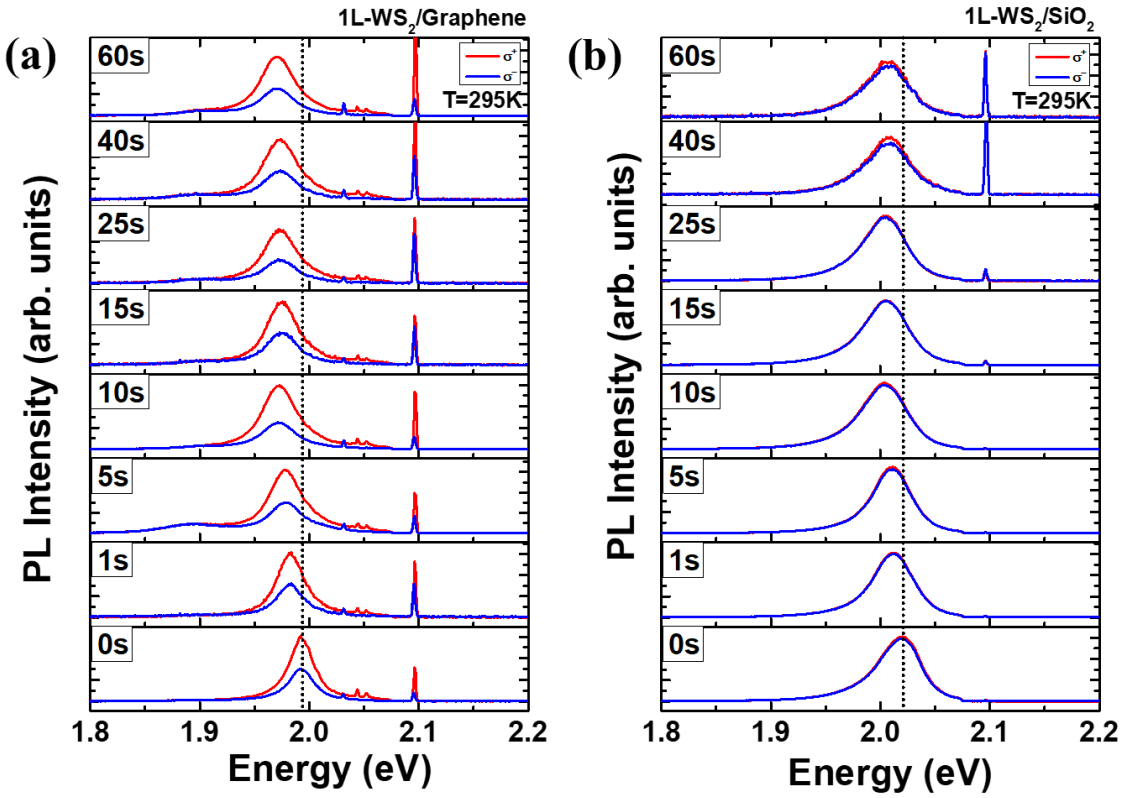

Figure 4.26 Photoluminescence spectra analyzed for positive (σ +: red solid line) and negative (σ –: blue solid line) helicity as a function of photochlorination time. Spectra measured at 295K with excitation energy 2.09eV for (a) 1L-WS_2 on top of 1L-Graphene and (b) 1L-WS_2 on top of SiO_2.

Similar studies took place for a few layers of graphene at several temperatures. Fig. 4.27 shows the photoluminescence spectra for 1L-WS_2 on top of few layers of graphene at (a) 200K, (b) 250K, and (c) 300K and for different number of pulses. At lower temperatures, we can't get reliable data because of the presence of strong Raman peaks. The Raman modes have a strong circular polarization and it is impossible to extract reliable information for the polarization of the neutral exciton. In Fig. 4.27 (d), (e), (f), we plot the circular polarization as a function of the photochlorination step. For one more time, we observe an increase in circular polarization. We investigate a various number of layers of graphene (1L and few layers) as a substrate, and the results have the same response.

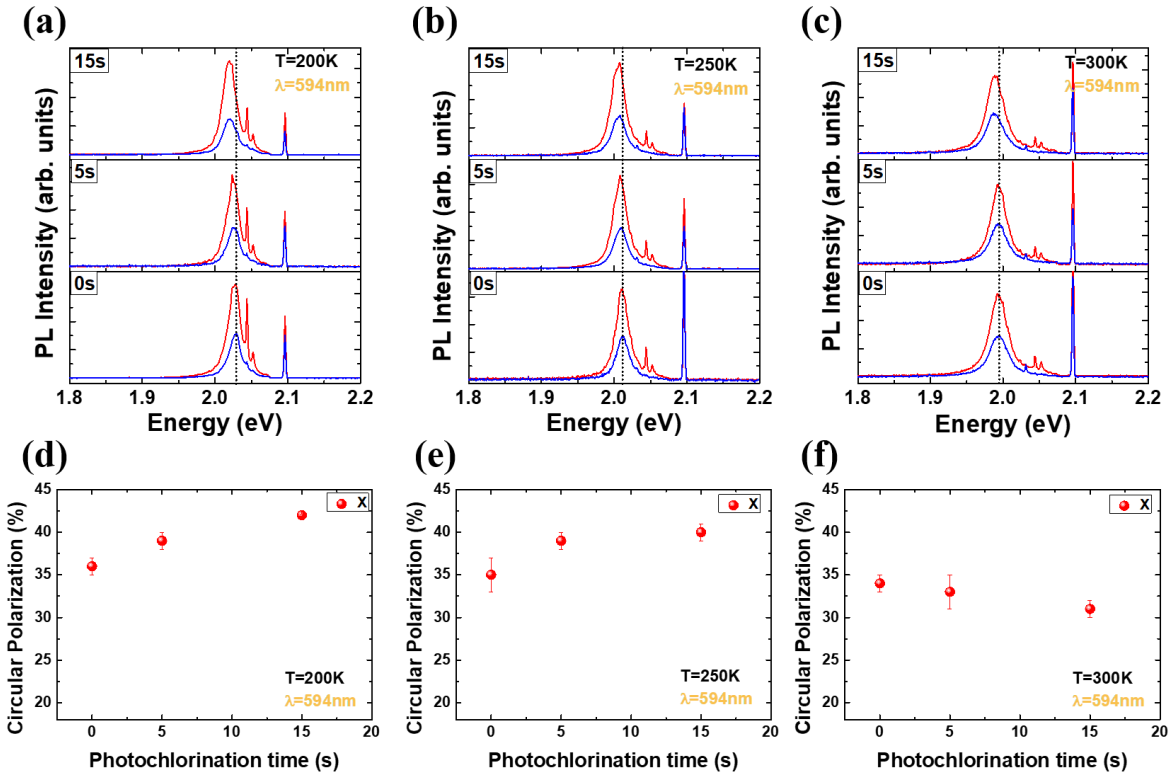

Figure 4.27 Photoluminescence spectra of 1L-WS_2 on top of a few layers of graphene analyzed for positive (σ +: red solid line) and negative (σ –: blue solid line) helicity as a function of photochlorination time for three different temperatures (a) T=200K (b) T=250K (c) T=300K. Circular Polarization of 1L-WS_2 on top of a few layers of graphene as a function of photochlorination time for three different temperatures (d) T=200K (e) T=250K (f) T=300K.

We will continue the analysis with the most exciting type of heterostructure in this project, 1L-WS_2 on top of exfoliated Graphite. Monolayer WS_2 presents a uniform, single excitonic photoluminescence at 1.99eV at room temperature. The position of the neutral exciton is redshifted by 0.02eV compared to the typical case of 1L-WS_2/SiO_2. In this sample, no additional peaks were observed for charged or bound excitons, even at low temperatures (Fig. 4.28 (a), (b), (c)). Circular polarization measurements were performed on 1L-WS_2/Graphite at temperatures higher than 200K in order to avoid the Raman peaks. The degree of circular polarization is high at all temperatures. At room temperature, from 24% for the pristine sample it reaches 33% after 40 pulses in the chlorine environment. This value is a significant value for room temperature valley polarization. The graphite seems to be the ideal substrate for valley polarization measurements for TMDs. The error bars in Fig. 4.28 (d), (e), and (f) are small and indistinguishable.

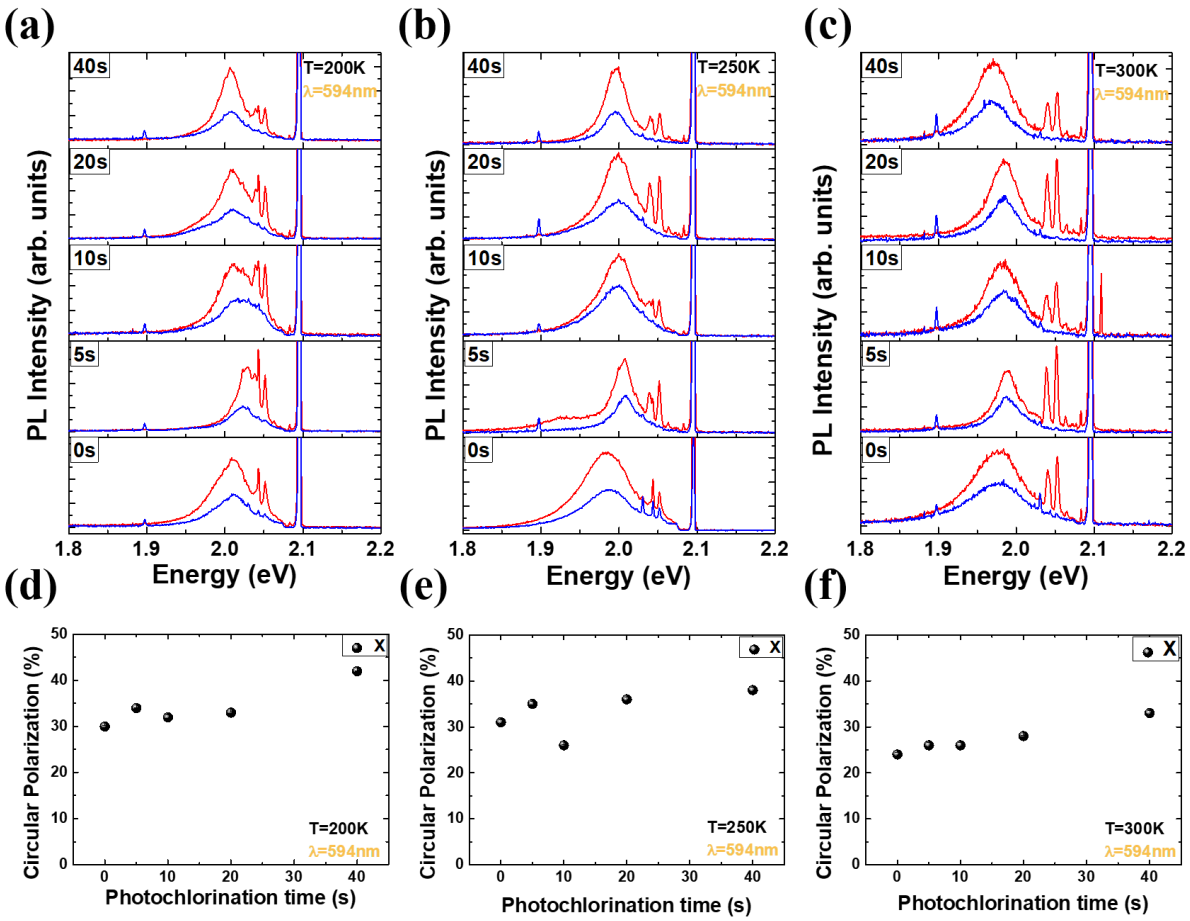

Figure 4.28 Photoluminescence spectra of 1L-WS_2/Graphite analyzed for positive (σ +: red solid line) and negative (σ –: blue solid line) helicity as a function of photochlorination time for three different temperatures (a) T=200K (b) T=250K (c) T=300K. Circular Polarization of 1L-WS_2/Graphite as a function of photochlorination time for three different temperatures (d) T=200K (e) T=250K (f) T=300K.

Next we compare the response of the WS_2/graphite system under two different gases. We perform the same experimental photodoping procedure for two different samples of 1L-WS_2/Graphite at room temperature and with the same KrF excimer UV laser (248nm). The gas pressure into the chamber was 120Torr for chlorine and nitrogen (Chapter 3.3). The only parameter that changes here is the type of gas in the chamber. Fig. 4.29 (a) and (c) represent the results after several pulses in a chlorine environment and Fig. 4.29 (b) and (d) after several pulses in a nitrogen environment. The degree of circular polarization was maintained at high levels (over 23%) for both samples. A remarkable increase of polarization after photochlorination is noted (from 27% to 38%) contrary to the nitrogen (Fig. 4.29 (e)). Even after 40 pulses in the nitrogen environment, the circular polarization is almost unaffected (Fig. 4.29 (d) and (e)). Furthermore, after several pulses in the chlorine environment, the neutral exciton redshifted, as we observed in Fig. 4.28 (f) and chapters 4.1 and 4.2. In the case of nitrogen, the peak position of the neutral exciton is fixed (Fig. 4.29 (d) and (f)) by varying the number of pulses.

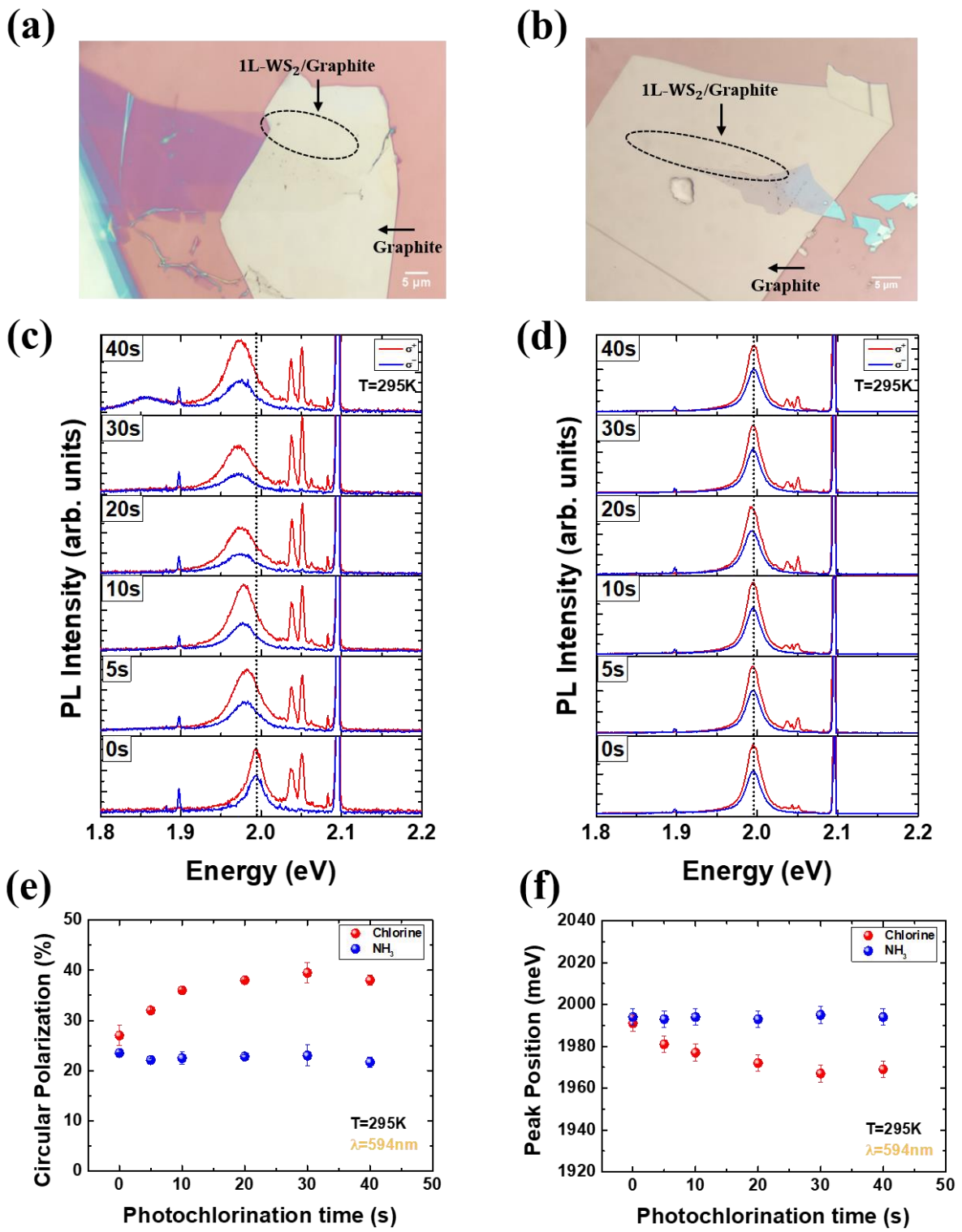

Figure 4.29 Chlorine vs Ammonia (a) (b) Optical image of 1L-WS_2 on top of graphite. (c) Photoluminescence spectra of 1L-WS_2 on top of graphite analyzed for positive (σ +: red solid line) and negative (σ –: blue solid line) helicity as a function of photochlorination time (d) Photoluminescence spectra of 1L-WS_2/Graphite after several pulses in nitrogen environment (e) Circular Polarization of 1L-WS_2/Graphite as the photodoping time increases at T=295K with excitation energy 2.09eV in chlorine environment (red bullets) and nitrogen environment (blue bullets). (f) The peak position of neutral exciton of 1L-WS_2/Graphite as the photodoping time increases.

4.3.3 Conclusions

These findings provide an alternative method to keep in high levels the circular polarization by using graphite as a supporting layer for 1L-WS_2. Furthermore, we proved that the photochlorination process not only conserves circular polarization at high levels in room temperature but is an indicator to measure circular polarization over 30% at non-cryogenic conditions. Considering monolayer TMDs on top of substrates such as SiO_2/Si, graphene and graphite conclude that substrate is one of the essential factors for measuring a high degree of circular polarization at room temperature.

Chapter V
Conclusions

Atomically thin TMDs have attracted tremendous attention owing to their novel physical properties and great potential applications in electronic and optoelectronic devices. The results presented here aimed at the understanding of the main reasons that affect the carrier density and optical properties of TMDs. This thesis presents a reliable photoinduced doping method of 1L-TMDs. The ability to modulate the carrier density in a monolayer crystal lattice in parallel with valley degree of freedom is a timely topic in the field 2D materials. At the same, the observed high degree of circular polarization in room temperature for a 1L-TMD on graphite revealed in this thesis opens up new opportunities to understand and explore valley physics in these materials.

Below is a summary of the most promising results obtained during this thesis.

In Chapter I a summary of the crystal and electronic properties of TMDs monolayers is presented. The basic fabrication methods of these ultrathin crystals have been also introduced. Furthermore the most important aspects of excitons, Spin Valley Polarization, optical selection rules, as well as the vibration properties of 2D-TMDs, have been presented.

In Chapter II we discuss different doping and carrier density modulation strategies in 1L-TMDs. Emphasis is given on the effect of doping on Raman, and valley polarization properties.

In Chapter III, the main experimental methods that employed for the photochemical doping as well as for investigating the optical and electronic properties of 1L-TMDs have been demonstrated.

Chapter IV is divided into three different parts that provide the most important results of this thesis. In the first subchapter, we showed that following the photochlorination process the chlorine dopants create a basal plane on the monolayer surface and attract electrons from the monolayer WS_2 lattice. Micro-Photoluminescence and micro-Differential reflectivity measurements show that, following the photochlorination treatment, the neutral exciton emission is enhanced. Also, a systematic blue shift of the sensitive-to-doping out-of-plane

Raman mode is presented. These findings combined with XPS analysis and theoretical simulations proved that chlorine doping give rise to a reduction of the electron density in a monolayer WS_2. An impressive part of this work is that we can not only control the doping level but also reverse the doping process upon laser cleaning of the monolayer surface. Following laser cleaning, the carrier density in the system returns to its initial levels. In the second subchapter, the emission and polarization dynamics of neutral and charged excitons have been investigated before and after photochlorination doping. It is shown that the circular polarization of 1L-WS_2/hBN and 1L-WS_2/SiO_2 is reduced after the photochlorination treatment. Theoretical simulations and TAS measurements indicate that the non-radiative recombination time (τ_{NR}) has the leading role behind the valley polarization effect. Indeed, the observed decrease in the polarization degree was attributed to the reduction of the active defect sites as a result of the chlorine doping. This in turn affects the non-radiative recombination time τ_{NR} and thus the degree of the emitted circular polarization. In the third subchapter, we show that using different substrates for 1L-WS_2 at resonant excitation conditions one can obtain high degree of circular polarization at room temperature. In particular, when 1L-WS_2 on top of Graphite is excited with on-resonance circularly polarized light, we measure a high (~25%) degree of valley polarization at room temperature. More important, the degree of valley polarization is further increased upon photochlorination treatment and reaches almost 40% at room temperature.

The ability to tune the carrier density and the degree of valley polarization in monolayer WS_2 via the photochlorination process opens up new opportunities to understand and explore the valley physics in these materials. The high degree of room temperature valley polarization observed in photochlorinated WS_2 on graphite is used as a substrate for 1L-WS_2 provides a new direction to enhance valley control via valley selective excitation and creates an intriguing platform for spin and valley physics and related devices.

The work of section 4.1 was published in 2D Materials, IOP Science (I. Demeridou, I. Paradisanos, Y. Liu, N. Pliatsikas, P. Patsalas, S. Germanis, N. T. Pelekanos, W A Goddard III, G. Kioseoglou & E. Stratakis. (2018). Spatially selective reversible charge carrier density tuning in WS_2 monolayers via photochlorination. 2D Materials, 6(1), 015003).

The work of section 4.2 was submitted in Applied Physics Letters (I. Demeridou, A. Papadopoulos, G. Kourmoulakis, L. Mouchliadis, E. Stratakis, and G. Kioseoglou, Tuning the valley polarization in WS_2 monolayers with photochemical doping).

The work of Chapter 4.3 is under preparation for submission.

References

[1] K.S. Novoselov, A.K. Geim, S. V Morozov, D. Jiang, Y. Zhang, S. V Dubonos, I. V Grigorieva, and A.A. Firsov, *Electric Field Effect in Atomically Thin Carbon Films* (2004).

[2] A. Geim and I. V Grigorieva, Nature **499**, 419 (2013).

[3] V. Nicolosi, M. Chhowalla, M.G. Kanatzidis, M.S. Strano, and J.N. Coleman, Science (80-.). **340**, 6139 (2013).

[4] M. Chhowalla, H. Suk Shin, G. Eda, L.J. Li, K. Ping Loh, and H. Zhang, Nat. Chem. **5**, 263 (2013).

[5] B. Radisavljevic, A. Radenovic, J. Brivio, V. Giacometti, and A. Kis, Nat. Nanotechnol. **6**, 147 (2011).

[6] B. Radisavljevic, M.B. Whitwick, and A. Kis, ACS Nano **5**, 9934 (2011).

[7] J.S. Ross, P. Klement, A.M. Jones, N.J. Ghimire, J. Yan, D.G. Mandrus, T. Taniguchi, K. Watanabe, K. Kitamura, W. Yao, D.H. Cobden, and X. Xu, Nat. Nanotechnol. **9**, 268 (2014).

[8] A. Pospischil, M.M. Furchi, and T. Mueller, *Solar Energy Conversion and Light Emission in an Atomic Monolayer P-n Diode* (2014).

[9] B.W.H. Baugher, H.O.H. Churchill, Y. Yang, and P. Jarillo-Herrero, *Optoelectronic Devices Based on Electrically Tunable P-n Diodes in a Monolayer Dichalcogenide* (2014).

[10] F. Withers, O. Del Pozo-Zamudio, A. Mishchenko, A.P. Rooney, A. Gholinia, K. Watanabe, and K.S. Novoselov, Nat. Mater. **14**, 301 (2015).

[11] D. Xiao, G. Liu, W. Feng, X. Xu, and W. Yao, Phys. Rev. Lett. **108**, 196802 (2012).

[12] J. Schaibley, H. Yu, G. Clark, P. Rivera, J. Ross, K. Seyler, and X. Xu, Nat. Rev. Mater. **1**, 1 (2016).

[13] J.A. Wilson and A.D. Yoffe, Adv. Phys. **18**, 193 (1969).

[14] G. Bin Liu, D. Xiao, Y. Yao, X. Xu, and W. Yao, Chem. Soc. Rev. **44**, 2643 (2015).

[15] P. Avouris, T. Heinz, and T. Low, Cambridge Cambridge Univ. Press 257 (2017).

[16] R. Roldán, J.A. Silva-Guillén, M.P. López-Sancho, F. Guinea, E. Cappelluti, and P. Ordejón, Ann. Phys. **526**, 347 (2014).

[17] K.F. Mak, C. Lee, J. Hone, J. Shan, and T.F. Heinz, Phys. Rev. Lett. **105**, 136805 (2010).

[18] A. Splendiani, L. Sun, Y. Zhang, T. Li, J. Kim, C.Y. Chim, G. Galli, and F. Wang, Nano Lett. **10**, 1271 (2010).

[19] J.O. Varghese, P. Agbo, A.M. Sutherland, V.W. Brar, G.R. Rossman, H.B. Gray, and J.R. Heath, Adv. Mater. **27**, 2734 (2015).

[20] H. Zeng, G. Liu, J. Dai, Y. Yan, B. Zhu, R. He, and X. Cui, Sci. Rep. **3**, 1608 (2013).

[21] K.S. Novoselov, D. Jiang, F. Schedin, T.J. Booth, V. V Khotkevich, S. V Morozov, and A.K. Geim, Proc. Natl. Acad. Sci. **102**, 10451 (2005).

[22] C. Lee, H. Yan, L.E. Brus, T.F. Heinz, J. Hone, and S. Ryu, ACS Nano **4**, 2695 (2010).

[23] S. Bertolazzi, J. Brivio, and A. Kis, ACS Nano **5**, 9703 (2011).

[24] F. Pizzocchero, L. Gammelgaard, B.S. Jessen, J.M. Caridad, L. Wang, J. Hone, and T.J. Booth, Nat.

Commun. **7**, 1 (2016).

[25] J.N. Coleman, M. Lotya, A. O'Neill, S.D. Bergin, P.J. King, U. Khan, and I. V. Shvets, Science (80-.). **331**, 568 (2011).

[26] C. Backes, R. Smith, N. McEvoy, N.C. Berner, D. McCloskey, H.C. Nerl, and N. Scheuschner, Nat. Commun. **5**, 1 (2014).

[27] K. Lee, H.Y. Kim, M. Lotya, J.N. Coleman, G.T. Kim, and G.S. Duesberg, Adv. Mater. **23**, 4178 (2011).

[28] J.R. Creighton and P. Ho, *Introduction to Chemical Vapor Deposition (CVD)* (2001).

[29] Y. Shi, H. Li, and L.-J. Li, Chem. Soc. Rev. **44**, 2744 (2015).

[30] P. Cudazzo, I. V Tokatly, and A. Rubio, Phys. Rev. B **84**, 85406 (2011).

[31] A. Ramasubramaniam, Phys. Rev. B **86**, 115409 (2012).

[32] A. Chernikov, T.C. Berkelbach, H.M. Hill, A. Rigosi, Y. Li, O.B. Aslan, D.R. Reichman, M.S. Hybertsen, and T.F. Heinz, Phys. Rev. Lett. **113**, 076802 (2014).

[33] D.Y. Qiu, F.H. Da Jornada, and S.G. Louie, Phys. Rev. Lett. **111**, 216805 (2013).

[34] G. Berghäuser and E. Malic, Phys. Rev. B **89**, 125309 (2014).

[35] H.P. Komsa and A. V Krasheninnikov, Phys. Rev. B **86**, 241201 (2012).

[36] T.C. Berkelbach, M.S. Hybertsen, and D.R. Reichman, Phys. Rev. B **88**, 45318 (2013).

[37] K. He, N. Kumar, L. Zhao, Z. Wang, K.F. Mak, H. Zhao, and J. Shan, Phys. Rev. Lett. **113**, 026803 (2014).

[38] N. Scheuschner, O. Ochedowski, A.M. Kaulitz, R. Gillen, M. Schleberger, and J. Maultzsch, Phys. Rev. B **89**, 125406 (2014).

[39] A. Kolobov V. and J. Tominaga., *Two-Dimensional Transition-Metal Dichalcogenides* (2016).

[40] Z. Ye, T. Cao, K. O'brien, H. Zhu, X. Yin, Y. Wang, and X. Zhang, Nature **513**, 214 (2014).

[41] C.F. Klingshirn, Springer, Berlin (1995).

[42] H. Shi, H. Pan, Y.-W. Zhang, and B.I. Yakobson, Phys. Rev. B **87**, 155304 (2013).

[43] T. Cheiwchanchamnangij and W.R.L. Lambrecht, Phys. Rev. B **85**, 205302 (2012).

[44] D. Kozawa, R. Kumar, A. Carvalho, K. Kumar Amara, W. Zhao, S. Wang, M. Toh, R.M. Ribeiro, A.H. Castro Neto, K. Matsuda, and G. Eda, Nat. Commun. **5**, 1 (2014).

[45] H. Yu, X. Cui, X. Xu, and W. Yao, Natl. Sci. Rev. **2**, 57 (2015).

[46] K. Kheng, R.T. Cox, M.Y. D'Aubigné, F. Bassani, K. Saminadayar, and S. Tatarenko, Phys. Rev. Lett. **71**, 1752 (1993).

[47] K. Mak, K. He, C. Lee, G. Lee, J. Hone, T.F. Heinz, and J. Shan, Nat. Mater. **12**, 207 (2013).

[48] A.A. Mitioglu, P. Plochocka, J.N. Jadczak, W. Escoffier, G.L.J.A. Rikken, L. Kulyuk, and D.K. Maude, Phys. Rev. B **88**, 245403 (2013).

[49] J. Yang, T. Lü, Y.W. Myint, J. Pei, D. Macdonald, J.C. Zheng, and Y. Lu, ACS Nano **9**, 6603 (2015).

[50] J. Ross, S. Wu, H. Yu, N. Ghimire, A.M. Jones, G. Aivazian, and X. Xu, Nat. Commun. **4**, 1 (2013).

[51] M.D. Tran, J.H. Kim, and Y.H. Lee, Curr. Appl. Phys. 1159 (2016).

[52] B. Zhu, X. Chen, and X. Cui, Sci. Rep. **5**, 9218 (2015).

[53] A.M. Jones, H. Yu, N.J. Ghimire, S. Wu, G. Aivazian, J.S. Ross, B. Zhao, J. Yan, D.G. Mandrus, D. Xiao, W. Yao, and X. Xu, Nat. Nanotechnol. **8**, 634 (2013).

[54] J. Shang, X. Shen, C. Cong, N. Peimyoo, B. Cao, M. Eginligil, and T. Yu, ACS Nano **9**, 647 (2015).

[55] I. Paradisanos, S. Germanis, N.T. Pelekanos, C. Fotakis, E. Kymakis, G. Kioseoglou, and E. Stratakis, Appl. Phys. Lett. **110**, 193102 (2017).

[56] W. Yao, D. Xiao, and Q. Niu, Phys. Rev. B **77**, 235406 (2008).

[57] X. Xu, W. Yao, D. Xiao, and T. Heinz, Nat. Phys. **10**, 343 (2014).

[58] K.F. Mak, K. He, J. Shan, and T.F. Heinz, Nat. Nanotechnol. **7**, 494 (2012).

[59] T. Cao, G. Wang, W. Han, H. Ye, C. Zhu, J. Shi, Q. Niu, P. Tan, E. Liu, and J. Feng, Nat. Commun. **3**, 1 (2012).

[60] H. Zeng, J. Dai, W. Yao, D. Xiao, and X. Cui, Nat. Nanotechnol. **7**, 490 (2012).

[61] G. Kioseoglou, A.T. Hanbicki, M. Currie, A.L. Friedman, D. Gunlycke, and B. Jonker, Appl. Phys. Lett. **101**, 221907 (2012).

[62] W. Zhao, Z. Ghorannevis, A. Kiran Kumar, J. Ren Pang, M. Toh, X. Zhang, C. Kloc, P. Heng Tan, and G. Eda, *Lattice Dynamics in Mono-and Few-Layer Sheets of WS2 and WSe2* (2013).

[63] X. Zhang, X.F. Qiao, W. Shi, J. Bin Wu, D.S. Jiang, and P.H. Tan, Chem. Soc. Rev. **44**, 2757 (2015).

[64] T. Korn, S. Heydrich, M. Hirmer, J. Schmutzler, and C. Schüller, Appl. Phys. Lett. **99**, 102109 (2011).

[65] A. Molina-Sánchez and L. Wirtz, Phys. Rev. B **84**, 155413 (2011).

[66] A. Berkdemir, H. Gutiérrez, A.R. Botello-Méndez, N. Perea-López, A.L. Elías, C.I. Chia, and H. Terrones, Sci. Rep. **3**, 1 (2013).

[67] G. Seifert, H. Terrones, M. Terrones, G. Jungnickel, and T. Frauenheim, Phys. Rev. Lett. **85**, 146 (2000).

[68] D.R. Cooper, B. D'Anjou, N. Ghattamaneni, B. Harack, M. Hilke, A. Horth, N. Majlis, M. Massicotte, L. Vandsburger, E. Whiteway, and V. Yu, ISRN Condens. Matter Phys. **2012**, 1 (2012).

[69] A.H. Castro Neto, F. Guinea, N.M.R. Peres, K.S. Novoselov, and A.K. Geim, Rev. Mod. Phys. **81**, 109 (2009).

[70] A.C. Ferrari, J.C. Meyer, V. Scardaci, C. Casiraghi, M. Lazzeri, F. Mauri, S. Piscanec, D. Jiang, K.S. Novoselov, S. Roth, and A.K. Geim, Phys. Rev. Lett. **97**, 187401 (2006).

[71] A.C. Ferrari, Solid State Commun. **143**, 47 (2007).

[72] P. Luo, F. Zhuge, Q. Zhang, Y. Chen, L. Lv, Y. Huang, and T. Zhai, Nanoscale Horizons **4**, 26 (2019).

[73] C. Ataca and S. Ciraci, J. Phys. Chem. C **115**, 13303 (2011).

[74] J. Yu, C.-H. Lee, D. Bouilly, M. Han, P. Kim, M.L. Steigerwald, X. Roy, and C. Nuckolls, Nano Lett. **16**, 3385 (2016).

[75] M. Chen, H. Nam, S. Wi, L. Ji, X. Ren, L. Bian, S. Lu, and X. Liang, Appl. Phys. Lett. **103**, 142110 (2013).

[76] D. Kiriya, M. Tosun, P. Zhao, J.S. Kang, and A. Javey, J. Am. Chem. Soc. **136**, 7853 (2014).

[77] Y.M. Chang, S.H. Yang, C.Y. Lin, C.H. Chen, C.H. Lien, W. Bin Jian, K. Ueno, Y.W. Suen, K. Tsukagoshi, and Y.F. Lin, Adv. Mater. **30**, 1706995 (2018).

[78] H. Fang, S. Chuang, T.C. Chang, K. Takei, T. Takahashi, and A. Javey, Nano Lett. **12**, 3788 (2012).

[79] S. Bertolazzi, M. Gobbi, Y. Zhao, C. Backes, and P. Samorì, *Molecular Chemistry Approaches for Tuning the Properties of Two-Dimensional Transition Metal Dichalcogenides* (2018).

[80] Y. Jing, Z. Zhou, X. Tan, and P. Shen, J. Mater. Chem. **2**, 16892 (2014).

[81] H. V. Han, A.Y. Lu, L.S. Lu, J.K. Huang, H. Li, C.L. Hsu, and H.C. Kuo, ACS Nano **10**, 1454 (2016).

[82] S. Mouri, Y. Miyauchi, and K. Matsuda, Nano Lett. **13**, 5944 (2013).

[83] Y. Kim, Y.I. Jhon, J. Park, C. Kim, S. Lee, and Y.M. Jhon, Sci. Rep. **6**, 21405 (2016).

[84] R. Rao, V. Carozo, Y. Wang, A. Islam, N. Perea-Lopez, K. Fujisawa, and B. Maruyama, 2D Mater. **6**, 045031 (2019).

[85] Y. Li, X. Li, H. Chen, J. Shi, Q. Shang, S. Zhang, X. Qiu, Z. Liu, Q. Zhang, H. Xu, W. Liu, X. Liu, and Y. Liu, ACS Appl. Mater. Interfaces **9**, 27402 (2017).

[86] S. Tongay, J. Zhou, C. Ataca, J. Liu, J.S. Kang, T.S. Matthews, L. You, J. Li, J.C. Grossman, and J. Wu, Nano Lett. **13**, 2831 (2013).

[87] L. Yang, K. Majumdar, H. Liu, Y. Du, H. Wu, M. Hatzistergos, P.Y. Hung, R. Tieckelmann, W. Tsai, C. Hobbs, and P.D. Ye, Nano Lett. **14**, 6275 (2014).

[88] D.M. Sim, M. Kim, S. Yim, M.J. Choi, J. Choi, S. Yoo, and Y.S. Jung, ACS Nano **9**, 12115 (2015).

[89] J. Liang, X. Li, B. Pan, L. Zhang, Y. Dong, C. Zou, and S. Huang, 2D Mater. **6**, 025003 (2019).

[90] N. Peimyoo, W. Yang, J. Shang, X. Shen, Y. Wang, and T. Yu, ACS Nano **8**, 11320 (2014).

[91] J.D. Lin, C. Han, F. Wang, R. Wang, D. Xiang, S. Qin, X.A. Zhang, L. Wang, H. Zhang, A.T.S. Wee, and W. Chen, ACS Nano **8**, 5323 (2014).

[92] C. Anichini, W. Czepa, D. Pakulski, A. Aliprandi, A. Ciesielski, and P. Samorì, Chem. Soc. Rev. **47**, 4860 (2018).

[93] S. Najmaei, X. Zou, D. Er, J. Li, Z. Jin, W. Gao, Q. Zhang, S. Park, L. Ge, S. Lei, J. Kono, V.B. Shenoy, B.I. Yakobson, A. George, P.M. Ajayan, and J. Lou, Nano Lett. **14**, 1354 (2014).

[94] Y. Li, C.Y. Xu, P. Hu, and L. Zhen, ACS Nano **7**, 7795 (2013).

[95] H. Nan, Z. Wang, W. Wang, Z. Liang, Y. Lu, Q. Chen, D. He, P. Tan, F. Miao, X. Wang, J. Wang, and Z. Ni, ACS Nano **8**, 5738 (2014).

[96] M. Tosun, L. Chan, M. Amani, T. Roy, G.H. Ahn, P. Taheri, C. Carraro, J.W. Ager, R. Maboudian, and A. Javey, ACS Nano **10**, 6853 (2016).

[97] J. Suh, T.-E. Park, D.-Y. Lin, D. Fu, J. Park, ‖ Hee, J. Jung, Y. Chen, C. Ko, C. Jang, Y. Sun, R. Sinclair, J. Chang, S. Tongay, and J. Wu, Nano Lett. **14**, 6976 (2014).

[98] Q. Yue, S. Chang, S. Qin, J. Li, and R. Wu, Phys. Lett. A **377**, 1362 (2013).

[99] K. Dolui, I. Rungger, C. Das Pemmaraju, and S. Sanvito, Phys. Rev. B **88**, 75420 (2013).

[100] Y. Yue, C. Jiang, Y. Han, M. Wang, J. Ren, and H. Wu, J. Magn. Magn. Mater. **496**, 165929 (2020).

[101] H. Yao, L. Liu, Z. Wang, H. Li, L. Chen, M. Pam, and Y. Shi, Nanoscale **10**, 6105 (2018).

[102] A. Azcatl, X. Qin, A. Prakash, C. Zhang, L. Cheng, Q. Wang, N. Lu, M.J. Kim, J. Kim, K. Cho, R. Addou, C.L. Hinkle, J. Appenzeller, and R.M. Wallace, Nano Lett. **16**, 5437 (2016).

[103] T.S. Sreeprasad, P. Nguyen, N. Kim, and V. Berry, Nano Lett. **13**, 4434 (2013).

[104] K.Y. Ma, S.I. Yoon, A.R. Jang, H.Y. Jeong, Y.J. Kim, P.K. Nayak, and H.S. Shin, Artic. J. Mater. Chem. C **5**, 11294 (2017).

[105] D. Pierucci, H. Henck, Z. Ben Aziza, C.H. Naylor, A. Balan, J.E. Rault, M.G. Silly, Y.J. Dappe, F. Bertran, P. Le Fèvre, F. Sirotti, A.T.C. Johnson, and A. Ouerghi, ACS Nano **11**, 1755 (2017).

[106] M. Chen, H. Nam, S. Wi, L. Ji, X. Ren, L. Bian, S. Lu, and X. Liang, Appl. Phys. Lett. **103**, 142110 (2013).

[107] A. Nipane, D. Karmakar, N. Kaushik, S. Karande, and S. Lodha, ACS Nano **10**, 2128 (2016).

[108] H.P. Komsa and A. V Krasheninnikov, J. Phys. Chem. Lett **3**, 3652 (2012).

[109] N. Onofrio, D. Guzman, and A. Strachan, J. Appl. Phys. **122**, 185102 (2017).

[110] J. Kang, S. Tongay, J. Li, and J. Wu, J. Appl. Phys. **113**, 143703 (2013).

[111] V. Klee, E. Preciado, D. Barroso, A.E. Nguyen, C. Lee, K.J. Erickson, M. Triplett, B. Davis, I.H. Lu, S. Bobek, J. McKinley, J.P. Martinez, J. Mann, A.A. Talin, L. Bartels, and F. Léonard, Nano Lett. **15**, 2612 (2015).

[112] W. Kang, I. Lee, S. Yun, Y. Song, K. Kim, D. Kim, and Y. Lee, Nanoscale **10**, 11397 (2018).

[113] Y.C. Lin, D.O. Dumcenco, H.P. Komsa, Y. Niimi, A. V. Krasheninnikov, Y.S. Huang, and K. Suenaga, Adv. Mater. **26**, 2857 (2014).

[114] J. Gao, Y.D. Kim, L. Liang, J.C. Idrobo, P. Chow, J. Tan, B. Li, L. Li, B.G. Sumpter, T.M. Lu, V. Meunier, J. Hone, and N. Koratkar, Adv. Mater. **28**, 9735 (2016).

[115] X. Li, M.W. Lin, L. Basile, S.M. Hus, A.A. Puretzky, J. Lee, Y.C. Kuo, L.Y. Chang, K. Wang, J.C. Idrobo, A.P. Li, C.H. Chen, C.M. Rouleau, D.B. Geohegan, and K. Xiao, Adv. Mater. **28**, 8240 (2016).

[116] D.J. Lewis, A.A. Tedstone, X.L. Zhong, E.A. Lewis, A. Rooney, N. Savjani, J.R. Brent, S.J. Haigh, M.G. Burke, C.A. Muryn, J.M. Raftery, C. Warrens, K. West, S. Gaemers, and P. O'Brien, Chem. Mater. **27**, 1367 (2015).

[117] N. Al-Dulaimi, D. Lewis, X. Zhong, & Malik, M. A., and P. O'Brien, J. Mater. Chem. **4**, 2312 (2016).

[118] M. Li, J. Yao, X. Wu, S. Zhang, B. Xing, X. Niu, X. Yan, Y. Yu, Y. Liu, and Y. Wang, ACS Appl. Mater. Interfaces **12**, 6276 (2020).

[119] J. Suh, T. Tan, W. Zhao, J. Park, D. Lin, T. Park, and Z. Wong, Nat. Commun. **9**, 1 (2018).

[120] S. Lacey, W. Bao, J. Wan, S.D. Lacey, J. Dai, M.S. Fuhrer, and L. Hu, Chem. Soc. Rev. **45**, 6742 (2016).

[121] M.R. Lukatskaya, O. Mashtalir, C.E. Ren, Y. Dall'agnese, P. Rozier, P.-L. Taberna, M. Naguib, P. Simon, M.W. Barsoum, and Y. Gogotsi, Science (80-.). **341**, 1502 (2013).

[122] D. Kang, S. Dugasani, H.Y. Park, J. Shim, B. Gnapareddy, J. Jeon, and J.H. Park, Sci. Rep. **6**, 20333 (2016).

[123] P.M. Coelho, H.-P. Komsa, H.C. Diaz, Y. Ma, A. V Krasheninnikov, and M. Batzill, ACS Nano **12**, 3975 (2018).

[124] Y. Gong, H. Yuan, C.-L. Wu, P. Tang, S.-Z. Yang, A. Yang, G. Li, B. Liu, J. Van De Groep, M.L.

Brongersma, M.F. Chisholm, S.-C. Zhang, W. Zhou, and Y. Cui, Nat. Nanotechnol. **13**, 294 (2018).

[125] K.J. Koski, C.D. Wessells, B.W. Reed, J.J. Cha, D. Kong, and Y. Cui, J. Am. Chem. Soc. **134**, 13773 (2012).

[126] K. Zhang, S. Feng, J. Wang, A. Azcatl, N. Lu, R. Addou, N. Wang, C. Zhou, J. Lerach, V. Bojan, M.J. Kim, L.Q. Chen, R.M. Wallace, M. Terrones, J. Zhu, and J.A. Robinson, Nano Lett. **15**, 6586 (2015).

[127] J. Zheng, H. Zhang, S. Dong, Y. Liu, C.T. Nai, H.S. Shin, and K.P. Loh, Nat. Commun. **5**, 1 (2014).

[128] M. Chhowalla, D. Jena, and H. Zhang, Nat. Rev. Mater. **1**, 1 (2016).

[129] I. Lee, S. Rathi, L. Li, D. Lim, M. Khan, E. Kannan, and G. Kim, Nanotechnology **26**, 455203 (2015).

[130] C.J. Lockhart De La Rosa, R. Phillipson, J. Teyssandier, J. Adisoejoso, Y. Balaji, C. Huyghebaert, I. Radu, M. Heyns, S. De Feyter, and S. De Gendt, Appl. Phys. Lett. **109**, 253112 (2016).

[131] S. Wi, H. Kim, M. Chen, H. Nam, L.J. Guo, E. Meyhofer, and X. Liang, ACS Nano **8**, 5270 (2014).

[132] G. Kukucska and J. Koltai, Phys. Status Solidi **254**, 1700184 (2017).

[133] B. Chakraborty, A. Bera, D.V.S. Muthu, S. Bhowmick, U. V Waghmare, and A.K. Sood, Phys. Rev. B **85**, 161403 (2012).

[134] M. Yamamoto, T.L. Einstein, M.S. Fuhrer, and W.G. Cullen, J. Phys. Chem. C **117**, 25643 (2013).

[135] S. Zhang, H.M. Hill, K. Moudgil, C.A. Richter, A.R. Hight Walker, S. Barlow, S.R. Marder, C.A. Hacker, and S.J. Pookpanratana, Adv. Mater. **30**, 1802991 (2018).

[136] Y. Wang, C. Cong, C. Qiu, and T. Yu, Small **9**, 2857 (2013).

[137] S. Horzum, H. Sahin, S. Cahangirov, P. Cudazzo, § A Rubio, | T Serin, and F.M. Peeters, Phys. Rev. B **87**, 125415 (2013).

[138] W.M. Parkin, A. Balan, L. Liang, P.M. Das, M. Lamparski, C.H. Naylor, J.A. Rodríguez-Manzo, A.T.C. Johnson, V. Meunier, and M. Drndić, ACS Nano **10**, 4134 (2016).

[139] N. Mao, Y. Chen, D. Liu, J. Zhang, and L. Xie, Small **9**, 1312 (2013).

[140] G.L. Frey, R. Tenne, M.J. Matthews, M.S. Dresselhaus, and G. Dresselhaus, Phys. Rev. B **60**, 2883 (1999).

[141] D.H. Kang, M.S. Kim, J. Shim, J. Jeon, H.Y. Park, W.S. Jung, H.Y. Yu, C.H. Pang, S. Lee, and J.H. Park, Adv. Funct. Mater. **25**, 4219 (2015).

[142] J. Siviniant, D. Scalbert, A. V. Kavokin, D. Coquillat, and J.P. Lascaray, Phys. Rev. B **59**, 1602 (1999).

[143] K.K. Ki, J.B. Jung, K.P. Hyeon, M.K. Soo, H.Z. Geng, A.P. Kyung, H.J. Shin, S.M. Yoon, A. Benayad, J.Y. Choi, and H.L. Young, J. Am. Chem. Soc. **130**, 12757 (2008).

[144] K.K. Kim, A. Reina, Y. Shi, H. Park, L.J. Li, Y.H. Lee, and J. Kong, Nanotechnology **21**, 285205 (2010).

[145] B. Liu, L. Chen, G. Liu, A.N. Abbas, M. Fathi, and C. Zhou, ACS Nano **8**, 5304 (2014).

[146] F.K. Perkins, A.L. Friedman, E. Cobas, P.M. Campbell, G.G. Jernigan, and B.T. Jonker, Nano Lett. **13**, 668 (2013).

[147] Y. Du, H. Liu, A.T. Neal, M. Si, and P.D. Ye, IEEE Electron Device Lett. **34**, 1328 (2013).

[148] H. Schmidt, F. Giustiniano, and G. Eda, Chem. Soc. Rev. **44**, 7715 (2015).

[149] H. Li, Z. Yin, Q. He, H. Li, X. Huang, G. Lu, D.W.H. Fam, A.I.Y. Tok, Q. Zhang, and H. Zhang, Small **8**,

63 (2012).

[150] G. Kioseoglou, A. Hanbicki, M. Currie, A.L. Friedman, and B.T. Jonker, Sci. Rep. **6**, 1 (2016).

[151] A. Hanbicki, G. Kioseoglou, M. Currie, C.S. Hellberg, K.M. Mccreary, A.L. Friedman, and B.T. Jonker, Sci. Rep. **6**, 1 (2016).

[152] Y. Song and H. Dery, Phys. Rev. Lett. **111**, 026601 (2013).

[153] M.M. Glazov, E.L. Ivchenko, G. Wang, T. Amand, X. Marie, B. Urbaszek, and B.L. Liu, Phys. Status Solidi **252**, 2349 (2015).

[154] G. Sallen, L. Bouet, X. Marie, G. Wang, C.R. Zhu, W.P. Han, Y. Lu, P.H. Tan, T. Amand, B.L. Liu, and B. Urbaszek, Phys. Rev. B **86**, 081301 (2012).

[155] Y. Li, J. Ludwig, T. Low, A. Chernikov, X. Cui, G. Arefe, Y.D. Kim, A.M. Van Der Zande, A. Rigosi, H.M. Hill, S.H. Kim, J. Hone, Z. Li, D. Smirnov, and T.F. Heinz, Phys. Rev. Lett. **113**, 266804 (2014).

[156] A. Srivastava, M. Sidler, A. Allain, D. Lembke, A. Kis, and A. Imamoğlu, Nat. Phys. **11**, 141 (2015).

[157] A.T. Hanbicki, K.M. McCreary, G. Kioseoglou, M. Currie, C.S. Hellberg, A.L. Friedman, and B.T. Jonker, AIP Adv. **6**, 055804 (2016).

[158] L. Du, Q. Zhang, B. Gong, M. Liao, J. Zhu, H. Yu, R. He, K. Liu, R. Yang, D. Shi, L. Gu, F. Yan, G. Zhang, and Q. Zhang, Phys. Rev. B **97**, 115445 (2018).

[159] F. Cadiz, E. Courtade, C. Robert, G. Wang, Y. Shen, H. Cai, T. Taniguchi, K. Watanabe, H. Carrere, D. Lagarde, M. Manca, T. Amand, P. Renucci, S. Tongay, X. Marie, and B. Urbaszek, Phys. Rev. X **7**, 021026 (2017).

[160] A. Arora, R. Schmidt, R. Schneider, M.R. Molas, I. Breslavetz, M. Potemski, and R. Bratschitsch, Nano Lett. **16**, 3624 (2016).

[161] S. Feng, C. Cong, N. Peimyoo, Y. Chen, J. Shang, C. Zou, B. Cao, L. Wu, J. Zhang, M. Eginligil, X. Wang, Q. Xiong, A. Ananthanarayanan, P. Chen, B. Zhang, and T. Yu, Nano Res. **11**, 1744 (2018).

[162] G. Plechinger, P. Nagler, J. Kraus, N. Paradiso, C. Strunk, C. Schüller, and T. Korn, Phys. Status Solidi - Rapid Res. Lett. **9**, 457 (2015).

[163] P. Dey, L. Yang, C. Robert, G. Wang, B. Urbaszek, X. Marie, and S.A. Crooker, Phys. Rev. Lett. **119**, 137401 (2017).

[164] S. Feng, C. Cong, S. Konabe, J. Zhang, J. Shang, Y. Chen, and B. Zhang, Small **15**, 1805503 (2019).

[165] J.J. Carmiggelt, M. Borst, and T. van der Sar, Sci. Rep. **10**, 1 (2020).

[166] S. Konabe, Appl. Phys. Lett. **109**, 073104 (2016).

[167] Y. Miyauchi, S. Konabe, F. Wang, W. Zhang, A. Hwang, Y. Hasegawa, L. Zhou, S. Mouri, M. Toh, G. Eda, and K. Matsuda, Nat. Commun. **9**, 1 (2018).

[168] D. Lagarde, L. Bouet, X. Marie, C.R. Zhu, B.L. Liu, T. Amand, P.H. Tan, and B. Urbaszek, Phys. Rev. Lett. **112**, 047401 (2014).

[169] A. Neumann, J. Lindlau, L. Colombier, M. Nutz, S. Najmaei, J. Lou, A.D. Mohite, H. Yamaguchi, and A. Högele, Nat. Nanotechnol. **12**, 329 (2017).

[170] I.M. Paradisanos, Phys. Dep. Heraklion, Crete (2018).

[171] N. Saigal, I. Wielert, D. Čapeta, N. Vujičić, B. V. Senkovskiy, M. Hell, M. Kralj, and A. Grüneis, Appl. Phys. Lett. **112**, 121902 (2018).

[172] C.A. Howard, M.P.M. Dean, and F. Withers, Phys. Rev. B **84**, 241404 (2011).

[173] K. Cho, W. Park, J. Park, H. Jeong, J. Jang, T.Y. Kim, W.K. Hong, S. Hong, and T. Lee, ACS Nano **7**, 7751 (2013).

[174] E. Kim, C. Ko, K. Kim, Y. Chen, J. Suh, S.G. Ryu, K. Wu, X. Meng, A. Suslu, S. Tongay, J. Wu, and C.P. Grigoropoulos, Adv. Mater. **28**, 341 (2016).

[175] G. Eda, H. Yamaguchi, D. Voiry, T. Fujita, M. Chen, and M. Chhowalla, Nano Lett. **11**, 5111 (2011).

[176] I. Paradisanos, N. Pliatsikas, P. Patsalas, C. Fotakis, E. Kymakis, G. Kioseoglou, and E. Stratakis, Nanoscale **8**, 16197 (2016).

[177] W. Zhao, Z. Ghorannevis, L. Chu, M. Toh, C. Kloc, P.H. Tan, and G. Eda, ACS Nano **7**, 791 (2013).

[178] A.S. Bracker, E.A. Stinaff, D. Gammon, M.E. Ware, J.G. Tischler, D. Park, D. Gershoni, A. V Filinov, M. Bonitz, F. Peeters, and C. Riva, Phys. Rev. B **72**, 035332 (2005).

[179] V. Huard, R.T. Cox, K. Saminadayar, A. Arnoult, and S. Tatarenko, Phys. Rev. Lett. **84**, 187 (2000).

[180] K. McCreary, A. Hanbicki, G. Jernigan, J.C. Culbertson, and B.T. Jonker, Sci. Rep. **6**, 19159 (2016).

[181] B. Lindberg, K. Hamrin, G. Johansson, U. Gelius, A. Fahlman, C. Nordling, and K. Siegbahn, Phys. Scr. **1**, 286 (1970).

[182] M. Neustetter, F.F. Da Silva, and S. Denifl, Rapid Commun. Mass Spectrom. **30**, 1139 (2016).

[183] G. Kresse and J. Hafner, Phys. Rev. B **47**, 558 (1993).

[184] G. Kresse and J. Furthmüller, Phys. Rev. B **54**, 11169 (1996).

[185] P.E. Blöchl, Phys. Rev. B **50**, 17953 (1994).

[186] J.P. Perdew, K. Burke, and M. Ernzerhof, Phys. Rev. Lett. **77**, 3865 (1996).

[187] Q.H. Wang, K. Kalantar-Zadeh, A. Kis, J.N. Coleman, and M.S. Strano, Nat. Nanotechnol. **7**, 699 (2012).

[188] M. Xu, T. Liang, M. Shi, and H. Chen, Chem. Rev. **113**, 3766 (2013).

[189] G. Kioseoglou, M. Korkusinski, T. Scrace, A.T. Hanbicki, M. Currie, B.T. Jonker, A. Petrou, and P. Hawrylak, Phys. Status Solidi - Rapid Res. Lett. **10**, 111 (2016).

[190] Z.Y. Zhu, Y.C. Cheng, and U. Schwingenschl, Phys. Rev. B **84**, 153402 (2011).

[191] I. Demeridou, I. Paradisanos, Y. Liu, N. Pliatsikas, P. Patsalas, S. Germanis, N.T. Pelekanos, W.A. Goddard III, G. Kioseoglou, and E. Stratakis, 2D Mater. **6**, 015003 (2018).

[192] Q. Cai, A. Falin, K. Watanabe, D. Scullion, A. Falin, T. Taniguchi, Y. Chen, E.J.G. Santos, and L.H. Li, Nanoscale **9**, 3059 (2017).

[193] Z. Lin, B. Carvalho, E. Kahn, R. Lv, R. Rao, H. Terrones, and M. Terrones, 2D Mater. **3**, 022002 (2016).

[194] T. Yan, X. Qiao, P. Tan, and X. Zhang, Sci. Rep. **5**, 15625 (2015).

[195] G. Wang, L. Bouet, D. Lagarde, M. Vidal, A. Balocchi, T. Amand, X. Marie, and B. Urbaszek, Phys. Rev. B **90**, 075413 (2014).

[196] A. Molina-Sánchez, D. Sangalli, L. Wirtz, and A. Marini, Nano Lett. **17**, 4549 (2017).

[197] C. Robert, D. Lagarde, F. Cadiz, G. Wang, B. Lassagne, T. Amand, A. Balocchi, P. Renucci, S. Tongay,

B. Urbaszek, and X. Marie, Phys. Rev. B **93**, 205423 (2016).

[198] G. Wang, A. Chernikov, M.M. Glazov, T.F. Heinz, X. Marie, T. Amand, and B. Urbaszek, Rev. Mod. Phys. **90**, 021001 (2018).

[199] P.K. Nayak, F.-C. Lin, C.-H. Yeh, J.-S. Huang, and P.-W. Chiu, *Robust Room Temperature Valley Polarization in Monolayer and Bilayer WS2* (2016).

[200] K. McCreary, M. Currie, A. Hanbicki, H. Chuang, and B. Jonker, ACS Nano **11**, 7988 (2017).

[201] Y.K. Luo, J. Xu, T. Zhu, G. Wu, E.J. McCormick, W. Zhan, M.R. Neupane, and R.K. Kawakami, Nano Lett. **17**, 3877 (2017).

[202] A. Avsar, D. Unuchek, J. Liu, O.L. Sanchez, K. Watanabe, T. Taniguchi, B. Özyilmaz, and A. Kis, ACS Nano **11**, 11678 (2017).

[203] W. Han, R.K. Kawakami, M. Gmitra, and J. Fabian, Nat. Nanotechnol. **9**, 794 (2014).

[204] T.S. Ghiasi, J. Ingla-Aynés, A.A. Kaverzin, and B.J. Van Wees, Nano Lett. **17**, 7528 (2017).

[205] L.A. Benítez, J.F. Sierra, W.S. Torres, A. Arrighi, F. Bonell, M. V. Costache, and S.O. Valenzuela, Nat. Phys. 303 (2018).

[206] I. Paradisanos, K.M. McCreary, D. Adinehloo, L. Mouchliadis, J.T. Robinson, H.-J. Chuang, A.T. Hanbicki, V. Perebeinos, B.T. Jonker, E. Stratakis, and G. Kioseoglou, Appl. Phys. Lett. **116**, 203102 (2020).

[207] E. Lorchat, S. Azzini, T. Chervy, T. Taniguchi, K. Watanabe, T.W. Ebbesen, C. Genet, and S. Berciaud, ACS Photonics **5**, 5047 (2018).

[208] Y. Kobayashi, S. Sasaki, S. Mori, H. Hibino, Z. Liu, K. Watanabe, T. Taniguchi, K. Suenaga, Y. Maniwa, and Y. Miyata, ACS Nano **9**, 4056 (2015).